DETECTING SPATIAL AND TEMPORAL DISTRIBUTIONS OF LIPIDS AND PROTEINS DURING EMBRYO IMPLANTATION BY MALDI IMAGING MASS SPECTROMETRY

By

Kristin Elizabeth Burnum

Dissertation

Submitted to the Faculty of the

Graduate School of Vanderbilt University

in fulfillment of the requirements

for the degree of

DOCTOR OF PHILOSOPHY

in

Biochemistry

December, 2008

Approved:

Richard M. Caprioli

H. Alex Brown

Daniel C. Liebler

Jennifer A. Pietenpol

Michael R. Waterman

This work is dedicated to my parents, Kathy and Steve, who gave me everything

ACKNOWLEDGEMENTS

I would like to thank my mentor, Richard Caprioli, for all his guidance and support throughout my graduate school career. To each of my committee members, Sudhansu K. Dey, H. Alex Brown, Daniel Liebler, Jennifer Pietenpol, and Michael Waterman, thank you for all your guidance and input to help progress this project to its successful completion.

This work was supported in part by grants GM58008-9 and DOD W81XWH-05-1-0179 (RMC), HD12304 (SKD), U54 GM69338 (HAB). I would also like to acknowledge support from the NICHD Reproductive Biology Training Grant (2T HD007043-31A2) and the NCI Breast Cancer Research Training Grant (CA78136-07).

TABLE OF CONTENTS

Page

Chapter

LIST OF TABLES

LIST OF FIGURES

TECHNOLOGICAL ABBREVIATIONS

IMS, Imaging Mass Spectrometry

MS, Mass Spectrometry

MALDI, Matrix-Assisted Laser Desorption/Ionization

ESI, Electrospray Ionization

FTICR, Fourier Transform Ion Cyclotron Resonance

TOF, Time-Of-Flight

MS/MS, Tandem-MS

*m/*z, mass-to-charge

Da, Dalton

TIC, Total Ion Current

LC, liquid chromatographic

LTQ, Linear Ion Trap

SA, Sinapinic Acid

DHA, 2,5-dihydroxyacetophenone

DHB, 2,5-dihydroxybenzoic acid

SAM, Significance Analysis of Microarrays

FDR, False Discovery Rate

ICAT, Isotope Coded Affinity Tag

IHC, Immunohistochemistry

BIOLOGICAL ABBREVIATIONS

IS, Implantation Site

Inter-IS, Interimplantation Site

AM, Antimesometrial

M, Mesometrial

PDZ, Primary Decidual Zone

SDZ, Secondary Decidual Zone

EPC, Ectoplacental Cone

SM, Sphingomyelin

PC, Phosphatidylcholine

PE, Phosphatidylethanolamine

PEp, Phosphatidylethanolamine plasmalogens

PG, Phosphatidylglycerol

PI, Phosphatidylinositol

LPI, Lysophosphatidylinositol

PS, Phosphatidylserine

cPLA2α or Pla2g4a, cytosolic phospholipase A2α

COX-2, Cyclooxygenase-2

CHAPTER I

INTRODUCTION

I.A. **Embryo Implantation**

Implantation is the process by which an embryo comes into physical and physiological contact with uterine endometrium. Early pregnancy failure often arises due to defects that occur before, during or immediately after implantation. Even with *in vitro* fertilization and embryo-transfer techniques, implantation rates remain low in humans, most often as a result of embryos being transferred into nonreceptive uteri [1]. Studying the molecular interactions that regulate implantation will provide a better understanding of these signaling pathways, eventually leading to new approaches to prevent implantation failure.

Mouse models have provided insight into the molecular basis of human implantation, since there are certain similarities between mouse (**Figure 1**) and human implantation. For example, in both mice and humans decidualization and a hemochorial type of placentation take place. Also, embryos from both species embed in the antimesometrial stroma [2]. With the initiation of implantation, uterine stromal cells undergo proliferation and differentiate to decidual cells, creating an intrauterine environment conducive to embryonic development and growth. Reported functions of decidual cells include providing nutritional support to the embryo prior to establishment of a functional placenta [3], controlling embryonic trophoblast cell invasion [4], and attenuating maternal immune responses against the embryo carrying paternal genes [5]. A detailed account of cellular events crucial to successful implantation can be found in Chapter II.

Implantation involves the interplay of numerous signalling molecules, yet the hierarchical instructions that coordinate the embryo–uterine dialogue are not well understood. One major difficulty in clearly defining this discourse is the complexity of the implantation process involving heterogeneous cell types of both the uterus and blastocyst, each containing unique molecular signatures which show dynamic changes during the course of pregnancy.

While gene expression studies by *in situ* hybridization or immunohistochemistry have shown differential expression patterns of specific genes during implantation, there is no report how numerous proteins and other signaling molecules are spatially displayed at specific times and stages of implantation in the context of blastocyst-uterine juxtaposition. The goal of this study was to use Imaging Mass Spectrometry (IMS) to analyze molecular changes in the embryo and uterus during the periimplantation period, day 4 to day 8, of mouse pregnancy.

I.B. Imaging Mass Spectrometry

Matrix-Assisted Laser Desorption/Ionization (MALDI) IMS can be used to localize specific molecules such as drugs, lipids, peptides and proteins directly from fresh frozen tissue sections with a lateral image resolution up to 50 μm [6]. The size of the substructures or features of interest, for each tissue type, determines the lateral image resolution. Thin frozen sections (10-15 μm thick) are cut and thaw-mounted on target plates; subsequently, an energy absorbing matrix is applied. Laser ablation give rise to ionic molecular species that are recorded according to their mass-to-charge (*m/z*) values. Thus, a single mass spectrum is acquired from each ablated spot in the array. Signal intensities at specific *m/z* values can be exported from this array to give a two-dimensional ion density map, or image, constructed from the specific coordinate location of that signal, and its corresponding relative abundance. For images, matrix is deposited in a homogeneous manner to the surface of the tissue in such a way as to minimize the lateral dispersion of molecules of interest. Selected matrix deposition techniques are illustrated in **Figure 2, *left***. For example, to analyze proteins, peptides, drugs or phospholipids matrix can be deposited on the tissue by robotically spraying a continuous coating or by automatically printing arrays of small droplets. Recently, it has been found that ‘dry coating’ the tissue with a uniform layer of small matrix crystals (< 20 µm) can be used to obtain high lateral resolution phospholipids images [7]. As displayed in this figure, each micro spot or pixel coordinate is then automatically analyzed by MALDI Mass Spectrometry (MS). From the analysis of a single section, images at virtually any molecular weight may be obtained provided there is sufficient signal intensity to record. Examples of molecular images acquired from a day 6 implantation site tissue section are located in **Figure 2, *right***.

One of the most compelling aspects of IMS is that it provides the ability to simultaneously visualize the spatial arrangement of hundreds of analytes directly from tissue without any prior knowledge or need for target specific reagents such as antibodies. IMS also enables the visualization of post translational modifications and proteolytic processing while retaining spatial localization. Other MS techniques, such as secondary ionization mass spectrometry (SIMS), have also seen use for a variety of imaging applications. One of the major advantages of SIMS is that it is capable of high resolution imaging, around or better than 1 μm for small molecules (*m/z* <1000 Da) and elements, respectively [8]. However, thus far, it has not been shown to be effective for the analysis of proteins and large peptides.

The following sections will focus on MALDI IMS analysis of proteins and phospholipids in terms of basic instrumentation, sample preparation and recent applications. IMS has been shown to be an effective technology for discovery for both qualitative and relative quantitative analysis of normal and disease tissue and for assessing temporal changes in biological systems [6]. In addition, this technology has been applied for the generation of three-dimensional protein images of brain, whole body reconstructions and the measurement of protein changes in specific tissues after systemic drug administration [9-11].

I.B.i. The Technology

The MS instrumentation best suited for *in-situ* analysis of proteins and phospholipids directly from tissue sections is MALDI time-of-flight (TOF) technology. The ablation process directed by the focused laser beam, together with the high frequency of the laser pulse, has rendered MALDI the most widely used ionization method for imaging. The duty cycle of a modern TOF analyzer is an ideal match for the pulsed laser process and also has the advantage of a theoretically unlimited mass range, high ion transmission efficiency, multiplex detection capability and simplicity in instrument design and maintenance [12].

A brief description of a MALDI-TOF MS experiment follows for those who are not currently practitioners and who seek introductory information; more detailed information can be found in other works [13, 14]. A typical analysis of proteins directly from tissue is described for illustrative purposes. Two main experimental approaches may be used: profiling and imaging. Profiling involves analyzing discrete areas of the tissue sections and subjecting the resulting protein profiles to computational analysis. These experiments are designed to make comparisons between representative areas on a single piece of tissue, such as a normal healthy area versus a diseased area, or between two different specimens. A sufficient number of areas must be sampled to gain statistical confidence in the results; the number varies depending on the specific experiment. On the other hand, imaging requires that the entire tissue section be analyzed through an ordered array of spots, or raster, in which spectra are acquired at intervals that define the image resolution (e.g. every 50 μm in both the x and the y direction). Two-dimensional ion-intensity maps, or images, can then be created by plotting the intensities of any signal obtained as a function of its xy coordinates. The resulting images allow rapid assessment of protein localization differences between and among samples.

Tissues used for analysis should be frozen in liquid nitrogen immediately after resection to preserve the morphology and minimize protein degradation through proteolysis. The tissue is usually sectioned in a cryostat to give 10-15 µm thick sections and thaw-mounted onto an electrically conductive sample plate [13]. Sample plates include gold-coated or stainless steel metal plates and glass slides that have a conductive coating. For protein analysis, the tissue section may be gently rinsed with ethanol as a fixative and a wash to remove lipids and salts. Alternatively, IMS-compatible tissue-staining protocols can be used in conjunction with the optically transparent glass slides, allowing correlation of IMS data with histological features of the same section by optical microscopy [15].

MALDI IMS requires the application of energy-absorbing matrix. The matrix is typically a small organic molecule that co-crystallizes with the analytes of interest on the tissue surface. The matrix is capable of absorbing laser energy, thereby causing the analyte to desorb intact from the sample surface and ionize. The most commonly used matrices include 3,5-dimethoxy-4-hydroxy-cinnamic acid (SA), 2,5-dihydroxybenzoic acid (DHB), 2,5-dihydroxyacetophenone (DHA), and α-cyano-4-hydroxycinnamic acid (CHCA). Solvent combinations and the matrix used will vary depending on the type of molecule and tissue being investigated [13]. A 50:50 – 70:30 (v/v) of acetonitrile/water or ethanol/water mixture is generally recommended for use in protein and phospholipid analyses [16, 17]. SA is an excellent matrix for the analysis of proteins [13], DHB, DHA and HCCA are primarily used for the analysis of phospholipids, peptides and lower molecular weight analytes.

For high resolution imaging, the matrix solution should be homogenously deposited across the tissue section in such a manner as to avoid significant lateral migration of analytes. Currently, this is achieved by applying matrix solution to the tissue in either a spotted array or a homogenous spray coating [13]. A continuous and homogenous spray coating allows the highest spatial resolution, but densely spotted arrays show higher reproducibility and generally better spectra quality. Heterogeneous matrix coating gives rise to hot and cold ablation spots due to random crystal formation, thus producing poor, highly pixilated images. Several robotic spotting devices are commercially available and utilize acoustic [18], piezoelectric [19], inkjet printer [20], and capillary deposition techniques [21]. Several robotic spray coating devices are also commercially available and utilize a mist nebulizing method [22] or a thermal spray method [23]. Sublimation of matrix can also be used to produce an even layer of small crystals across the tissue section for lipid analysis [24].

Areas are ablated with an UV laser, typically having a target spot size of 50-100 µm in diameter. It is possible to image features smaller than the laser beam using an oversampling technique [25]. This technique involves the complete ablation of the MALDI matrix coating at each sample position and moving the sample target a distance less than the diameter of the laser beam before repeating the process.

Protein analysis is usually performed on a linear TOF instrument to attain the highest achievable sensitivity. Ions formed and desorbed during the laser pulse are extracted and accelerated into the field-free drift region of the TOF analyzer. Ions are usually detected by a multi-channel plate detector and the flight time of the various ions is inversely related to their *m/z* values. This time measurement is then converted to *m/z* through appropriate calibration procedures. For the analysis of low molecular weight species; such as, peptides and phospholipids, an ion mirror or reflectron can be used in the ion flight path to compensate for the initial velocity/energy distribution and improve resolution [26].

Instruments utilizing MALDI Fourier transform ion cyclotron resonance (FTICR) [27, 28] and MALDI ion trap [29, 30] technologies can be advantageous in the analysis of lower molecular weight species. MALDI FTICR technologies offers 10–100 times higher mass resolution and mass accuracy than any other mass analysis technique [31]. MALDI ion trap technologies allow for coupling tissue imaging to tandem MS^n enabling concurrent molecular identification [29]. Other analyzer combinations have been used with MALDI IMS including TOF-TOF [19], orthogonal TOF and orthogonal Quadrapole-TOF (Q-TOF) [32, 33], and ion mobility [34]. Although it is beyond the scope of this section to describe these in more detail, the reader is referred to other works for more thorough descriptions of these mass spectrometry technologies [6, 19, 27, 29, 32-34].

I.B.ii. **Reproducibility**

To assess changes in protein concentrations in a given tissue, pixel-to-pixel reproducibility must be high, that is, two pixels close together having the same protein concentrations should give the same spectra within acceptable standards. Although these standards vary from experiment to experiment, typically variations of ±15% (or less) are deemed acceptable. Factors directly affecting this aspect of the analysis include ionization efficiency of a given molecule, ion suppression effects, extraction efficiency of the matrix deposition process and the robustness and effectiveness of post acquisition processing. High pixel-to-pixel reproducibility can be achieved if careful attention is paid to sample preparation and matrix application. In addition, instrument parameters such as voltage settings and laser power must be kept constant within an experiment. A robotic matrix application device is invaluable in removing operator to operator variations. In a recent study of protein distribution in brain, relative standard errors of 3.7–9.6% were obtained between striatal regions in multiple animals [32]. Nevertheless, one must keep in mind that because ionization processes can be affected by the physical and chemical processes of molecules, it is difficult to estimate relative concentrations of two completely different proteins by comparing their peak heights alone.

I.B.iii. **Data Processing and Analysis**

To assess reproducibility, one must perform two general types of data analysis: pre-processing and statistical analysis. The pre-processing step reduces the experimental variance between spectra through the removal of background, normalization of the peak intensity to the total ion current, and peak alignment algorithms. Normalization of the spectra minimizes variation arising from day-to-day instrument fluctuations, differences in matrix crystallization across tissue sections, and changes in sample preparation and chemical properties of the underlying tissue [35]. Various algorithms are employed for all of the spectra processing steps; baseline subtraction, peak alignment, normalization and peak picking. Ion images are generated directly from these processed data sets.

The next phase of data processing involves downstream events such as calculation of average spectra for each specimen type or targeted area in the tissue (as determined by the investigator) and subsequent statistical analysis procedures. Principle Component Analysis (PCA) can be performed to reduce the dimensionality of a data set using processes to extract, display and rank the variance within a data set. By identifying patterns in data, the investigator can more easily determine similarities and differences [36]. Significance Analysis of Microarrays (SAM) can be performed to assign a score to each feature on the basis of change in its spectral intensity relative to the standard deviation of repeated measurements. For features with a score greater than a predetermined threshold, SAM uses permutations of the repeated measurements to estimate the percentage of features identified by chance, the false discovery rate (FDR) [37]. This algorithm is used to elucidate features that change significantly between two groups of specimens. A hierarchical clustering analysis (HCA) may also be applied to the data set, enabling samples to be grouped blindly according to their expression profiles. HCA functions by calculating the dissimilarity between the individual analyses [38].

I.B.iv. **Biological Applications of IMS**

Over the past decade, proteomics has become a vital complement to genetic analysis in the investigation of nearly all aspects of the life sciences including elucidation of cellular processes in both health and disease [39-41], and the evaluation of pharmaceutical compounds [42-47]. Lipidomics has gained interest in the scientific community because lipids have been found to have unique biological roles distinct from their function as a source of energy or as a simple construction unit of a membrane. Mass spectrometry has emerged as an important analytical tool for the investigation of these molecules. In particular, MALDI IMS provides the investigator with the ability to analyze the spatial distribution of proteins and phospholipids directly in tissue specimens.

I.B.iv.a. Molecular Images of Disease

Considerable effort has been focused on finding molecular markers as early indicators of disease. MALDI IMS provides a means to visualize molecularly specific information while maintaining spatial integrity. For example, cancer progression is dependent on essential characteristics such as: self-sufficiency in growth signals, insensitivity to growth-inhibitory signals, evasion of apoptosis, high replicate potential, sustained angiogenesis, and tissue invasion and metastasis [48]. Alterations in protein expression, proteolytic processing and post-translational modifications all contribute to this cellular transformation. IMS analyses of tissue sections reflect the overall status of the tissue, therefore, analyses of tissues in various states can reveal differences in the expression of proteins which otherwise could not be predicted. IMS has been used to image protein distributions in multiple types of cancer. Imaging analysis has been use to probe proteome changes in mouse breast and brain tumor [49, 50], glioblastoma biopsies [16], human lung metastasis to the brain [51], and prostate cancer [52, 53]. Identifying features that display differential expression patterns between cancerous and normal tissue can provide valuable insight into the molecular mechanisms of cancer, provide molecular diagnostic and prognostic signature, and identify possible drug targets in implicated pathways.

Three-dimensional MALDI IMS was first reported in 2005 for the analysis of myelin basic protein isoform 8 in the corpus callosum of a mouse brain [54] and more recently, it was used to explore three-dimensional protein volumes in the substantia nigra in a mouse model of Parkinson’s disease [55]. The acquisition of three-dimensional molecular images also raises the exciting possibility of combining these MS images with Magnetic Resonance Imaging (MRI) and perhaps Positron emission tomography (PET) imaging, so that the molecularly specific MS data could be co-registered with these complementary imaging technologies. MRI technology relies on the relaxation properties of excited hydrogen nuclei in water and lipids after exposure to a powerful, uniform magnetic field [56].

Figure 3 shows the results of experiments wherein IMS and MRI were combined to analyze a mouse brain injected with glioma cells and to visualize the data in three dimensions [9]. The entire mouse head was sectioned from the olfactory bulb to the beginning of the spinal cord. Coronal sections of the mouse brain were collected at 20 μm increments as a high-resolution camera acquired blockface images every 40 μm. Tissue sections for IMS analysis were collected every 160 μm, coated with SA and imaged at 150 μm lateral resolution. In

Figure 3 (*right*), Histone H2B, is associated with the tumor as it manifests in the contra-lateral ventricle. Conversely, in **Figure 3 (*left*)**, the myelin basic protein isoform 4 image demonstrates that the corpus callosum can be accurately spatially correlated in a three-dimensional sample-specific context. A good correlation of the tumor between MALDI ion intensities, contrast variation in the magnetic resonance parameters, and the optical volume were observed.

IMS has also been utilized to study neurodegenerative diseases such as Alzheimer's and Parkinson's. Neurodegeneration is widespread in Alzheimer's disease, affecting several brain regions. ß-Amyloid plaques accumulate causing plaque formation and subsequent neurodegeneration [57, 58]. A mutation of the amyloid precursor protein gene causes a higher production of ß-amyloid and ß-amyloid peptides in the cortical and hippocampal structures of the brain. MALDI images showed that the ß-amyloid peptides (1-40) and (1-42) were the most abundant amyloid peptides in those brain regions in an Alzheimer's disease mouse model [59].

From previous studies of Parkinsonism, a condition that affects regions of the brain that control motor function (such as the substantia nigra and the striatum), it was found that dopamine neurons in the nigrostriatal pathway are gradually decreased in the striatum. IMS technology has been applied to the 1-methyl 4-phenyl 1,2,3,6-tetrahydropyridine (MPTP) animal model of Parkinsonism [60]; the investigators found that purkinje cell protein 4 (PEP-19), a neuronal calmodulin-binding protein, was significantly reduced (by 30%) in the striatum compared to control regions in normal brain. Further study is needed to determine the specific involvement of PEP-19 in neurodegeneration.

I.B.iv.b. **Proteome Response to Drug Administration**

In addition to assisting in disease differentiation and diagnosis, the proteome signature of a tissue can also be used for determining the effects of drug/small-molecule administration to an animal model or patient. Over the past decade, proteins have become principal targets of drug discovery, and proteomics-oriented drug research has come to the forefront of activity in this area. Proteomics plays a major role in drug development, specifically in target identification, target validation, drug design, lead optimization, and pre-clinical and clinical development [61].

Pharmaceutical drug discovery is a laborious and tedious process: it can take from 8 to 10 years, at great expense, to bring a drug candidate onto the market [42]. Obviously, it is essential to find ways to expedite this process. With the early assessment of the distribution of a drug candidate in targeted tissues, IMS can greatly assist in the discovery and validation of processes related to drug administration, distribution, metabolism and excretion (ADME) [62, 63]. For example, IMS can individually detect the presence and location of an individual drug and its metabolites in a label-free protocol, a significant advantage over other small molecule imaging techniques that typically require the addition of a radioactive tag to the molecule of interest, such as in autoradiography. Another advantage of IMS is that it is capable of providing information on both the pharmacological and biological effects of a drug in that it can detect molecular features that may be markers of drug efficacy or toxicity. Other imaging techniques give little information on the molecular identity of these biological endpoints. Thus, IMS can monitor the analyte of interest and also the corresponding proteome response. For example, investigators have discovered transthyretin as a marker for gentamicin-induced nephrotoxicity in rat [11]. Gentamicin-induced nephrotoxicity is seldom fatal and is usually reversible but often results in long hospital stays. Thus, there is great interest finding potential markers of early toxicity and also to help elucidate the molecular mechanism. Investigators utilized MALDI IMS to determine differential protein expression within the rat kidney (cortex, medulla, and papilla), identified features of interest between dosed and control rat, and then applied downstream protein identification procedures. Transthyretin signal was significantly increased in the treated mouse kidney over control and these findings were validated with western blot and immunohistochemistry.

To study the relationship between the drug distribution in tumors and the resulting protein alterations, mass spectral images were obtained from MMTV/HER2 tumors excised from mice [50]. Investigators were able to identify markers that indicate a response of the tumor to administration of erbB receptor inhibitors OSI-774 and Herceptin. Inhibition of tumor cell proliferation, induction of apoptosis, and tumor reduction were predicted by a >80% reduction in thymosin ß4 and ubiquitin levels that were detectable after 16 hours of a single drug dose before any evidence of *in situ* cellular activity.

These same procedures discussed for excised organs or tumors can also be applied to whole-body animal tissue sections for a system-wide analysis in a single experiment [32]. For whole-body sagittal tissue sections, using the same sample preparation and analysis conditions described for IMS experiments of tissues, signals unique to individual organs were detected and used to produce a two-dimensional protein map of a control rat (**Figure 4**). By expanding the capabilities of MALDI IMS to investigate multiple tissue types simultaneously across a whole-body tissue section, distinct protein patterns can be identified and used to monitor whole-body systems dynamics.

I.B.iv.c. ***In situ*** **Proteomics**

Because the MALDI desorption process leads to the measurement of the molecular weight of a given protein, off-line techniques involving extraction, liquid chromatographic (LC) separation, digestion and LC-MS/MS analyses with database searches are performed to identify a protein. These approaches are effective, but are very time consuming and costly. Direct *in situ* protein identification provides a significant advantage in such cases. Investigators have developed a protocol that allows digestion of proteins directly on thin tissue sections using well defined microspotted arrays of enzymes that can subsequently be spotted with matrix for IMS and MALDI MS/MS analyses [19]. Although any enzyme can be used, the serine protease, trypsin, is the most common choice because it has a very well defined specificity in that it preferentially hydrolyzes the peptide bond at the carboxyl side of the amino acids lysine (K) and arginine (R). In one such study (**Figure 5**); trypsin spots (150 μm diameters) were deposited in an array (spots located 200 μm apart) on a section of mouse brain. For two specific proteins, neurogranin and PEP-19, four tryptic peptides from each were identified and sequenced by MALDI MS/MS directly from the tissue digest spots. The image of each peptide was then constructed (**Figure 5**).

The application of IMS to the analysis of formalin-fixed paraffin embedded (FFPE) tissue sections has also been undertaken. FFPE is the most convenient method to preserve samples in hospital tissue banks; this method is of great interest as millions of tissue samples are stored worldwide, many of which are linked to detailed patient histories and outcomes. However, analysis of the proteins in formalin fixed tissues is a major challenge: the fixation process alters the structures of the proteins by cross-linking, thereby changing the molecular weight, often in unpredictable ways. Recent studies have focused on protocols utilizing antigen retrieval, *in situ* trypsin digestion and subsequent IMS analysis to analyze such samples and thus far have shown promise. For example, IMS was used to analyze a two-year-old archived FFPE rat brain tissues and the results showed the same localization of various proteins as that of the proteins within frozen tissue sections [64].

Preserved FFPE tissues are often collected into tissue microarrays, which consist of paraffin blocks in which hundreds of separate tissue cores are assembled in array fashion to allow simultaneous histological analysis. In one study, microarray FFPE tissues, containing 112 needle core biopsies from lung-tumor patients, were analyzed by IMS following antigen retrieval and on-tissue tryptic digestion protocols [65]. This high-throughput approach allows investigators to detect and characterize tumor marker proteins from a large cohort of microarray samples.

I.B.iv.d. Phospholipid Imaging

MALDI IMS has been used to analyze glycerophospholipids, phosphate-containing glycerol-based lipids, which are the main component of biological membranes. The major classes of these phospholipids, grouped according to the headgroup identity, are phosphatidylcholine (PC), sphingomyelin (SM), phosphatidylinositol (PI), phosphatidylserine (PS), phosphatidylglycerol (PG) and phosphatidylethanolamine (PE). Many molecular species exist within each class containing different combinations of fatty acids in the sn1 and sn2 position of the glycerol backbone.

Several MALDI IMS studies have focused on mapping phospholipid distributions in brain tissue sections [17, 66-69]. Lipids are one of the most abundant biomolecules found in the brain, second only to water. Lipids make up 50% of the dry weight of the brain and play an important role in brain anatomy, physiology and pathophysiology. Altered levels of phospholipids are associated with Farber disease, Gaucher disease, Niemann-Pick disease, Alzheimer disease, and Down syndrome [70-73]. IMS analysis of rat brain sections found PI 38:4 and PC 36:1 localize mainly to the gray matter, conversely, PC 32:0 localizes mainly to the white matter [74]. This inverse relationship between PC

36:1 and PC 32:0 was documented in another IMS study and the corresponding images are depicted in **Figure 6** [7]. Although, these IMS results are supported by earlier studies [75] to begin to understand the biology implications of these images each fatty acid chain needs to be identified. This will be discussed more in Chapter III, where phospholipid fatty acid chains were identified directly from mouse implantation site tissue sections by FTICR and Tandem MS analyses.

MALDI IMS has an advantage over thin-layer chromatography (TLC) and LC-Tandem-MS, in that, the anatomical integrity of the sample is maintained. TLC and LC-Tandem-MS techniques require homogenization prior to lipid analysis [76, 77]. Immunostaining of the phospholipid head group can be used to obtain spatial information on phospholipids, but this technique cannot distinguish between the unique molecular species for each phospholipid class [78]. Imaging mass spectrometry can visualize the spatial distribution of different phospholipid species (e.g. same headgroup different fatty acid chains [**Figure 6**]).

In addition to MALDI-MS, other mass spectrometric techniques such as desorption electrospray ionization mass spectrometry (DESI) [79] and secondary ion mass spectrometry (SIMS) [8, 80, 81] have also been used for lipid imaging studies. New technologies, such as, MALDI-ion mobility-TOF MS imaging with gold nanoparticles as matrices enabled low abundant cerebroside species to be imaged in a rat brain section [82]. Cerebroside cannot be seen with traditional MALDI IMS methods because they are suppressed by the highly abundant PC which account for approximately 50% of phospholipid mass in cell membranes [83, 84]. In another study, tandem Imaging MS was successfully used for the structural characterization of isobaric PCs, PEs, PSs and DHB clusters while maintain the spatial localization of each species [66]. Overall, technological advancements in IMS has allowed for sensitive and very selective analyses of lipids with diverse chemical compositions, therefore, advancing the lipidomics field in biomedical research [85].

I.B.iv.e. New Insights into Biology

MALDI IMS of tissue sections can provide information on the spatial and temporal action of proteins involved in processes that take place in organs or tissue substructures that contain heterogeneous cell types. A major advantage of MALDI IMS is that it allows the investigator to visualize molecular events while retaining spatial information that would have been lost using techniques that require tissue homogenization and extraction.

In a project involving mammalian reproduction [86], investigators evaluated protein expression during normal mouse prostate development (1-5 weeks of age), at sexual maturation (6 weeks of age), and in adult prostate (at 10, 15, or 40 weeks of age) [53]. This same study compared temporal protein expression in the prostate between healthy mice and mice with prostate tumors (LBP-Tag mouse model for prostate cancer). The expression of probasin and spermine-binding proteins was significantly decreased in prostate tumor formation. Cyclophilin A was differentially α-acetylated on the n-terminus, during normal prostate and prostate tumor development. In summary, tissue profiling and imaging were able to identify proteins related to prostate morphogenesis and tumorigenesis.

I.C. Summary and Research Objectives

Due to the fact that there is a high degree of molecular complexity in biological systems, new tools are needed to elucidate molecular events in both spatial and temporal distributions. IMS provides unique information of peptides, proteins and phospholipids directly from complex tissue surfaces, bringing powerful new capabilities to biological research. IMS requires relatively easy sample preparation and is well suited to high-throughput analysis (on the order of seconds per sample). Most importantly, it is an excellent discovery tool in research, providing that the analytes investigated do not need to be known in advance. Hundreds of signals can be extracted from a single experiment with relatively high mass measurement accuracy. Because the spatial integrity of the tissue is maintained, molecular images and patterns can easily be correlated with histopathological analyses.

The objective of our analysis was to use IMS to investigate the mammalian reproductive process involving implantation and early development of the embryo. The heterogeneous cell types of the uterus, each with unique function, pose a challenge for studying events during early pregnancy. In rodents and humans, one of the limiting factors is the availability of adequate amounts of tissues for biochemical and molecular biology experiments. Studying the uterine molecular landscape using conventional approaches presents an arduous task since some molecules localize to particular cell types on a specific day of pregnancy and do not reappear later in the process. Disregulation of events prior to, during, or immediately after implantation contributes to poor pregnancy rates. Therefore, understanding molecular localization patterns during implantation is essential to provide potential targets for treating infertility and developing novel contraceptive approaches.

In preliminary IMS experiments, we studied implantation sites from mice on day 6 (D6) and day 8 (D8) of pregnancy and obtained molecular distributions that were unique to embryo, surrounding muscle and uterine stroma within an area measuring ≤3 mm^2. The ion-intensity maps presented in **Figure 7** illustrate the power of IMS in viewing how molecular location and expression changes during early pregnancy. The ions depicted in red and green are expressed in the presence of the embryo only on D6 through D8 of pregnancy. The ion shown in red is expressed at the site of the embryo and increases by D8. The uterus has two poles; the mesometrial pole (M), where the blood supply enters the uterus, and the antimesometrial pole (AM), where the embryo implants. The ion depicted in purple remains at the AM pole in these images, whereas the ion depicted in green shifts solely to the AM pole by D8. The ion shown in blue represents the muscle surrounding the uterus. The correlation of molecular information to anatomical structures in implantation sites offers tremendous potential for a better understanding of biological processes essential to embryo implantation.

Briefly, in Chapter II we detail the cellular events associated with mouse embryo implantation. In Chapter III & IV we explore phospholipid and protein localization on days 4-8 of mouse pregnancy, respectively. In Chapter V, we analyze the expression of these molecules in context with the cellular transformations of the uterus and the embryo. From this analysis we found that small structural changes in phospholipids have a huge impact on the biological activity and distribution across the implantation sites. Also, biological processes essential to embryo implantation are highly regionalized and take place in very discrete time domains.

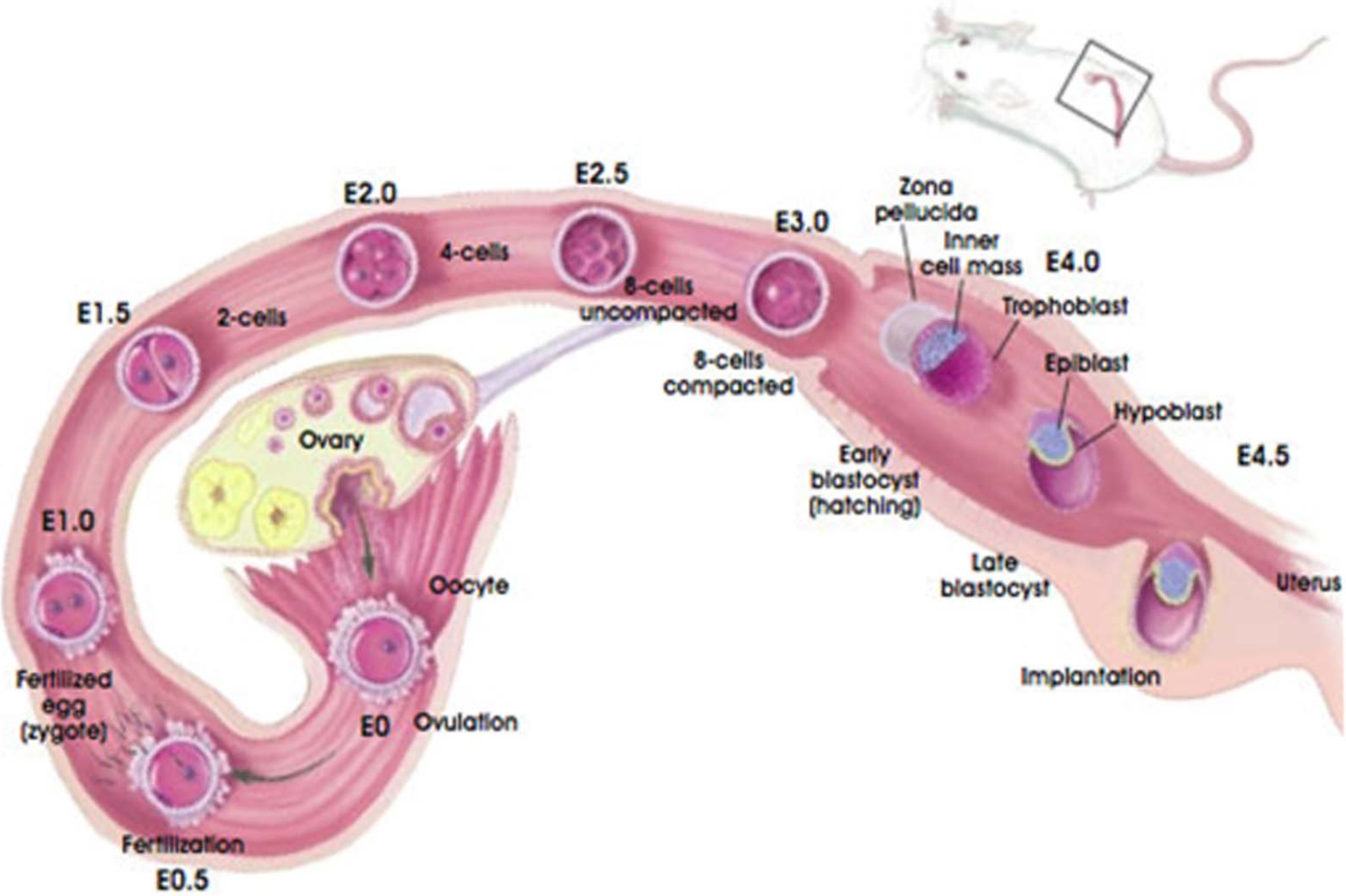

Figure 1. Mouse Embryo Implantation.

Adapted from: National Institutes of Health. Stem Cells: Scientific Progress and Future Research Directions. Stem Cell Information [online], http://stemcells.nih.gov/info/scireport (2001) Terese Winslow.

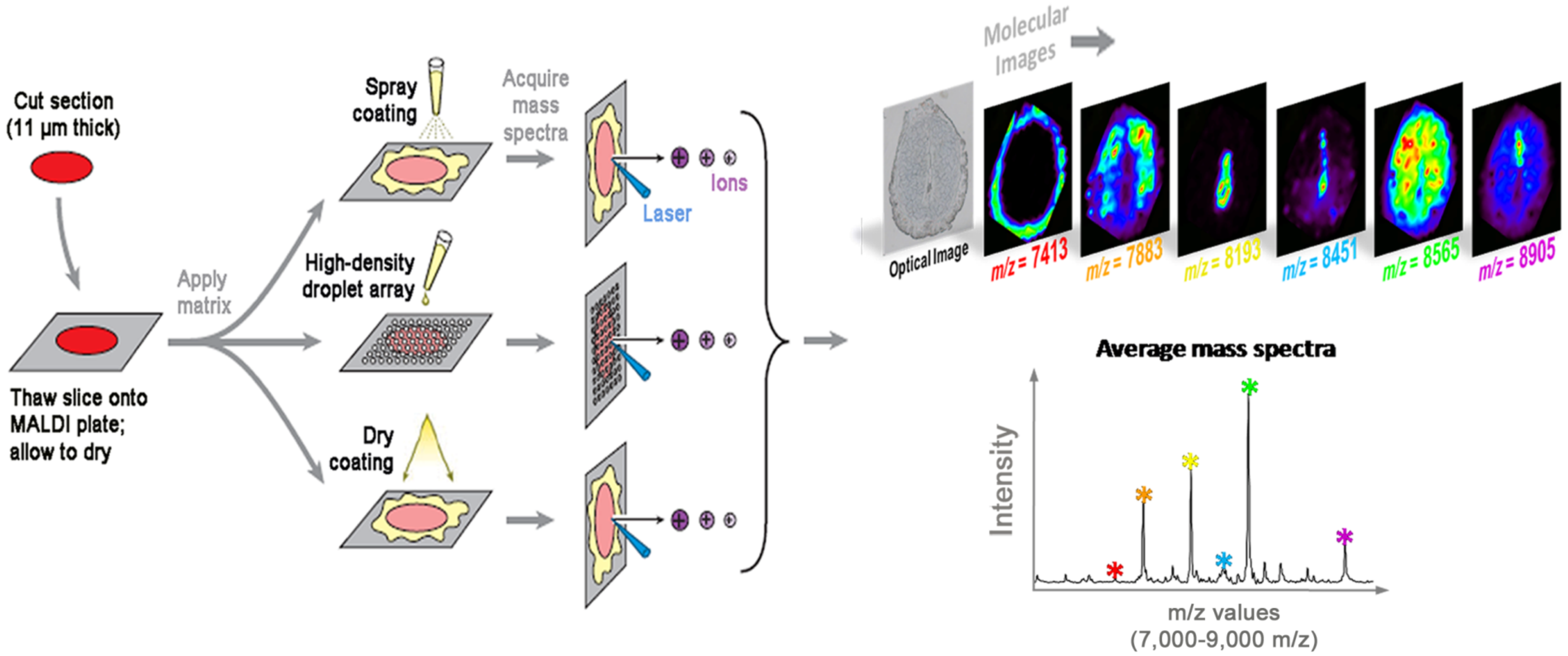

Figure 2. Scheme of a typical direct tissue imaging experiment. (Left) Three types of matrix application are shown: spraycoating, high-density droplet array, and dry coating. Subsequent image acquisition is shown for each technique. **(Right)** Selected Molecular images (top) and average mass spectra (bottom) from a mouse implantation site on day 6 of pregnancy. Abbreviation: MALDI, matrix-assisted laser desorption/ionization.

Image adapted from: Burnum, K.E. et al. Annual Review of Analytical Chemistry 1, 689-705 (2008)

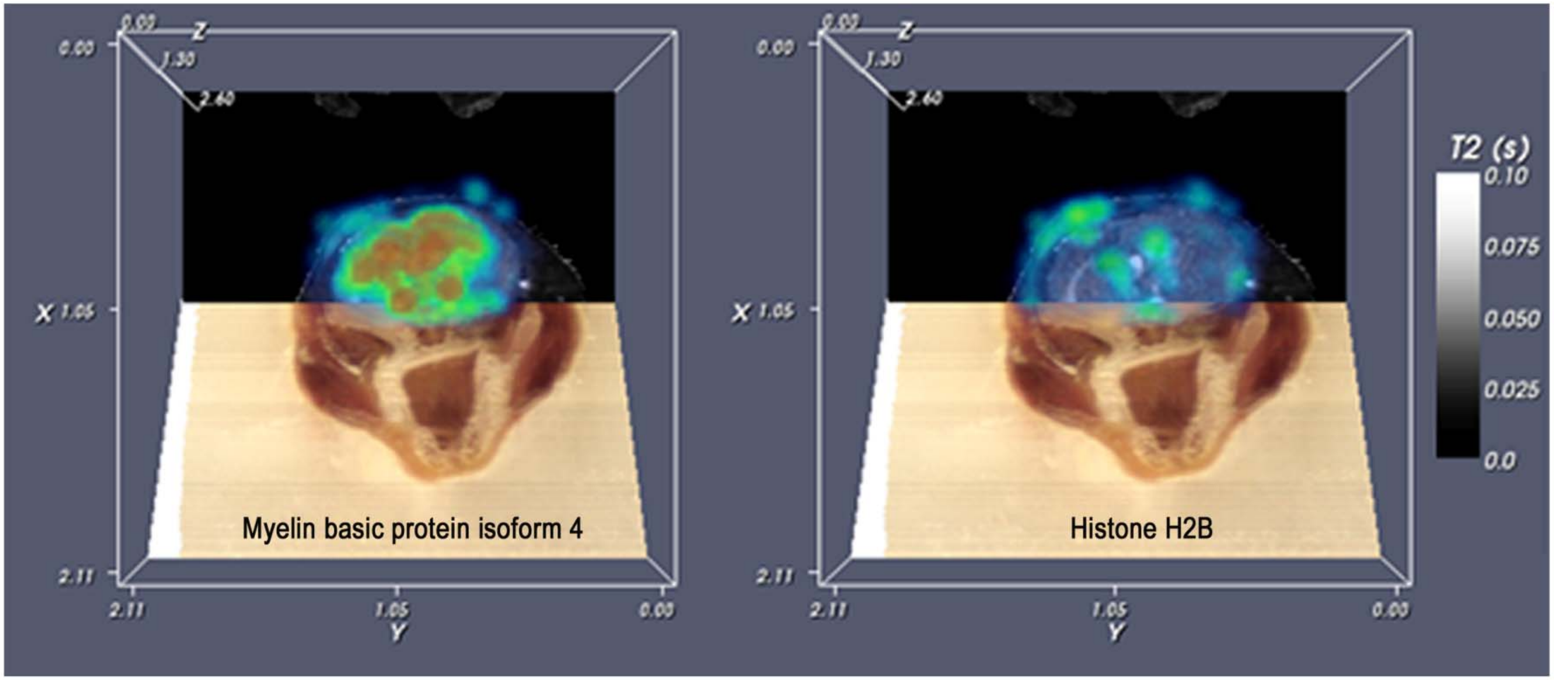

Figure 3. Imaging mass spectrometry analysis of a glioma tumor mouse brain. Spatially resolved three-dimensional IMS volumes coregistered to in vivo magnetic resonance imaging data and the optical volume of a glioma tumor mouse brain.

Image adapted from: Burnum, K.E. et al. Annual Review of Analytical Chemistry 1, 689-705 (2008)

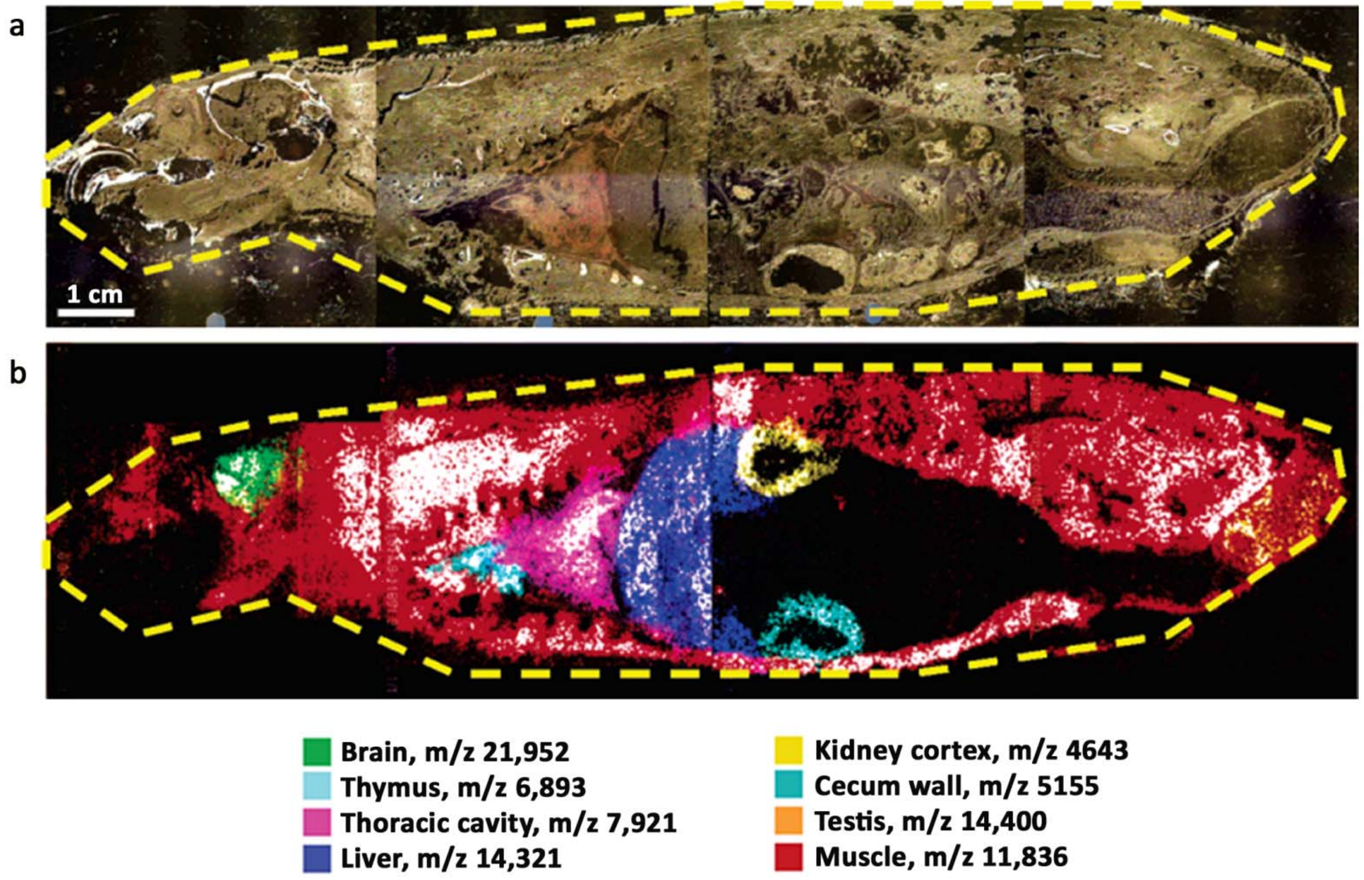

Figure 4. Whole-body protein analysis of rat sagittal tissue section by imaging mass spectrometry. **(a)** Optical image of rat sagittal tissue section across four gold matrix-assisted laser desorption/ionization target plates. **(b)** Ion image overlay of unique organ signals.

Reprinted with permission from: Khatib-Shahidi S., et al. Analytical Chemistry 78, 6448–56 (2006) American Chemical Society

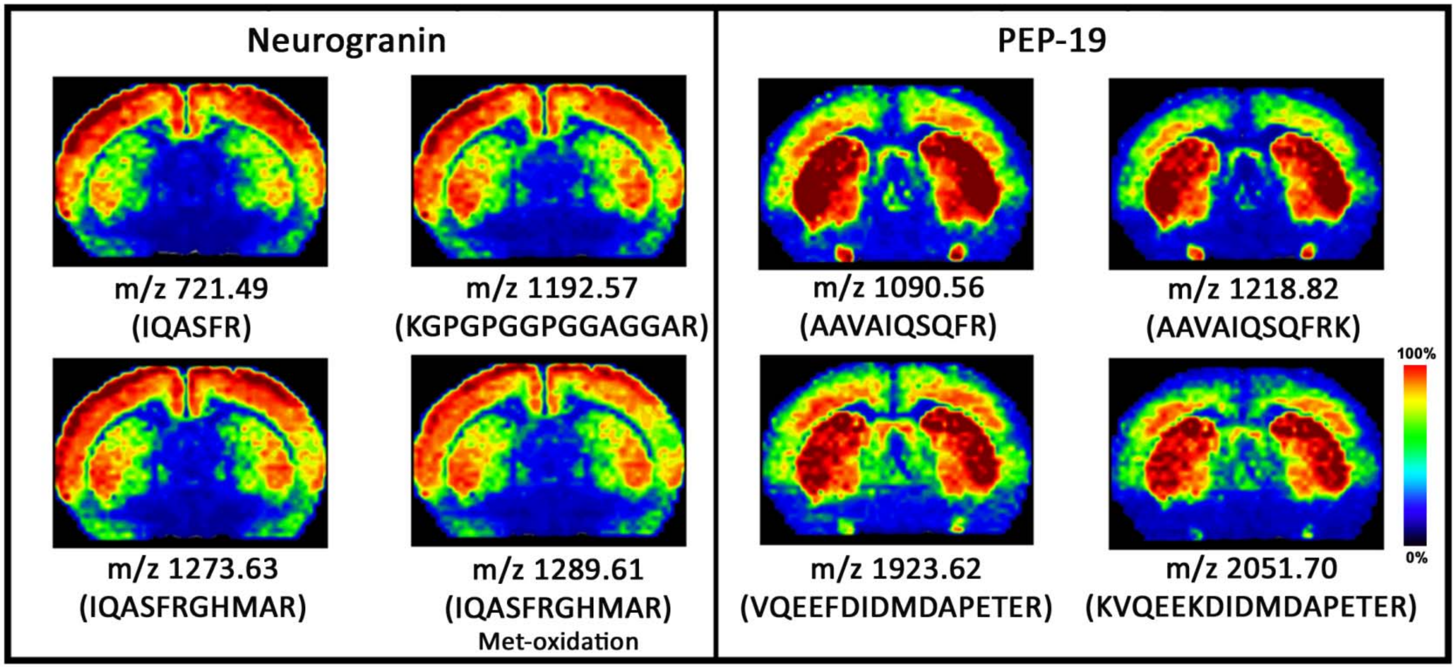

Figure 5. Examples of on-tissue tryptic digestion and subsequent matrix-assisted laser desorption/ionization imaging mass spectrometry analysis. (Left) Tryptic peptides generated from the digestion of the 7.5-kDa protein, neurogranin. **(Right)** Tryptic peptides generated from the digestion of the 6.7-kDa protein, PEP-19.

Reprinted with permission from: Groseclose M.R., et al. Journal Mass Spectrometry 42, 254–62 (2007)

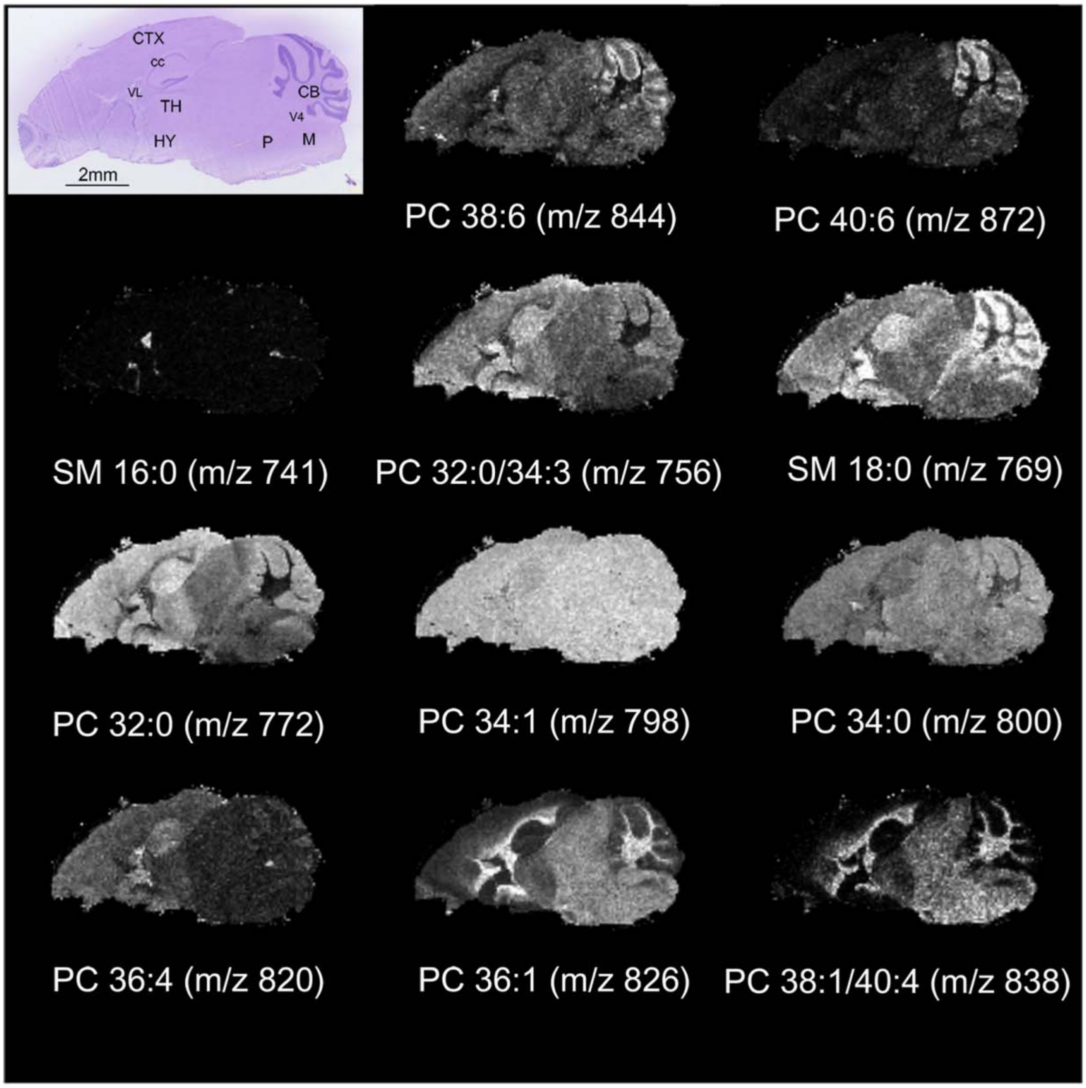

PC 38:6 (m/z 844)
PC 40:6 (m/z 872)
SM 16:0 (m/z 741)
PC 32:0/34:3 (m/z 756)
SM 18:0 (m/z 769)
PC 32:0 (m/z 772)
PC 34:1 (m/z 798)
PC 34:0 (m/z 800)
PC 36:4 (m/z 820)
PC 36:1 (m/z 826)
PC 38:1/40:4 (m/z 838)

Figure 6. Imaging mass spectrometry analysis of a sagittal mouse brain to determine the spatial localization of multiple phosphatidylcholine (PC) species. Number before the colon, total number of carbons in the two fatty acid chains; number after the colon, total number of double bonds in the two fatty acid chains.

Image adapted from: Puolitaival, S.M.; Burnum, K.E. et al. Journal of the American Society for Mass Spectrometry 19, 882-886 (2008)

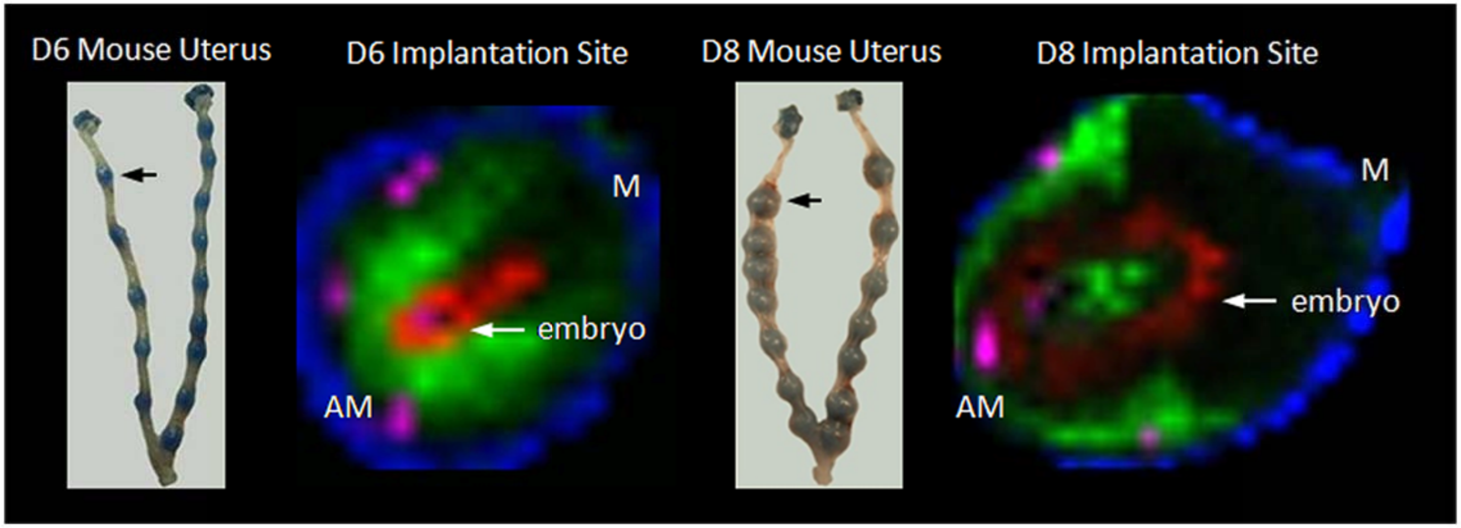

Figure 7. Optical images of a day 6 (D6) and day 8 (D8) pregnant mouse uterus along with the corresponding ion images (arrows indicate the implantation site). D6 implantation site and D8 implantation site ion-density maps obtained for: m/z 5924 (purple), m/z 4040 (green), m/z 6718 (blue), m/z 8194 (red). Abbreviations: AM, antimesometrial; M, mesometrial.

Image adapted from: Burnum, K.E. et al. Annual Review of Analytical Chemistry 1, 689-705 (2008)

CHAPTER II

STAGES OF MOUSE EMBRYO IMPLANTATION

Establishment of a receptive uterus to support embryo development and implantation depends on coordinated effects of ovarian steroid hormones estrogen and progesterone (P_4) [2]. Studies in mice using embryo transfer experiments have shown that uterine receptivity occurs for a limited period during pregnancy: the prereceptive uterus on days 1-3 becomes receptive on day 4 and nonreceptive by late day 5 of pregnancy [87]. In mice, implantation sites are evenly spaced with implantation and interimplantation sites differing in molecular composition, the former influenced by the embryo and the latter without such influence. Once implantation occurs on the evening of day 4 of pregnancy, the uterine stroma surrounding the embryo at the implantation site undergoes extensive remodeling, a process termed decidualization. Thus, it is highly expected that differential molecular signatures are represented not only by implantation and interimplantation sites, but also by the cellular regions within these sites.

The initial attachment reaction between the embryo and the luminal epithelial cells lining the inside of the uterus occurs approximately between 2200 – 2300 h on day 4 of pregnancy (vaginal plug = day 1). This attachment is accompanied by an increased endometrial vascular permeability at the sites of blastocysts, which can be visualized as distinct blue bands after an intravenous injection of a Chicago Blue dye solution [88]. This blue dye method is a useful tool, since implantation and interimplantation sites can be separately excised, and sections with and without the implanting embryo can be obtained for differential characterization. **Figure 8** shows day 5 and 6 mouse uteri with blue bands (implantation sites) along with resulting implantation site sections. On day 8 of pregnancy, blue dye injection is not necessary, since implantation sites are larger and visually distinguishable (**Figure 8**). Following the attachment reaction, in a process termed luminal closure, the inner canal of the uterus collapses in on itself resulting in an intimate apposition of the embryo with the luminal epithelium [89, 90]. This luminal closure reaction is evident in the day 5 implantation site section of **Figure 8** since all that remains of the inner canal is a thin line of luminal epithelium cells which stretch from the embryo to the Mesometrial Pole. On the afternoon of day 5 of pregnancy, the proliferating stromal cells bordering the implanting embryo begin to differentiate into decidual cells, forming the avascular primary decidual zone (PDZ). By day 6, the PDZ completes differentiation, and a secondary decidual zone (SDZ) forms around the PDZ. Although proliferation is terminated in the PDZ, it continues in the SDZ. The PDZ then progressively degenerates through day 8 of pregnancy. On day 8 of pregnancy the SDZ decidual cells surrounding the embryo at the antimesometrial (AM) pole undergo apoptosis to create space for the growing embryo; whereas, the region containing decidual cells at the mesometrial (M) pole undergoes angiogenesis forming a vascularized zone that brings maternal and fetal blood vessels in close proximity, a prerequisite for the formation of a functional placenta [2]. This maternal-fetal interface is achieved by rapid multiplication of embryonic trophoblast cells towards the M pole, resulting in the formation of an ectoplacental cone (EPC) by day 8 of pregnancy.

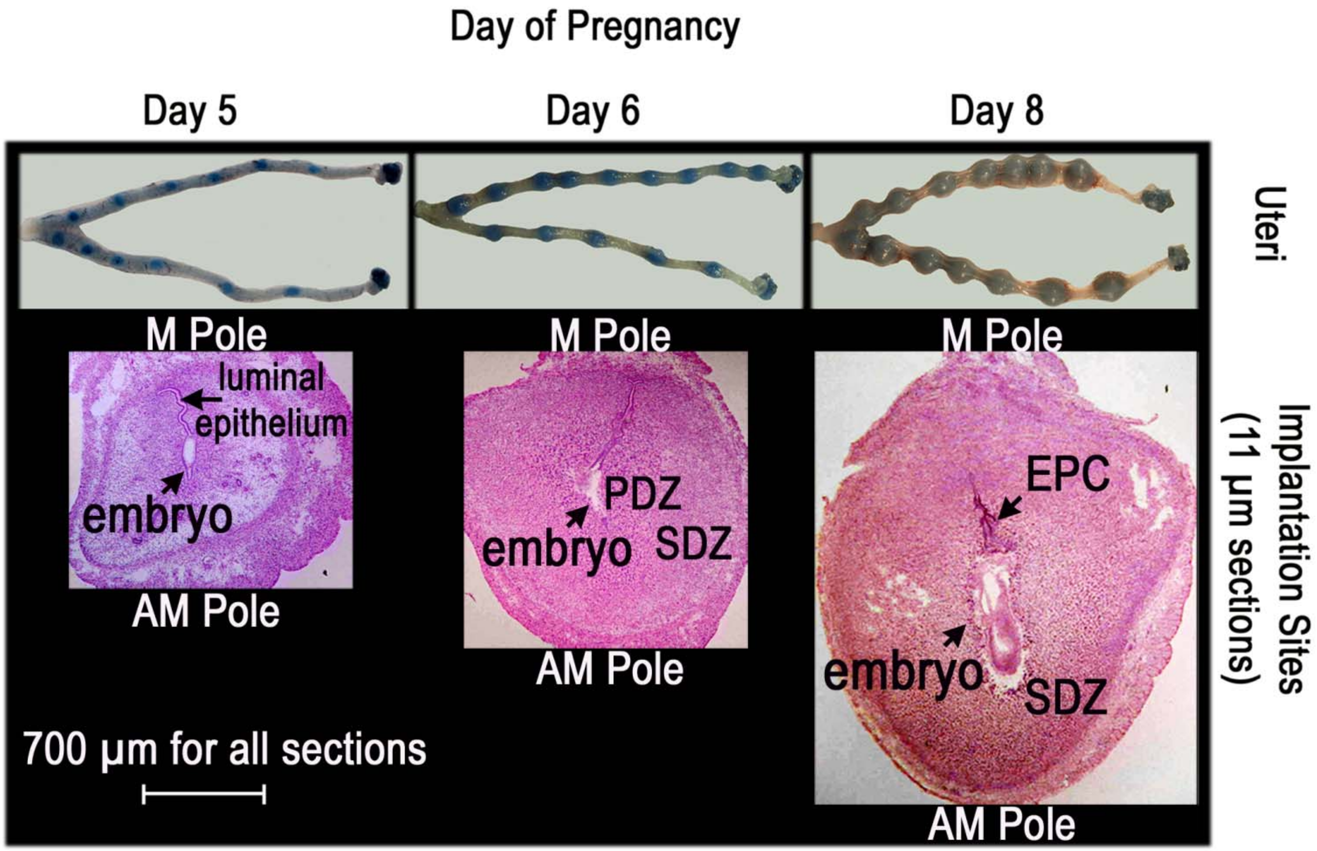

Figure 8. Morphological changes in the mouse uterus from day 5 to day 8 of pregnancy. The three panels contain optical photographs of uteri (top of each panel) and uterine implantation site sections (bottom of each panel) collected on days 5, 6, and 8 of pregnancy. Abbreviations: M, mesometrial pole; AM, antimesometrial pole; PDZ, primary decidual zone; SDZ, secondary decidual zone; EPC, ectoplacental cone.

CHAPTER III

DETECTING SPATIAL AND TEMPORAL DISTRIBUTIONS OF PHOSPHOLIPIDS DURING EMBRYO IMPLANTATION BY MALDI IMAGING MASS SPECTROMETRY

A. **Overview**

Molecular events involved in successful embryo implantation are not well understood. In this study, we used MALDI Imaging Mass Spectrometry technologies to characterize the spatial and temporal distribution of phospholipid species associated with mouse embryo implantation. Molecular images showing phospholipid distribution within implantation sites changed markedly between distinct cellular areas during days 4-8 of pregnancy. For example, by day 8, linoleate- and docosahexaenoate-containing phospholipids localized to regions destined to undergo cell death, whereas oleate-containing phospholipids localized to angiogenic regions. Arachidonate-containing phospholipids showed different segregation patterns depending on the lipid class, revealing a strong correlation of phosphatidylethanolamines and phosphatidylinositols with cytosolic phospholipase $A_{2\alpha}$ and cyclooxygenase-2 during embryo implantation. Liquid chromatography-electrospray ionization tandem MS was used to validate MALDI IMS phospholipid distribution patterns. Overall, molecular images revealed the dynamic complexity of lipid distributions in early pregnancy, signifying the importance of complex interplay of lipid molecules in uterine biology and implantation.

B. Introduction

There is evidence that phospholipid metabolism and signaling influences early pregnancy events [91]. Phospholipids are vital structural and regulatory components of biological membranes and serve as precursors for many active biomolecules, such as eicosanoids and lysophospholipids [92, 93]. Prostaglandins (PG), one major group of eicosanoid lipid molecules, are produced from arachidonic acid (AA) that is released from membrane phospholipids by phospholipase A_2 (PLA_2). The released AA is acted upon by cyclooxygenases (COX) to form PGH which is then converted to various PGs by specific PG synthases [94]. Spatiotemporal expression profiles of cytosolic $PLA_{2\alpha}$ ($cPLA_{2\alpha}$), COX-1 and COX-2 in the uterus at different stages of pregnancy suggest their differential functions [95-98]. In mice, PGI_2 and PGE_2 generated by COX-2 are essential for ovulation, fertilization, implantation and decidualization [96, 97, 99-102]. PG's role is further illustrated by poor fertility, resulting from deferred implantation, in mice lacking $cPLA_{2\alpha}$ [95]. Another example for critical roles of lipid signaling in reproduction is the influence of lysophosphatidic acid (LPA), a small lipid molecule of the lysophospholipid family. LPA influences a variety of processes via its cell-surface G protein coupled receptors, LPA_{1-4} [103]. In mice, LPA_3 is expressed in the uterine luminal epithelium with peak expression occurring during the periimplantation period, and its expression overlaps with $cPLA_{2\alpha}$ and COX-2 at the site of implantation [104]. More importantly, mice missing LPA_3 show remarkably similar defects as $cPLA_{2\alpha}$-deficient mice, such as deferred on-time implantation, retarded fetal development, embryo crowding, and sharing of one placenta by several embryos [95, 104]. Restoration of on-time implantation in LPA_3-deficient females by PG supplementation suggests an intimate interaction between the LPA-LPA_3 and $cPLA_{2\alpha}$-COX-2-PG signaling pathways [104]. These findings established a new concept that a short delay in the attachment of blastocysts to the uterine lining during early pregnancy creates adverse ripple effects during the subsequent course of pregnancy, ultimately compromising pregnancy outcome [91, 105, 106]. There is also evidence that disturbances in sphingolipid metabolism by disruption of sphingosine kinase genes causes sphingoid base accumulation and a reduction of phosphatidylethanolamines, thereby inducing early pregnancy loss by compromising decidualization and the uterine vascular bed stability [107].

The goal of the present study was to utilize mass spectrometry technologies to assess globally the differential distribution of glycerophospholipids and sphingomyelins during the cellular events that define implantation. We speculate that spatial distribution of those phospholipids plays important roles in the implantation process. Matrix-Assisted Laser Desorption/Ionization Imaging Mass Spectrometry (MALDI IMS) generates ion density maps from tissue sections that allow protein and phospholipid localization to be visualized without prior knowledge of the specific molecules being analyzed [66, 67, 79, 81, 108-112]. This technology has been previously used to analyze proteins involved in proliferation, differentiation and apoptosis during early mouse pregnancy, providing unique and distinctive proteomic profiles of implantation sites [113]. In the present study, phospholipid distribution was visualized using the molecular imaging mode of both MALDI-TOF/TOF (TOF, Time-of-flight) and MALDI Fourier Transform Ion Cyclotron Resonance (FTICR) mass spectrometers. The fatty acid chain identities for each phospholipid were determined by tandem mass spectrometry (MS/MS) fragmentation. Isobaric phospholipid species with identical masses were visually distinguished using the MS/MS imaging mode of a MALDI linear ion trap (LTQ) mass spectrometer. Finally, absolute quantitation and identification of phospholipids on day 8 of pregnancy was determined using liquid chromatography-electrospray ionization tandem MS (LC-ESI-MS/MS) with odd carbon internal standard in order to further validate phospholipid distribution patterns obtained from the MALDI MS images.

C. Results

C.i. Spatial remodeling of phospholipids during early pregnancy. The molecular images obtained in this study show that phospholipid distributions correlate with the heterogeneous cell types (indicated in **Figure 8**) that arise during the course of implantation. Zwitterionic phosphatidylcholines (PCs) and sphingomyelins (SMs) are readily detected in the positive mode (**Figure 9**) by MALDI MS; whereas, the anionic phosphatidylinositols (PIs), phosphatidylserines (PSs), and phosphatidylglycerols (PGs) are best detected in the negative mode (**Figure 10**). Phosphatidylethanolamines (PEs) and phosphatidylethanolamine plasmalogens (PEps) can be detected as positive or negative ions, but are usually best measured in negative mode directly from tissue sections.

Images of specific phospholipids taken during day 4-8 are shown in columns in **Figures 9 and 10**. At the top of each column phospholipids are labeled using accepted lipid nomenclature where the first number represents the total number of carbon atoms in the two fatty acid chains, and the second number represents the total number of double bonds in the two fatty acid chains. The identity of each individual fatty acid side chain is located in parenthesis (sn1/sn2). Fatty acid chains were identified from a combination of the exact mass of the phospholipid molecular species and the MS/MS fragmentation pattern (described below).

From these data, phospholipid expression patterns can be categorized according to the degree of unsaturation of the sn2 fatty acid chain. Consequently, the images displayed in **Figures 9 and 10** are aligned in increasing order of unsaturation; 16:0, 18:0, 18:1, 18:2, 20:4, 22:4, and 22:6. Although there remains some uncertainty in the sn1 and sn2 positional assignment of fatty acids from mass spectral data, it is generally accepted that the more unsaturated fatty acids occupy the sn2 position. **Table 1** and **Table 2** list fragment peaks from highest intensity to lowest intensity [67, 114].

The molecular images shown in **Figures 9 and 10** depict alterations in phospholipid distributions as uterine cells undergo decidual changes from day 4 to day 8 of pregnancy. Before embryo attachment, luminal epithelial cells show substantial increases for SM 16:0 and PCs with 18:1, 18:2 and 20:4 as their unsaturated fatty acid chain (**Figure 9**). Conversely, PC (16:0/16:0) shows relatively higher expression in all cell types except for the luminal epithelial cells.

Overall, this saturated phospholipid shows an inverse localization pattern when compared to the other phospholipids on days 4-8 of pregnancy. On day 5 of pregnancy, glycerophospholipid images show an intensity increase in uterine stroma cells at the site of embryo attachment, whereas on day 6, glycerophospholipid expression is most intense in the PDZ. Also, certain phospholipids show higher levels in the M pole (above the embryo in these images) and AM pole (around the bottom of the embryo). Higher expression in the M pole is seen for all PC (16:0/18:1), PE (16:0/18:1), and PI (18:1/20:4), whereas higher expression at the AM pole can be seen for PC (18:0/18:2) and PI (16:0/18:2). On day 8 of pregnancy many of the phospholipids show higher intensity either in the M pole or AM pole. Overall, the phospholipids that show higher levels at the M pole are: PCs, PE, PG and PS containing 18:1; PIs and PE with 20:4 as their polyunsaturated fatty acid; and PEp (16:0/22:4). The phospholipids showing higher intensities at the AM pole are: PCs, PIs, and PS having 18:2 as a substituent; PCs with 20:4 as their polyunsaturated fatty acid; PC, PEp, and PI with 22:6 as their polyunsaturated fatty acid. The reproducibility of these results is represented in **Figures 11, 12 and 13**, and the quality of the primary Maldi Spectra is represented in **Figure 14** (positive ion mode) and **Figure 15** (negative ion mode). Subsequent experiments were focused on the day 8 implantation sites, because the most dramatic spatial changes in phospholipid expression were observed. Day 8 implantation sites also contain major cellular alterations including angiogenesis, apoptosis and proliferation.

C.ii. **Determining the presence of isobaric ions (same nominal mass but different exact masses) in day 8 implantation sites by FTICR IMS.** The molecular weights of phospholipids investigated in this study are between 600 and 1000 Da. Within this mass range, the peak density of MALDI spectra are typically complicated by a large number of other endogenous metabolites as well as matrix ions. Together with the naturally occurring carbon isotopes of these species, the resolving power of TOF instruments may not be capable of determining if multiple isobaric ions are contributing to a specific ion image. Positive ion spectra, in particular, can be quite complex with the possibility of detecting ions adducted with H^+, Na^+ or K^+. To determine isobaric interference, MALDI images of Day 8 embryos were also acquired on a FTICR at a resolving power of 100,000 (FWHM). Peak widths were 10-20 mDa, compared to 100-200 mDa for the TOF spectra, and are sufficient to resolve most phospholipid species that are typically observed in MALDI spectra. Ion images from both instruments are shown in **Figure 9 and 10** and from these data it is clear that only one molecular species contributes to the TOF images.

An example where multiple isobaric ions were detected is shown in **Figure 16**. **Figure 16** illustrates MALDI-TOF images (top) and corresponding MALDI-FTICR (bottom). The first 2 columns and last 2 columns represent the potassiated (K^+) and sodiated (Na^+) forms of PC 34:1 (16:0/18:1) and PC 34:2 (16:0/18:2), respectively. The TOF images of the potassiated form of each phospholipid species do not contain any interfering ions. Conversely, the TOF images of the sodiated form of each phospholipid species represent multiple ions. The TOF image of PC 34:1 Na^+ contains an unknown interfering peak at 782.509 *m/z*. The TOF image of PC 34:2 Na^+ contains 3 unknown interfering peaks with *m/z* values 758.508, 758.545, and 758.525. The FTICR images of PC 34:2 Na^+ illustrates the strength of this technology, by its ability to spatially resolve 4 different ions within a mass window of only 0.06 Daltons.

C.iii. ***In situ* identification of phospholipids by tandem MS.** Identification of fatty acid chains in the phospholipids was accomplished using both the accurate mass of the parent phospholipid ion with FTICR IMS (mass accuracy of +/- 0.005 Da at *m/z* 1,000 [5 ppm]) and MS/MS fragmentation spectra [115]. **Table 1 and 2** contain the accurate mass and fragmentation peaks for each lipid in positive and negative ion mode, respectively. The structures and fragmentation spectra of PI (18:0/18:2) and PC (18:0/18:2) are shown in **Figure 17**.

C.iv. **Distinguishing spatial distribution of isobaric phospholipids (identical masses) in day 8 implantation sites by tandem IMS.** The MS images for phospholipids PE 36:2 and PE 38:2 showed no distinct spatial location (**Fig 18, *left***). However, MS/MS fragmentation found each of these phospholipid ions to consist of multiple isobaric species (structure of each isobar **Fig 18, *middle***). PE 18:0/18:2 and PE 18:1/18:1 are isobars of the class PE 36:2 (*m/z* = 742.54). PE 20:0/18:2, PE 18:0/20:2, and PE 18:1/20:1 are isobars of PE 38:2 (*m/z* = 770.57). Tandem MS imaging determined the spatial location of each isobar in day 8 implantation sites (**Fig 18, *right***). The MS/MS images of PE 36:2 and PE 38:2

confirmed that more than one combination of sn1 and sn2 fatty acids were present. Although MS/MS images were obtained for each fragment ion, **Figure 18** displays only the most intense fragment ion from each isobar (represented by a red arrow on each phospholipid structure). The MS/MS images of PE 36:2 contain 18:2 (signified by the fatty acid 18:2 or the 279 *m/*z fragment ion) that localized to the bottom (AM pole) and 18:1 (281 *m/*z fragment ion) that localized to the top (M pole) of the day 8 implantation site. The MS image of PE 38:2 includes PE (20:0/18:2), PE (18:0/20:2), and PE (18:1/20:1). The MS/MS images of PE 38:2 contain either the diunsaturated 18:2 fatty acid (279 *m/*z fragment ion) or 18:0 fatty acid (283 *m/*z fragment ion) that both localize to the AM pole or the monounsaturated fatty acid 18:1 (281 *m/*z fragment ion) that localizes to the M pole of the day 8 implantation site.

C.v. **Validation of MALDI IMS phospholipid expression patterns by liquid chromatography-electrospray ionization tandem MS (LC-ESI-MS/MS) quantitation.** LC-MS/MS was used to quantify and identify phospholipids in the M and AM poles on day 8 of pregnancy (**Figure 19a-c**). Approximately 15 mg of tissue was needed for this analysis; thus, day 8 implantation sites were micro-dissected (**Figure 19a**) to isolate the top and bottom hemispheres for subsequent organic phase lipid extraction. The bottom row of **Figure 19c** contains selected FTICR phospholipid images that exhibit the greatest change in relative abundance between the M and AM poles in day 8 implantation sites. LC-MS/MS quantitation of these same phospholipids is illustrated as block structures, set to the same linear black and white scale as the MALDI images, in the top row of **Figure 19c** or as bar graphs in **Figure 19b**. In summary, LC-MS/MS quantitation and MALDI IMS showed excellent agreement, with PC 34:1 (16:0/18:1), PE 34:1 (16:0/18:1), and PI 38:5 (18:1/20:4) localizing to the M pole and PC 34:2 (16:0/18:2), PI 34:2 (16:0/18:2), PC 36:4 (16:0/20:4), PC 40:6 (18:0/22:6) and PI 40:6 (18:0/22:6) localizing to the AM pole. **Table 3** contains all of the statistically significant LC-MS/MS results.

C.vi. **Colocalization of arachidonate-containing phospholipids with cyclooxygenase-2 (COX-2).** Signaling of prostaglandin signaling, resulting from cPLA$_{2\alpha}$-COX-2 processing of arachidonate (20:4), participates in embryo attachment and uterine decidualization during embryo implantation [95, 97]. Thus, it was of interest to determine which arachidonate-containing phospholipids colocalize with COX-2. **Figure 20** shows an immunohistochemistry (IHC) stain for COX-2 and the MALDI images of arachidonic acid containing phospholipids. COX-2 expression localizes to the M pole above the EPC, correspondingly PIs and PEs show M pole expression with PE 38:5 (18:1/20:4) and PI 38:5 (18:1/20:4) exhibiting highest levels of expression above the EPC. In contrast, PC 36:4 (16:0/20:4) and PC 38:4 (18:0/20:4) expression patterns are confined to the AM pole.

D. Discussion

Lipids are important components of cellular membranes and also serve as signaling molecules that help coordinate events during embryo implantation and postimplantation growth [97, 104]. In the present study, we have mapped phospholipid distributions during embryo implantation employing the molecular specificity of mass spectrometry. The results demonstrate that distribution of phospholipids is markedly altered during implantation with changes specific to the M (top) and AM (bottom) poles of the uterus, suggesting roles for those phospholipids in the implantation process.

The distribution of phospholipids showed significant changes in day 5 implantation sites after embryo attachment, and most phospholipids showed substantial increases in the stroma immediately surrounding the implanting embryo. The spatial redistribution continued on days 6-8 of pregnancy with differential localization in the M and AM poles of the implantation sites. With respect to proteins, previous reports on day 8 of pregnancy revealed an increased level of proteins involved in angiogenesis at the M pole and those involved in cell death at the AM pole. Specifically, pro-angiogenic proteins angiopoietins 2 (Ang2) and Ang3 and their endothelial-specific receptor tyrosine kinase Tie2 show an increased expression at the M pole, which also expresses COX-2, a known enhancer of angiogenesis [2]. Although the mechanism(s) governing decidual cell death at the AM pole are not clearly understood, there is evidence that a balance between proapoptotic Bax and antiapoptotic Bcl are involved [116]. Regardless, these differential behaviors of the M and AM poles have biological significance with respect to increasing angiogenesis at the M pole, the site of angiogenesis, and initiating apoptosis or cell death at the AM pole to make room for the rapidly growing embryo. This molecular orchestration of lipids and proteins in both space and time underscores the complex biological processes involved in sustaining embryo growth and survival during early pregnancy.

For lipids, these data show a segregation of phospholipids that contain linoleate (18:2) and docosahexaenoate (22:6) at the AM pole, and oleate (18:1) at the M pole, across all lipid classes. Arachidonate (20:4) containing phospholipids showed differential segregation patterns depending on the lipid class. This is interesting in the context of the reported finding that liberation of arachidonate by $cPLA_{2\alpha}$ from membrane phospholipids is class-dependent [117, 118]. This may explain why different classes of arachidonic acid containing membrane phospholipids show differential expression patterns in our molecular images. There is now evidence that COX-2 expressed on day 8 of pregnancy at the M pole above the EPC plays a role in angiogenesis [97] (**Figure 20**). Phospholipids that act as substrates in the $cPLA_{2\alpha}$-COX-2 pathway should co-localize with the rate limiting enzyme COX-2. In fact, while arachidonate containing PEs and PIs are localized to the M pole, arachidonate containing PCs are found to be localized to the AM pole.

The present study reveals the importance of obtaining detailed molecular information on both a spatial and temporal basis to uncover the complexity of biological events. We believe this paper will initiate further studies which will help us to better understand the intricacies of implantation and how specific lipid species may mediate, balance, and control cellular events.

E. Materials and Methods

Mice. Adult CD-1 mice were purchased from Charles River Laboratory (Raleigh, NC). Females were mated with fertile males of the same strain to induce pregnancy. Mice were sacrificed between 0900 and 1000 h on the specified day of pregnancy (0 h on day 1 = vaginal plug). Implantation sites on days 5 and 6 of pregnancy were visualized by an intravenous injection of Chicago Blue dye solution, as previously described [87]. With the blue dye method, implantation and interimplantation sites can be separately excised, and sections with the implanting embryo can be analyzed. On day 8 of pregnancy, blue dye injection is not necessary, since implantation sites are visually distinguishable. All mice in the present investigation were treated in accordance with the National Institutes of Health and institutional guidelines on the care and use of laboratory animals.

MALDI-MS Data. Implantation and interimplantation sites were dissected from the uterus, snap-frozen, sectioned (11 µm) in a cryostat and thaw-mounted onto MALDI MS compatible glass slides. Tissues analyzed include pre-implantation uterine sections (Day 4 of pregnancy) and implantation site sections (Day 5, Day 6, Day 7 and Day 8). MALDI-TOF Images were acquired on an Ultraflex (Bruker Daltonics, Billerica, MA) Mass Spectrometer. MALDI-FTICR Images were acquired on a 9.4 T Apex III (Bruker Daltonics, Billerica, MA) Mass Spectrometer. The lateral resolution of images depicted in **Figures 9 and 10** was 100 µm (positive ion mode images) and 150 µm (negative ion mode images) for the MALDI-TOF data and 250 µm (positive mode images) and 150 µm (negative mode images) for the MALDI-FTICR data. For positive mode figures, the most intense $[M+K]^+$ form of each phospholipid species is depicted, although each type of adduct ($[M+H]^+$, $[M+Na]^+$ and $[M+K]^+$) showed the same localization pattern. Matrix application in positive and negative mode utilized dry-coating methods [7] to deposit 2,5-dihydroxybenzoic acid (DHB) and ultra fine nebulization to deposit 2,5-dihydroxyacetophenone (DHA) (9 mg DHA, 6 µl aniline, 700 µl ethanol, 300 µl DI water) on tissue sections, respectively.

MALDI-MS/MS Data. The Day 8 images, located in the bottom of **Figure 9 and 10,** were acquired on a 9.4 Tesla FTICR mass spectrometer with a mass accuracy of +/- 0.005 Da at *m/z* of 1,000 (5 ppm). The LIPID metabolites and pathways strategy (LIPID MAPS) online resource was used to search for possible lipid structures that could match our experimental mass (+/- 0.005 Da). Although only one theoretical mass matched in each case, multiple fatty acid isobars with the same exact mass are possible. Thus, MS/MS fragmentation of phospholipids was implemented to confidently determine the fatty acid chains. Fragmentation of PIs, PSs and PEs in negative ion mode generates fatty acid peaks and corresponding lysospecies [115]. Characteristic fragmentations of PCs in positive ion mode contain only one fragment corresponding to the head group (*m/z* 184 Da). To obtain more fragment peaks for PCs, the matrix was doped with lithium chloride [67, 119]. Fragmentation peaks for each lipid in positive ion mode and negative ion mode are listed in **Table 1 and 2**, respectively. **Figure 17** contains MS/MS spectra.

All MS/MS experiments were performed on a MALDI-Linear Ion Trap Quadrupole mass spectrometer (MALDI-LTQ, Thermo Electron Corporation, San Jose, CA). For fragmentation of phospholipids, matrix was hand spotted; DHA was used for negative mode analysis and DHA with 100 mM LiCl was used for positive mode fragmentation. In MS/MS imaging experiments, tissue sections were spotted at a lateral resolution of 230µm (Portrait 630 reagent Multi-Spotter, Labcyte, Sunnyvale, CA)

LC-MS/MS Data. All LC-MS/MS experiments were performed on a hybrid triple quadrupole/ linear ion trap mass spectrometer (4000 QTrap, Applied Biosystems, Foster City, CA). Each experiment required approximately 15 mg of tissue. LC-MS quantitation of phospholipids followed previously published protocols [76]. Specifically, we use 4 odd carbon internal standards per lipid class (25:0 [low mass] to 43:6 PUFA [high mass]). We produce standard curves using multiple naturally occurring even carbon standard for each class (tied to the intensity of the internal standards). Identification of individual phospholipids was achieved by LC-MS/MS fragmentation analysis. **Table 3** contains the results for some of the phospholipids analyzed (3 replicate experiments for the analysis of top and bottom hemispheres of day8 implantation sites [top1, top2, topM / bot1, bot2, botM]).

Immunohistochemistry. The COX-2 antibody was purchased from Cayman (Ann Arbor, MI) [98]. Localization of protein in formalin-fixed paraffin-embedded uterine sections (5 μm) was achieved as previously described [120]. In brief, after deparaffinization and hydration, sections were subjected to antigen retrieval using a pressure cooker in 10 mmol/L sodium citrate solution (pH 6.0) for 20 minutes. A Histostain-Plus kit (Zymed, San Francisco, CA) was used to visualize the antigen; brown deposits indicate sites of positive immunostaining.

F. Acknowledgments

Mice were supplied by Sudhansu K. Dey's Lab. Sections were provided by Susanne Tranguch (Sudhansu K. Dey's Lab). LC-ESI-MS/MS experiments were done in collaboration with H. Alex Brown's Lab (Stephen B. Milne and David S. Myers). COX-2 IHC staining experiments were done in collaboration with Haibin Wang (Sudhansu K. Dey's Lab).

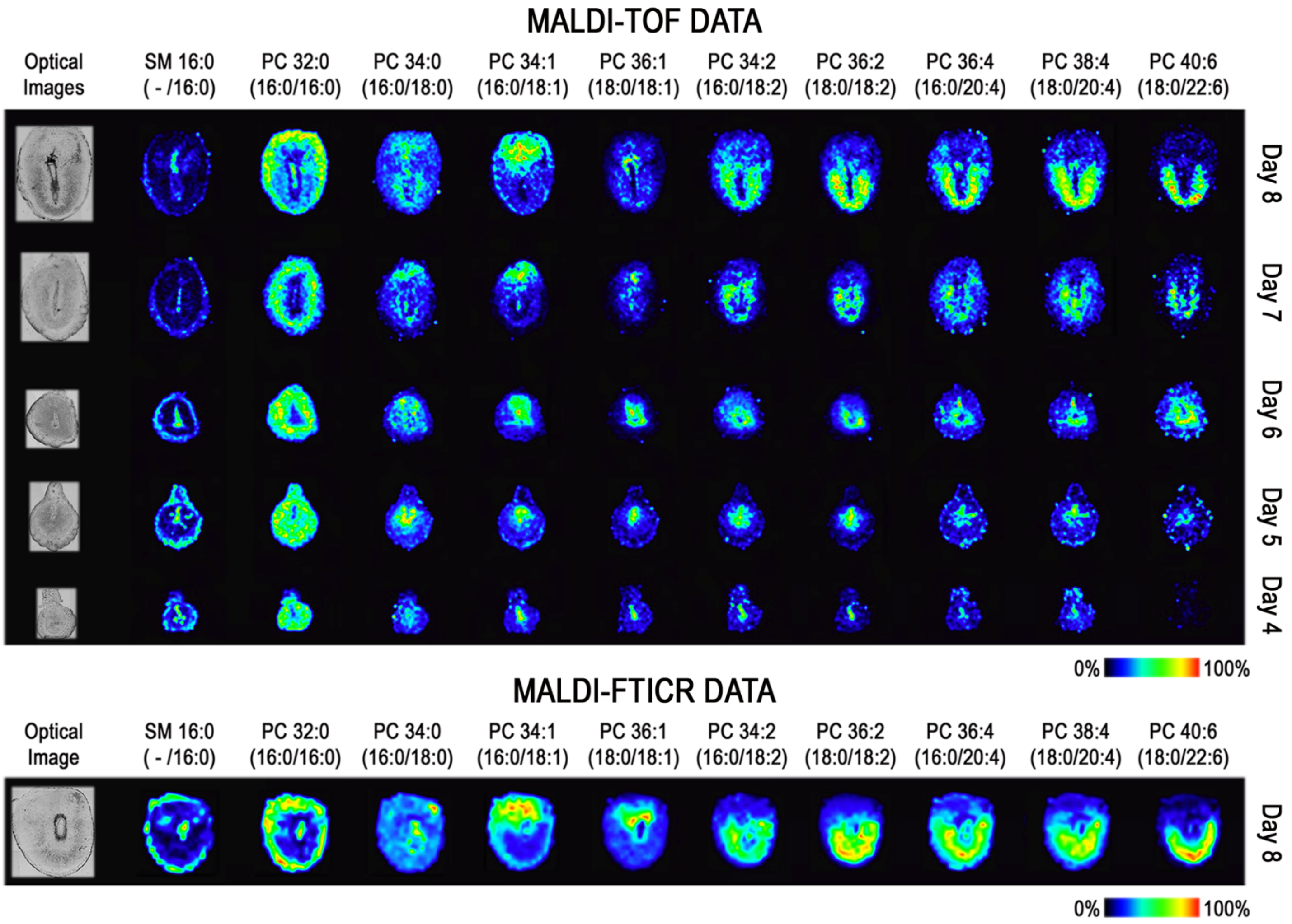

Figure 9. Molecular images of sphingomyelin (SM) and phosphatidylcholine (PC) phospholipids on days 4 to 8 of implantation. MALDI-TOF images (top) and MALDI-FTICR images (bottom) of implantation sites are located to the right of their respective optical images. Each column represents a unique potassiated phospholipid [M+K]+ and each row represents a different day of pregnancy.

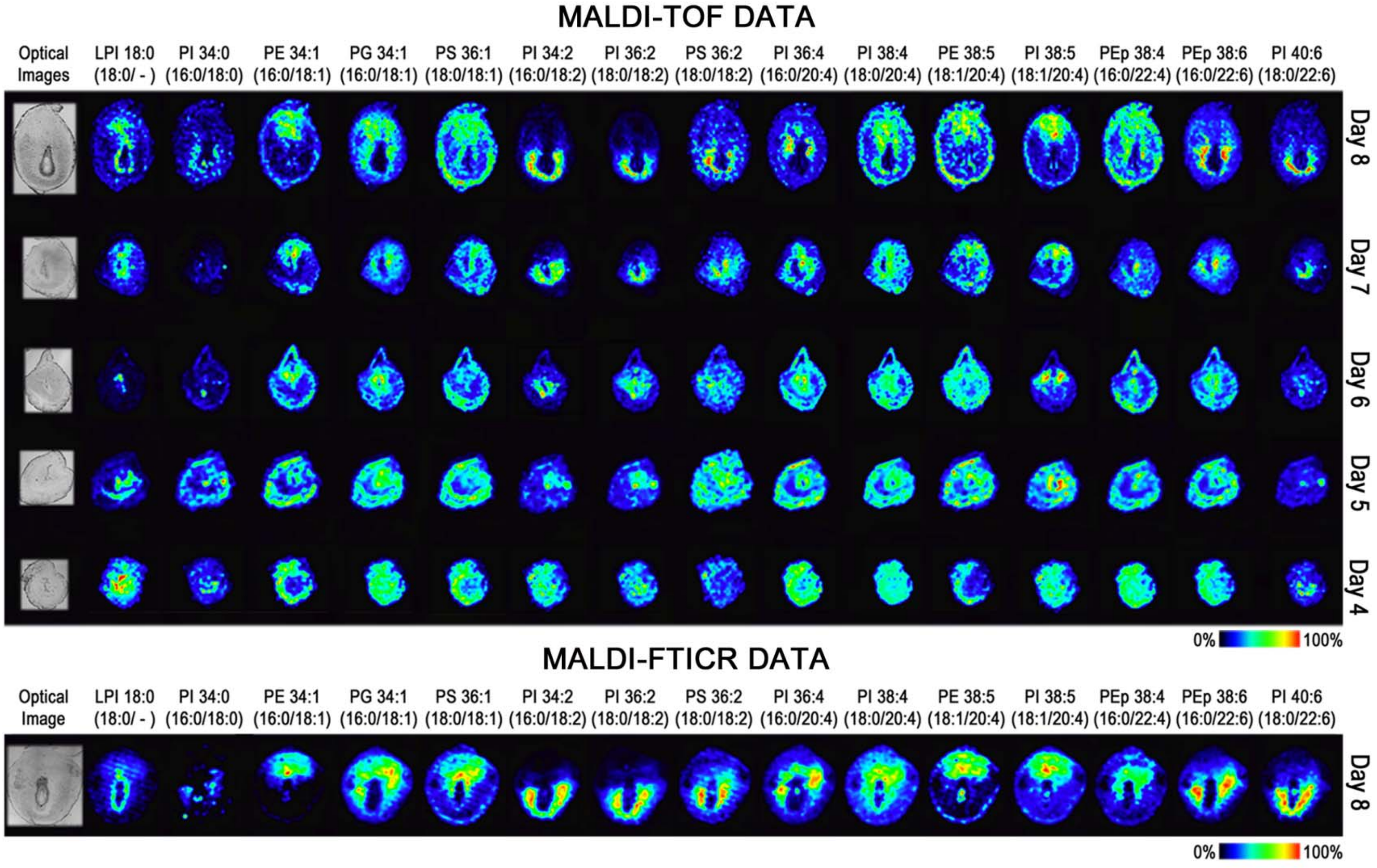

Figure 10. Molecular images of phosphatidylethanolamine (PE), phosphatidylethanolamine plasmalogen (PEp), phosphatidylinositol(PI), lysophosphatidylinositol (LPI), phosphatidylserine (PS) and phosphatidylglycerol (PG) on days 4 to 8 of implantation. MALDI-TOF images (top) and MALDI-FTICR images (bottom) of implantation sites are located to the right of their respective optical images. Each column represents a unique phospholipid [M-H]- and each row represents a different day of pregnancy.

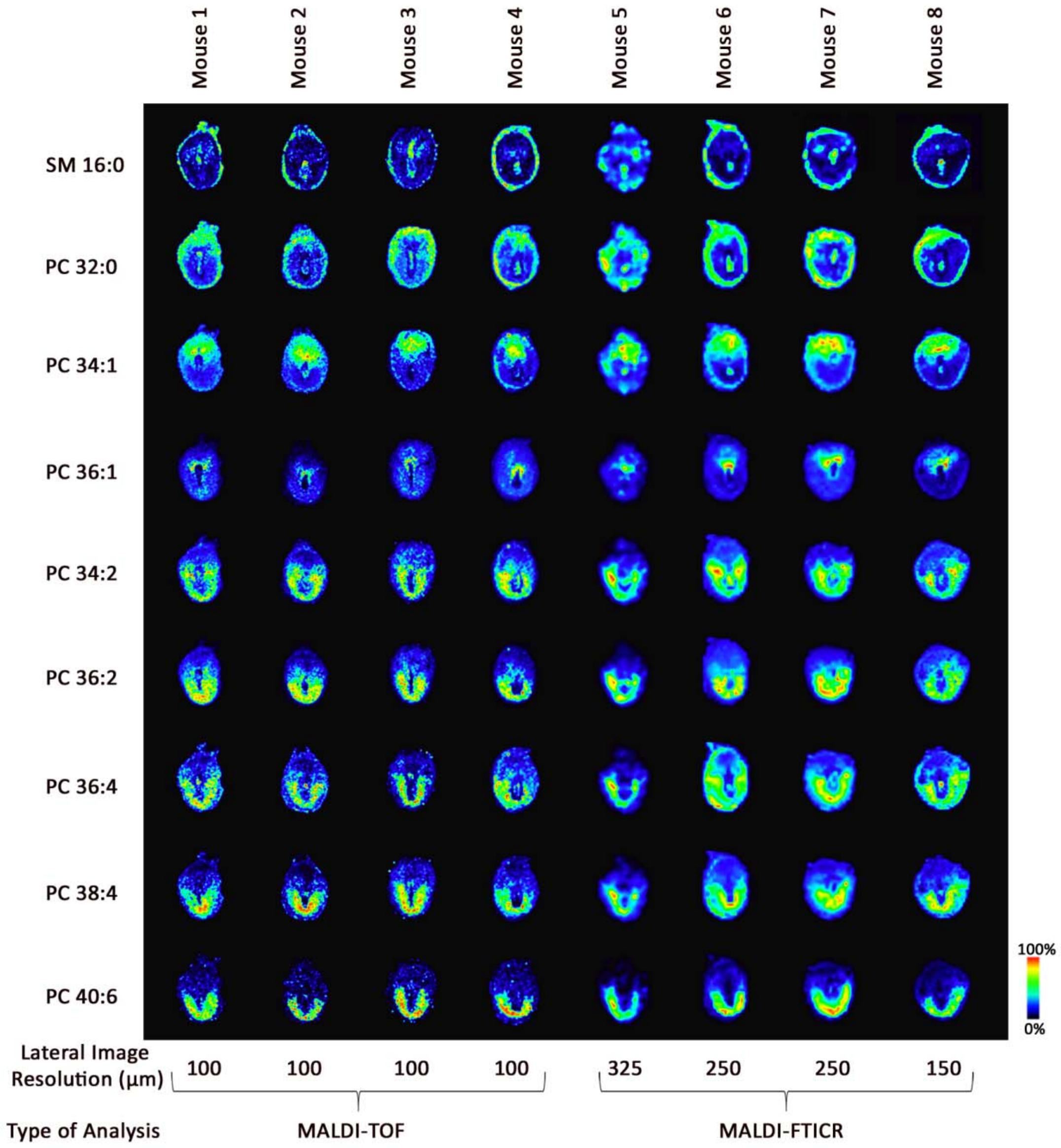

Figure 11. Reproducibility of Positive Ion Mode (MALDI-TOF & MALDI-FITCR) Phospholipid Imaging Data. Each column represents a different day 8 implantation site each from a different mouse. Each row represents a unique potassiated phospholipid ([M+K]+) and how it localizes in each of the 8 different implantation sites.

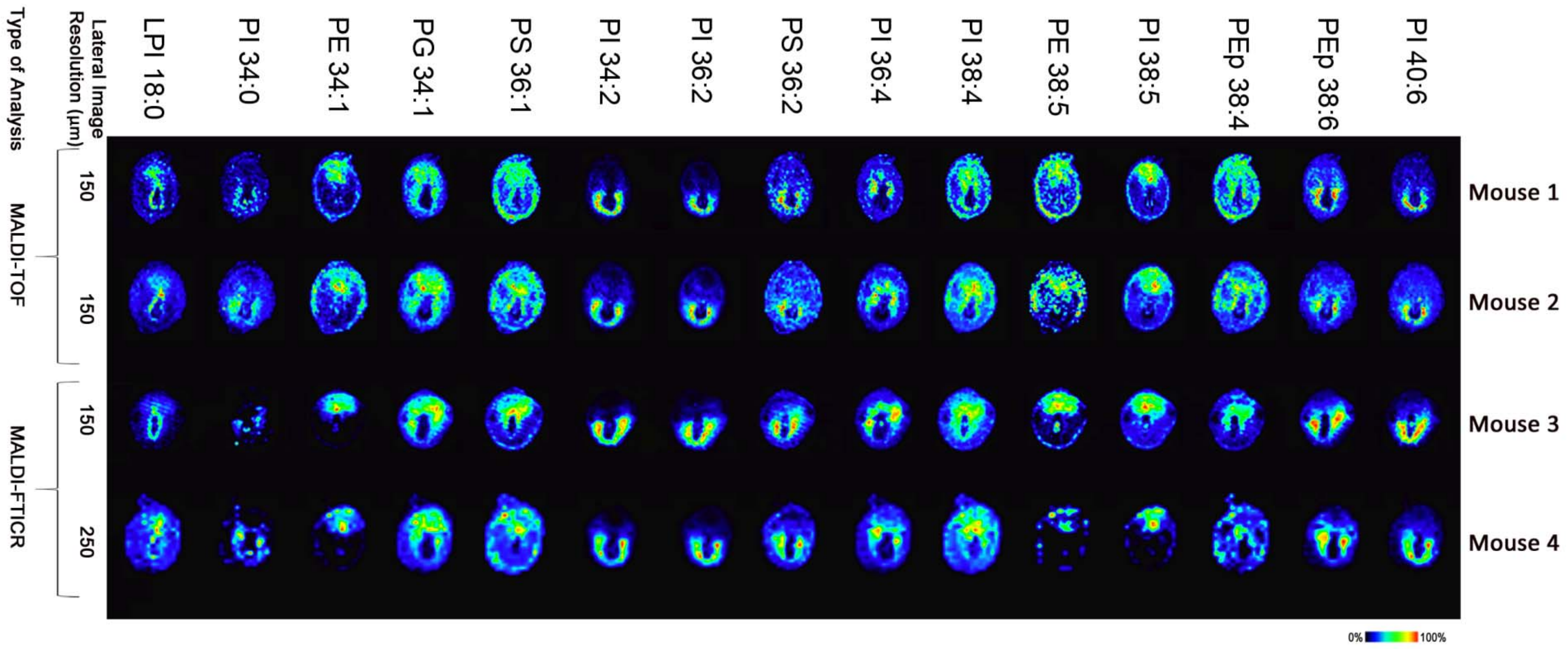

Figure 12. Reproducibility of Negative Ion Mode (MALDI-TOF & MALDI-FITCR) Phospholipid Imaging Data. Each row represents a different day 8 implantation site each from a different mouse. Each column represents a unique phospholipid ([M-H]-) and how it localizes in each of the 4 different implantation sites.

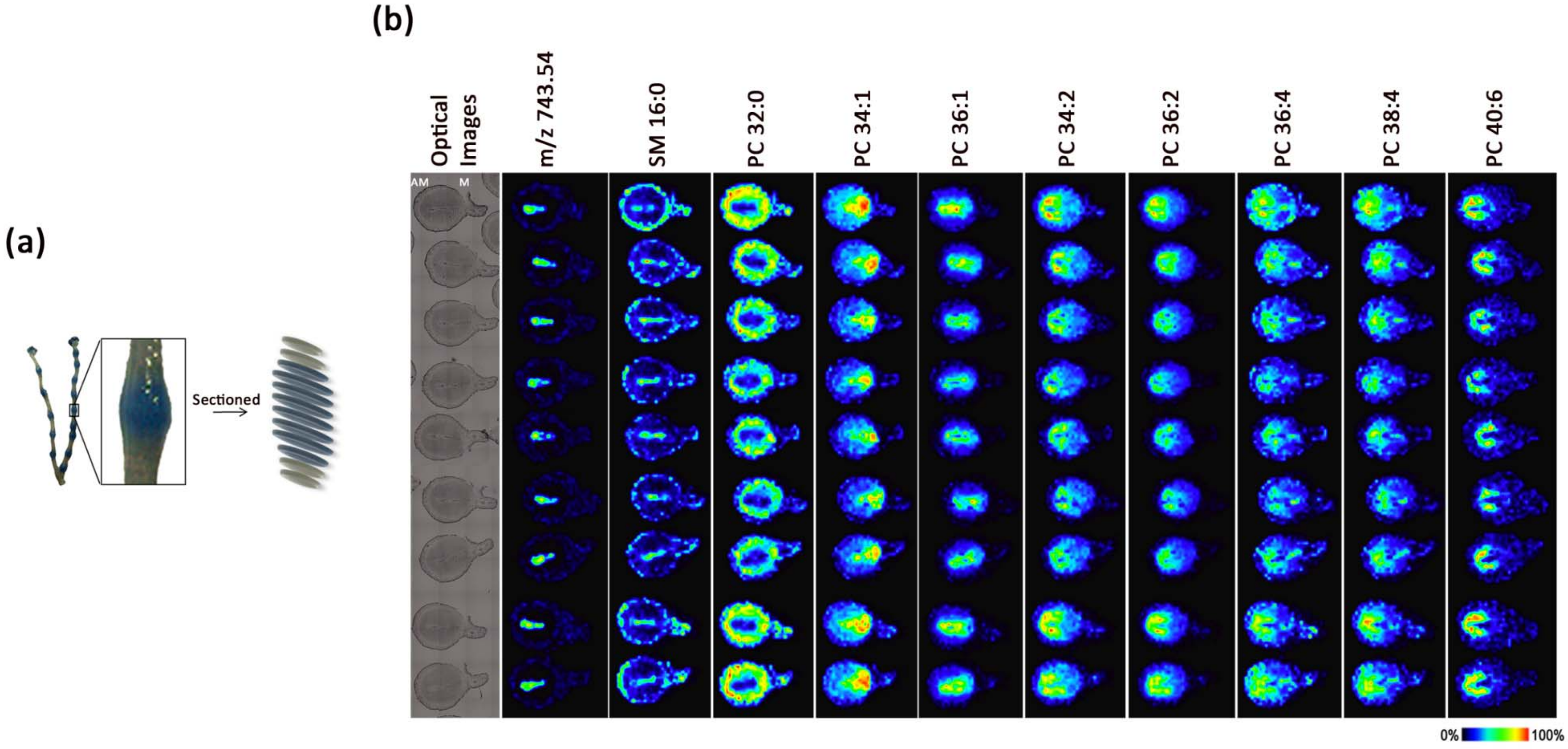

Figure 13. Reproducibility of MALDI-FTICR IMS analysis of embryo implantation in the mouse uterus on day 6 of pregnancy. (a) This picture shows a mouse uterus on day 6 of pregnancy and an enlargement of the implantation site which was sectioned. **(b)** The optical images of the 9 serial center sections (left) with corresponding 150 µm lateral resolution MALDI-FTICR images (right). Phospholipid identities ([M+K]+) are listed above their respective columns. Each column is set to the same relative intensity scale.

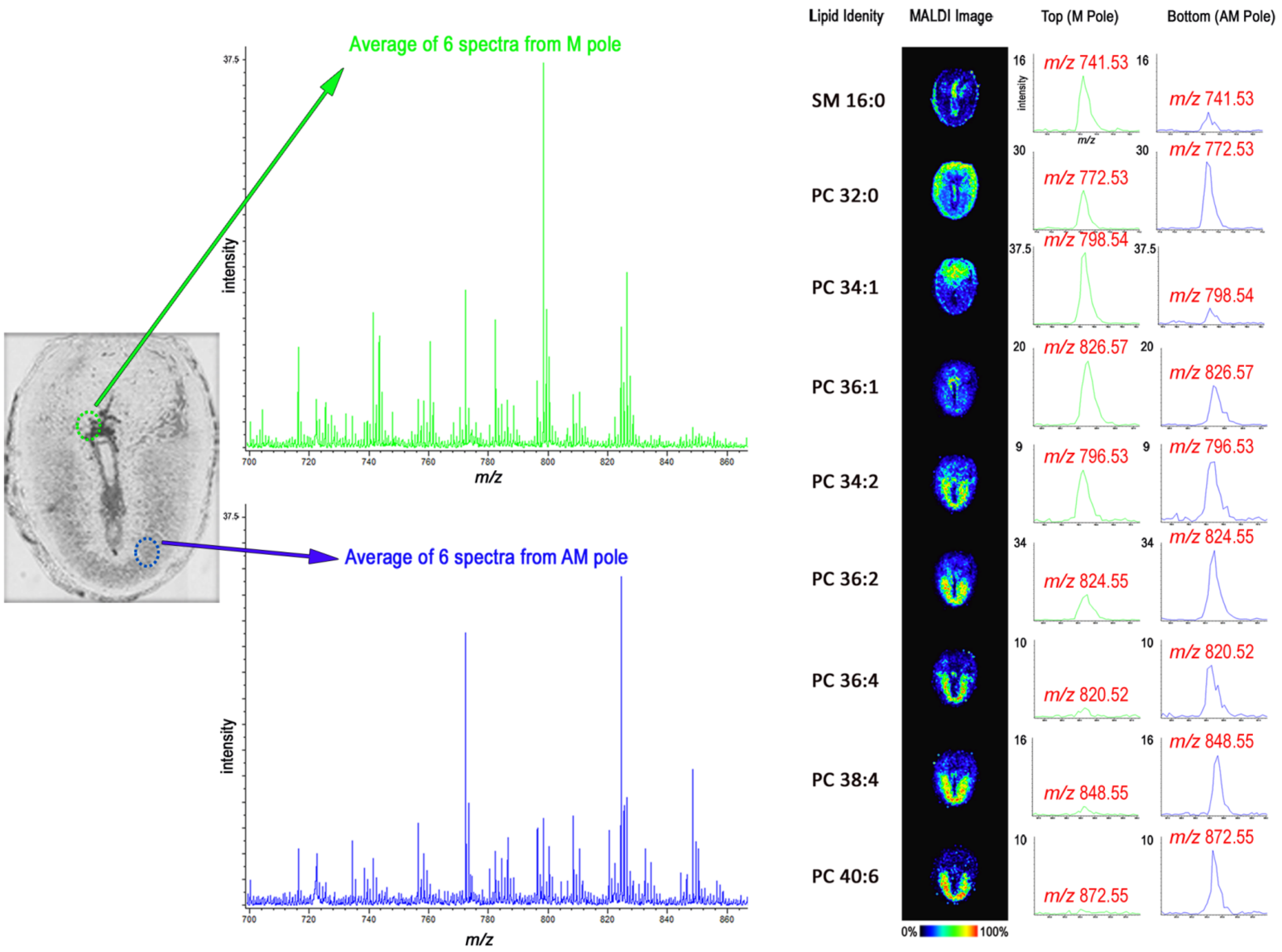

Figure 14. A Look at Positive Ion Mode MALDI-TOF Image Spectra. All spectra is from representative “top” and “bottom” areas of a day 8 implantation site which are depicted as a green and blue circles on the optical image, respectively.

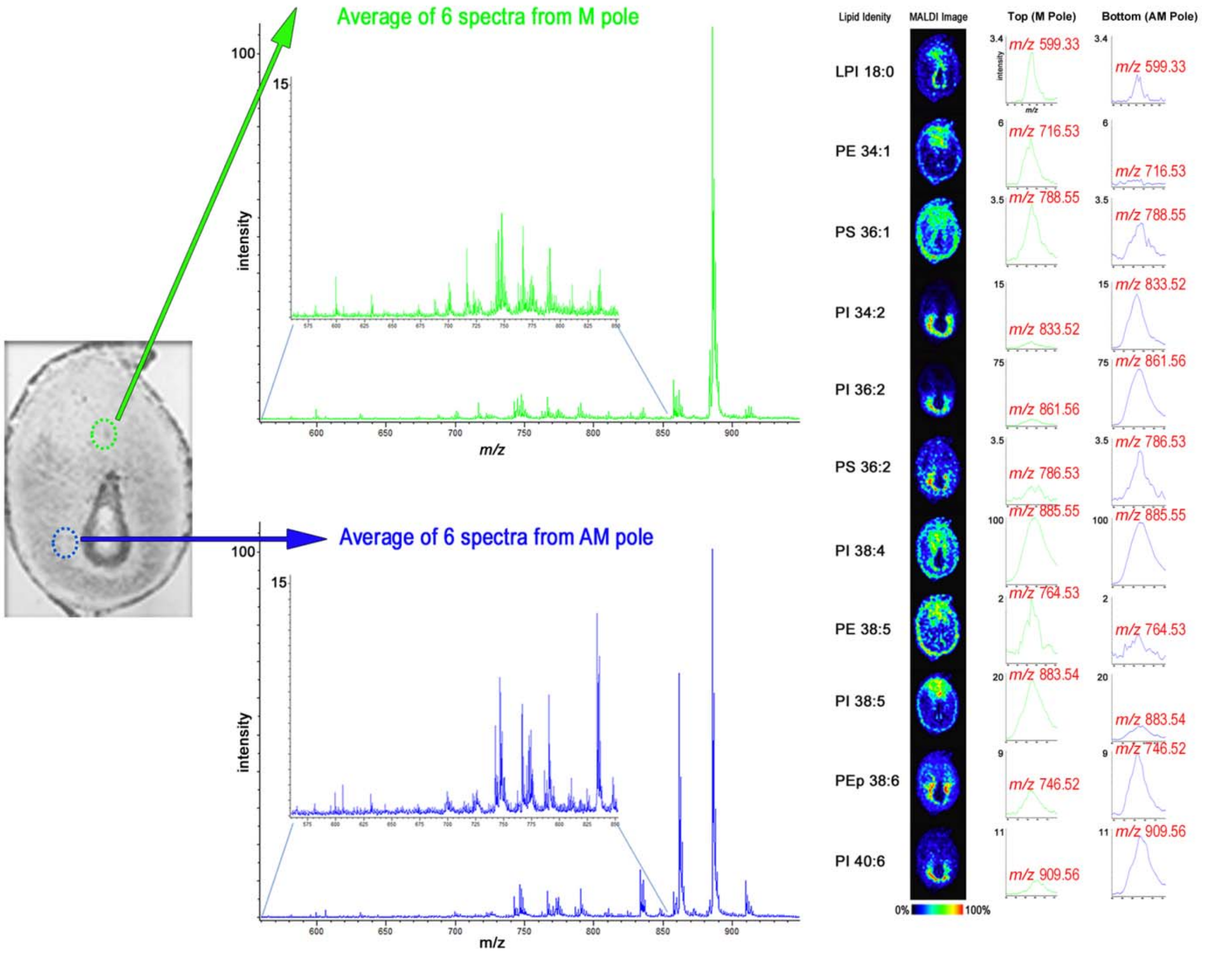

Figure 15. A Look at Negative Ion Mode MALDI-TOF Image Spectra. All spectra is from representative “top” and “bottom” areas of a day 8 implantation site which are depicted as a green and blue circles on the optical image, respectively.

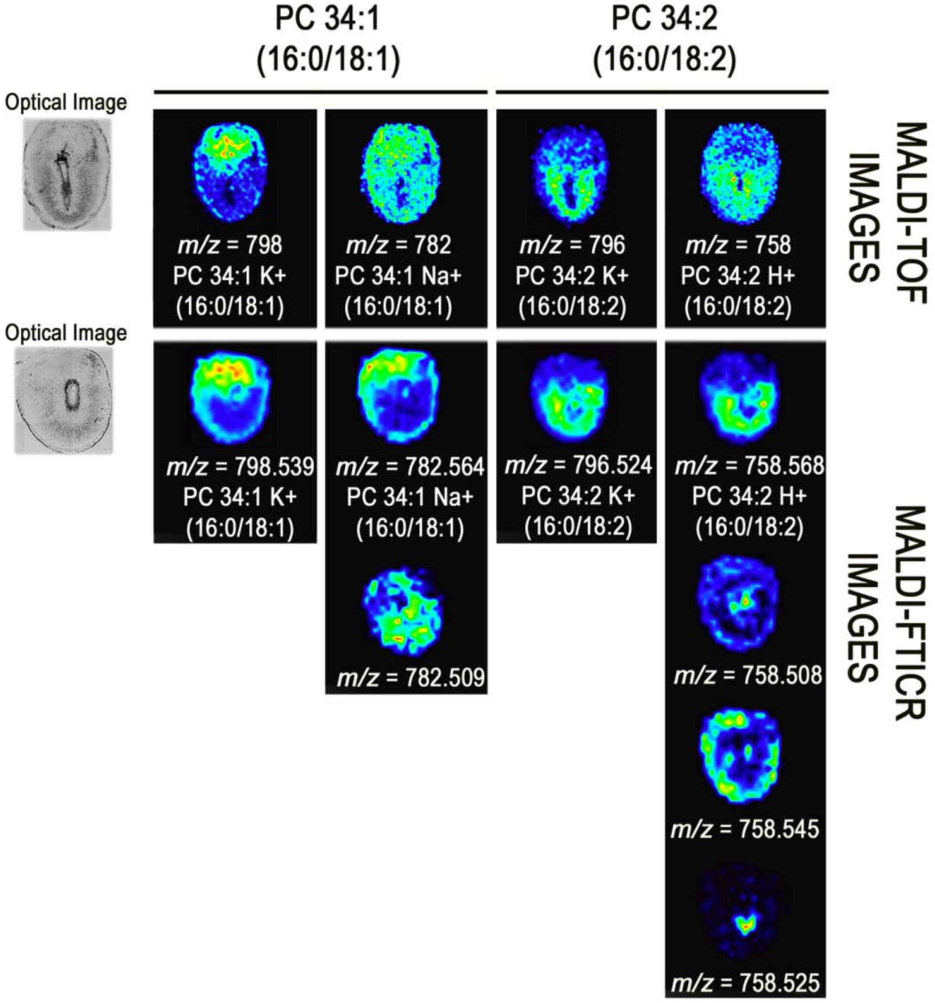

Figure 16. Identification of isobaric phospholipid species in day 8 implantation sites using high resolution MALDI-FTICR imaging MS. MALDI-TOF images (top) representative of spectral peaks 100-200 mDa in width. MALDI-FTICR images (below) representative of spectral peaks 10-20 mDa in width. Abbreviation: PC, phosphatidylcholine.

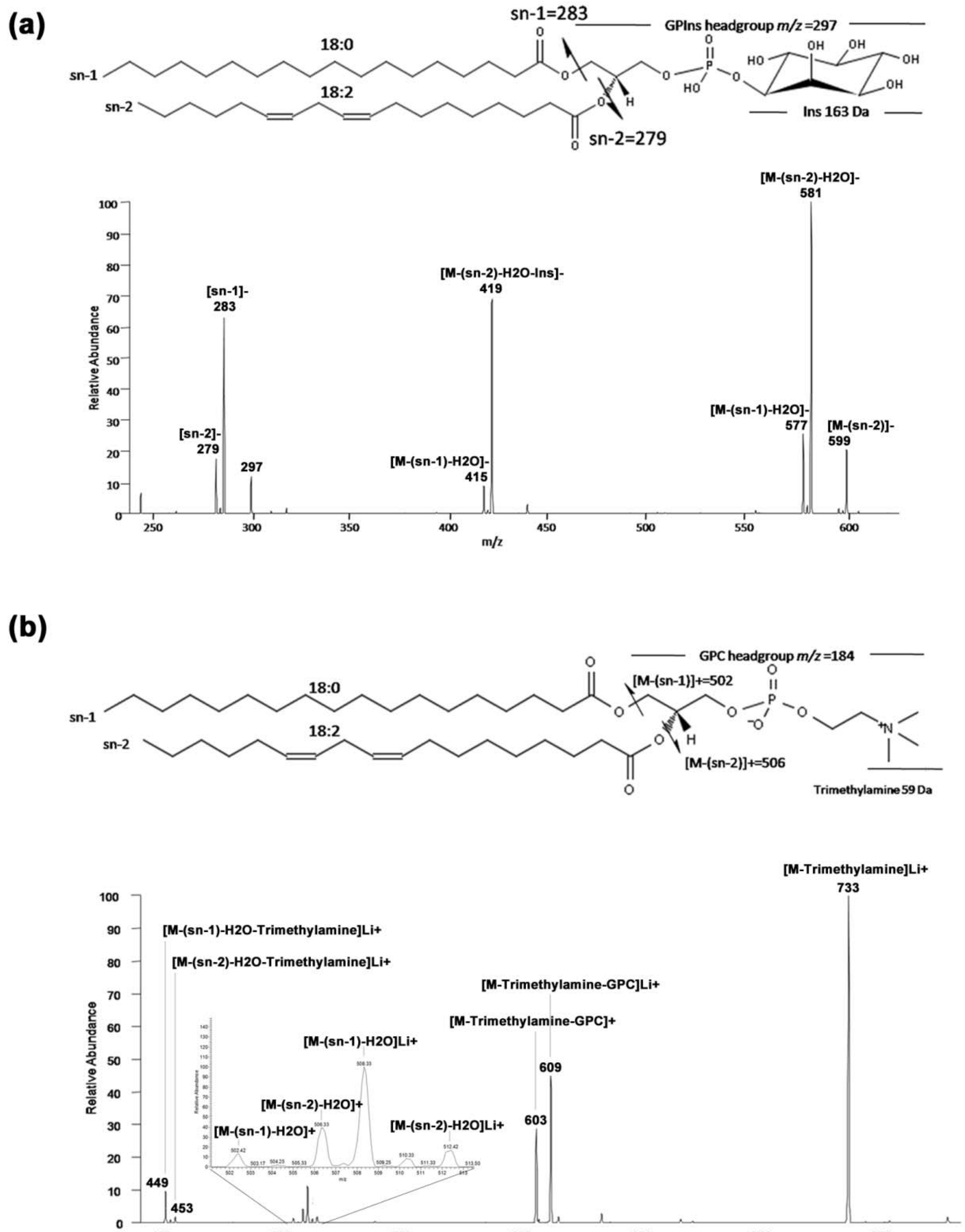

Figure 17. MS/MS spectra. (a) Fragmentation spectra of PI 36:2 in negative ion mode. **(b)** Fragmentation spectra of PC 36:2 in positive ion mode [matrix was doped with 100 mM lithium chloride].

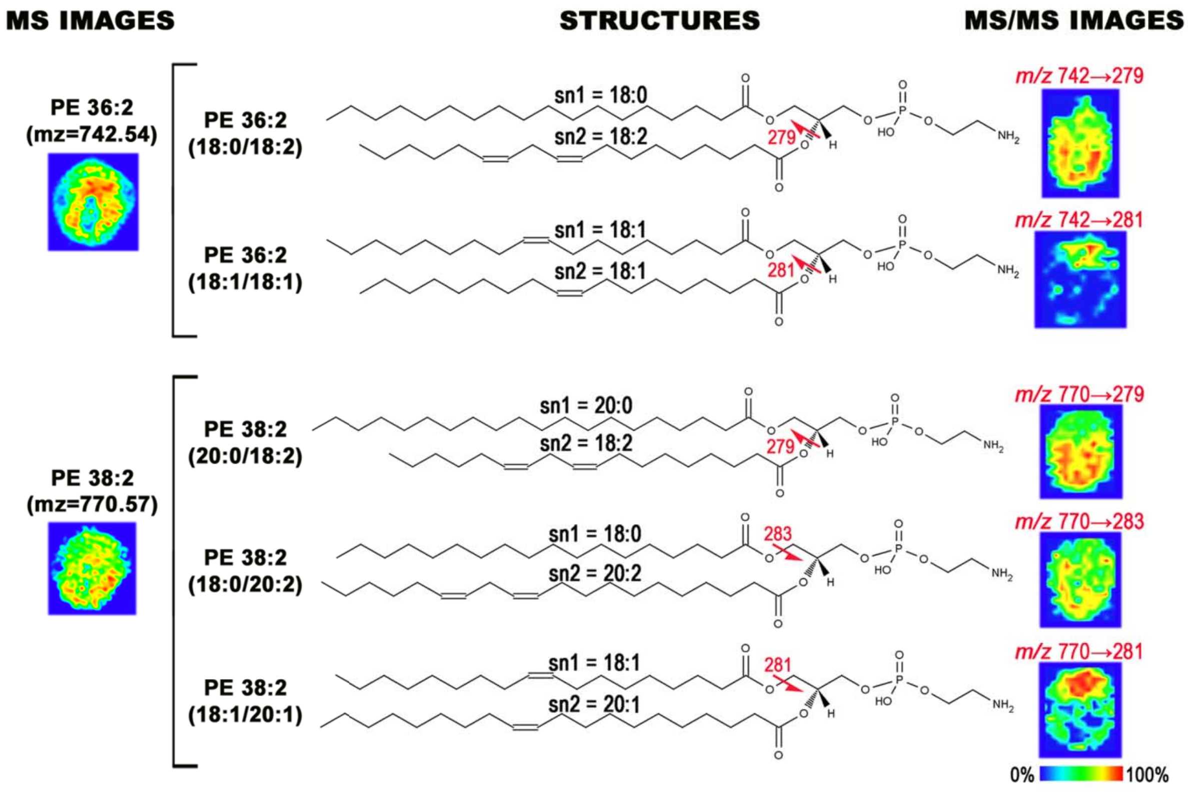

Figure 18. MS/MS imaging detects the spatial distribution of phospholipid isobars with identical masses. (Left) FTICR MS images of phospholipids PE 36:2 and PE 38:2. (Middle) Structure of each isobaric species for PE 36:2 and PE 38:2. **(Right)** MS/MS images of the most intense fragment ion for each parent phospholipid.

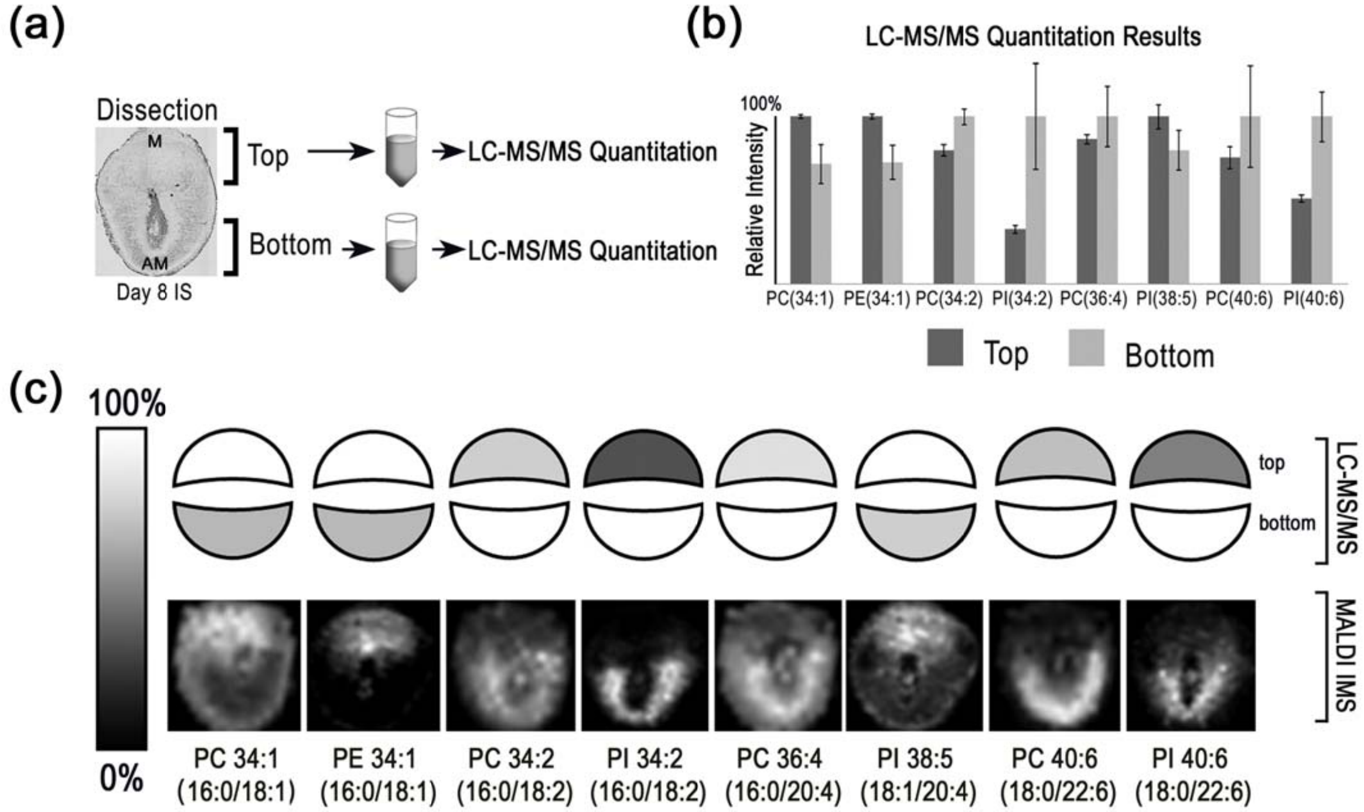

Figure 19. Quantation of phospholipids: LC-MS/MS data from implantation sites on day 8 of pregnancy correlates with MS images. **(a)** Workflow for micro-dissection of top (M pole) and bottom (AM pole) of uteri for subsequent LC-MS/MS analysis. **(b)** LC-MS/MS quantitative results for selected phospholipids between the top and bottom of day 8 implantation sites. **(c)** Block figures representing LC-MS/MS data (data from panel b) with corresponding MALDI-FTICR images below.

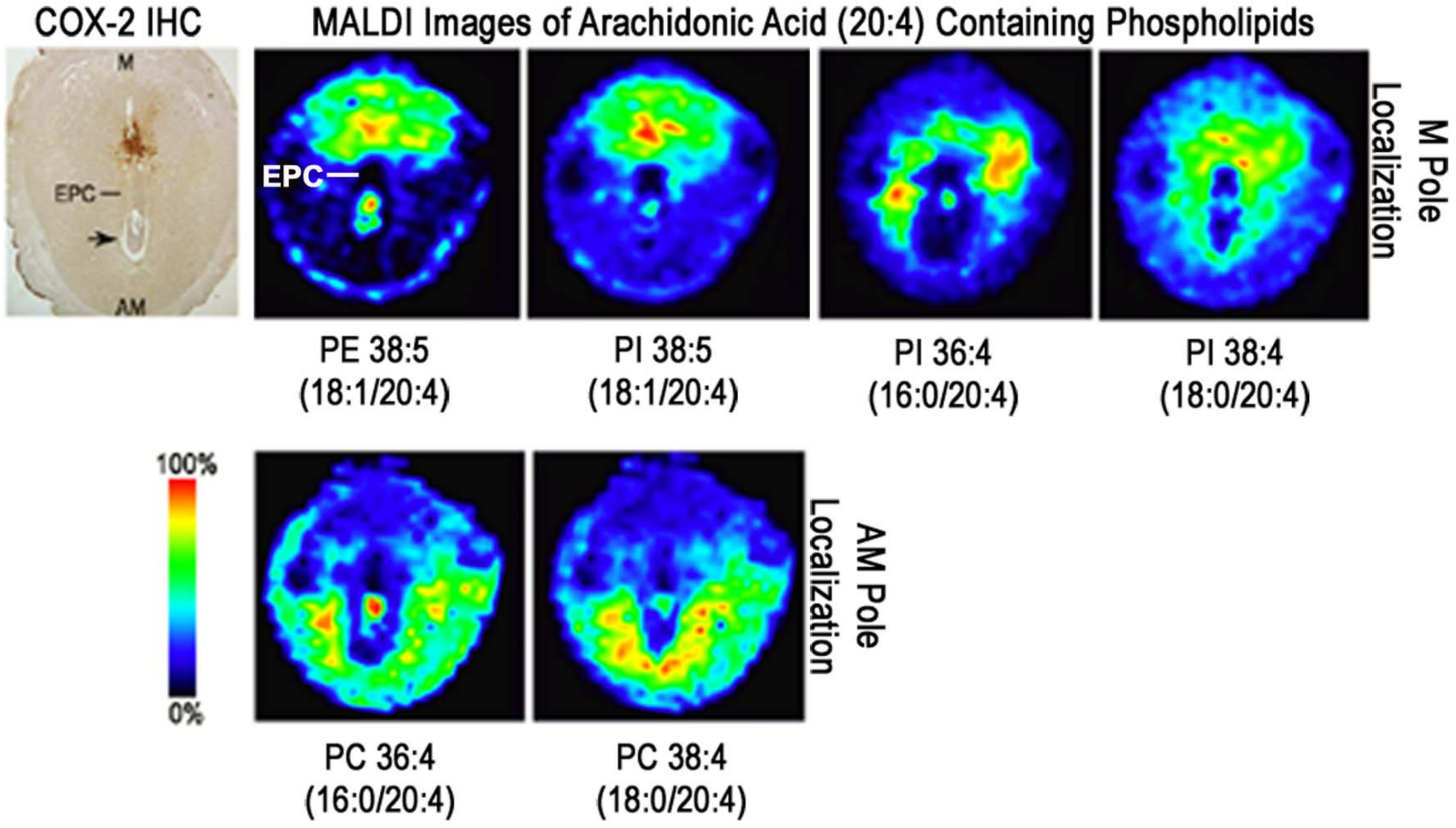

Figure 20. Colocalization of arachidonate-containing phospholipids with cyclooxygenase-2 (COX-2). Immunohistochemistry (IHC) stain of COX-2 on day 8 of pregnancy ***(left)***. MALDI images of arachidonic acid containing phospholipids on day 8 of pregnancy ***(right)***. Black arrow, embryo.

Table 1

Assignment of lipid molecular species in MS/MS positive ion mode

Class	Molecular species (C1 acyl chain/ C2 acyl chain)	Ion Type	*m/z* [a]	Lithium induced MS/MS Peaks ^
SM	**16:0**	[M+H]$^+$	703.573	650
		[M+Na]$^+$	725.555	
		[M+K]$^+$	741.529	
PC	32:0 (16:0/**16:0**)	[M+H]$^+$	734.568	681, 551, 557, 484, 425, 478
		[M+Na]$^+$	756.551	
		[M+K]$^+$	772.526	
PC	34:0 (16:0/**18:0**)	[M+H]$^+$	762.6	709, 579, 585, 484, 425, 512, 506, 453
		[M+Na]$^+$	784.581	
		[M+K]$^+$	800.554	
PC	34:1 (16:0/**18:1**)	[M+H]$^+$	760.584	707, 583, 577, 510, 451, 478, 484, 425
		[M+Na]$^+$	782.564	
		[M+K]$^+$	798.539	
PC	36:1 (18:0/**18:1**)	[M+H]$^+$	788.614	735, 611, 605, 510, 451, 506
		[M+Na]$^+$	810.594	
		[M+K]$^+$	826.569	
PC	34:2 (16:0/**18:2**)	[M+H]$^+$	758.568	705, 581, 575, 508, 449, 478, 484, 425, 502
		[M+Na]$^+$	780.548	
		[M+K]$^+$	796.524	
PC	36:2 (18:0/**18:2**)	[M+H]$^+$	786.6	733, 609, 603, 508, 449, 506, 512, 453, 502
		[M+Na]$^+$	808.581	
		[M+K]$^+$	824.554	
PC	36:4 (16:0/**20:4**)	[M+H]$^+$	hidden by 34:1 Na+	729, 605, 599, 532, 473, 478, 425, 484
		[M+Na]$^+$	804.55	
		[M+K]$^+$	820.524	
PC	38:4 (18:0/**20:4**)	[M+H]$^+$	no peak	633, 757, 627, 532, 473, 506, 526, 512, 453
		[M+Na]$^+$	832.58	
		[M+K]$^+$	848.554	
PC	40:6 (18:0/**22:6**)	[M+H]$^+$	834.596	781, 657, 651, 556, 497, 506, 453, 512
		[M+Na]$^+$	856.581	
		[M+K]$^+$	872.554	

[a] Data acquired on a MALDI-FTICR MS

^ arrangement - highest intensity ion (left) to lowest intensity ion (right) in the MS/MS spectra (decimal values not included)

Table 2

Assignment of lipid molecular species in MS/MS negative ion mode

Class	*m/z* [a]	MS/MS Peaks ^	Molecular species (C1 acyl chain/ C2 acyl chain)
LPI	599.332	283, 419, 315	**18:0**
PE	716.528	281, 255, 452, 478	34:1 (16:0/**18:1**)
PG	747.521	281, 255, 391, 465, 483, 491, 509	34:1 (16:0/**18:1**)
PS	788.551	701, 419, 283, 417, 504	36:1 (18:0/**18:1**)
PI	857.522	553, 391, 571, 303, 255, 439, 601, 297	36:4 (16:0/**20:4**)
PI	885.553	581, 419, 283, 599, 601, 303, 439, 297, 619	38:4 (18:0/**20:4**)
PE	764.529	303, 281, 478	38:5 (18:1/**20:4**)
PI	883.541	579, 417, 281, 597, 601, 303, 297, 439, 619	38:5 (18:1/**20:4**)
PEp	750.549	331, 436	38:4 (16:0p/**22:4**)
PI	837.556	581, 419, 283, 553, 599, 391, 297	34:0 (18:0/**16:0**)
PI	833.523	553, 391, 577, 255, 571, 279, 297	34:2 (16:0/**18:2**)
PI	861.558	581, 419, 283, 577, 599, 415, 279, 297	36:2 (18:0/**18:2**)
PS	786.534	699, 419, 283, 415,279	36:2 (18:0/**18:2**)
PEp	746.517	327, 436, 418	38:6 (16:0p/**22:6**)
PI	909.556	581, 419, 283, 599, 625, 297, 327	40:6 (18:0/**22:6**)
PE	742.543	279, 283, 281, 480, 478	36:2 (18:0/**18:2**, 18:1/**18:1**)*
PE	770.575	279, 283, 281, 460, 508, 307	38:2 (20:0/**18:2**, 18:0/**20:2**, 18:1/**20:1**)*

[a] Data acquired on a MALDI-FTICR Mass Spectrometer

^ arrangement - highest intensity ion (left) to lowest intensity ion (right) in the MS/MS spectra (decimal values not included)

* acyl chain identities confirmed by MS/MS imaging

Supplementary Table 3. LC-MS/MS Data
Predominantly bottom expression (AM pole)

weights (mg tissue):	15	15	15	14.5	15	15
values below are ng lipid/mg tissue	**top1**	**top2**	**topM**	**bot1**	**bot2**	**BotM**
GPA(36:2)	6	5.6	5.2	8.2	10.8	6.1
GPA(38:4)	4.6	4.3	4.2	6.1	6.7	5.7
GPA(40:6)	12.9	13.4	11.2	19.7	18.9	13.9
GPCho(32:1e)/GPCho(32:0p)	1.1	0.6	1.1	1.9	1.7	1.3
GPCho(34:2)*	44.4	41.1	43.6	55.2	55.4	50.9
GPCho(36:4)*	71.9	69.0	73.7	97.1	67.2	83.6
GPCho(36:4p)	3.5	2	4.2	5.1	5.1	5.4
GPCho(38:4)	166.1	157.7	152.3	160.1	177.5	168.7
GPCho(38:6e)/GPCho(38:5p)	5	4.4	5.1	6.8	13.1	7
GPCho(40:6)*	77.2	67.8	79.9	80.1	133.9	83.9
GPEtn(34:2)	6.4	6.5	5.5	7.2	6.4	8
GPEtn(36:0)	41.3	30.2	40.9	52.2	62.7	43.3
GPEtn(36:4e)/GPEtn(36:3p)	4.4	2.8	4	5.3	4.7	4.6
GPEtn(38:4)	81.2	76.5	71.3	97	80.8	94.4
GPGro(36:3)	16.7	14.1	15.3	21.1	30.5	17.5
GPGro(36:4)	10.6	8.6	8.8	18.1	26.7	14.5
GPGro(38:1)	1.4	1	1.3	1.8	2.5	1.5
GPGro(42:10)	4.9	4	5	8.1	14.4	7
GPGro(44:10)	4.2	3.3	3.8	4.8	6.4	4.3
GPGro(44:11)	6.5	5.2	6.5	10.1	10.5	8.2
GPGro(44:12)	21.3	16.4	21.1	31	39.5	27.2
GPIns(32:0)	0.3	0.5	0.4	1	1.2	1.1
GPIns(34:1)	3.9	3.6	3.4	6.2	9	6.5
GPIns(34:2)*	4.3	3.9	4.5	11.4	17.6	9.9
GPIns(36:1)	1.6	1.7	1.9	4.1	5.4	3.8
GPIns(36:2)	6.2	6	6.6	16	22.1	13.2
GPIns(38:6)	1.7	1.5	1.3	2.9	3	2.4
GPIns(40:4)	1.8	1.7	1.9	2.6	2	2.3
GPIns(40:6)*	2.4	2.3	2.5	4.7	5.4	4
GPSer(38:4)	49.8	48.4	44.2	66.4	61.1	50.6
GPSer(42:8)	0.8	0.4	0	0.9	1.2	0.8
GPThr(38:4)	2.4	2.7	2.5	3.8	3.2	3

***LC-MS/MS data correlates with MALDI images**

Supplementary Table 3. LC-MS/MS Data
Predominantly top expression (M pole)

weights (mg tissue):	15	15	15	14.5	15	15
values below are ng lipid/mg tissue	**top1**	**top2**	**topM**	**bot1**	**bot2**	**BotM**
GPA(32:1)	0.9	0.7	0.8	0.6	0	0
GPA(34:1)	4.6	4	4	3.4	3.8	2.6
GPCho(30:0)	10.9	10.7	10.2	8.9	6.9	7.3
GPCho(32:1)	30.8	29.7	29.5	23.7	20.4	20.3
GPCho(34:0)	19.4	17	19.5	14.4	12.5	14.4
GPCho(34:0e)	2.5	2	2.2	1.5	1.8	1.4
GPCho(34:1)*	57	55.7	56.5	46	33.3	42.1
GPCho(34:1e)/GPCho(34:0p)	11.3	12.1	10.2	9	9.2	7.1
GPCho(36:1)	74.1	73.3	73.2	54.2	60.8	55.2
GPCho(36:1e)/GPCho(36:0p)	1.4	1.2	1.1	0.7	0.8	0.7
GPCho(36:3)	49.2	48.7	49	40.9	39	41.6
GPCho(38:2)	8	8.3	7.5	3.3	4.4	3.4
GPCho(38:5)	48.7	45.8	45.3	39.9	33.8	38.8
GPCho(40:1)	29.8	24.3	29.1	25.8	22.9	22.5
GPCho(40:7)	20.5	15.6	17.4	12	10.4	12.6
GPEtn(32:0)	1.2	1.1	0.8	0.6	0	0.5
GPEtn(32:1)	0.8	0.7	0.9	0.4	0.3	0.5
GPEtn(34:0)	2.6	2.1	2.5	1.8	1.3	1.5
GPEtn(34:1)*	13.3	13.5	13.1	10.4	8.1	10.5
GPEtn(38:3e)/GPEtn(38:2p)	6.4	9.5	4.1	5.2	3.5	4
GPEtn(40:4e)/GPEtn(40:3p)	12.3	15.1	9.2	9.5	0	8.3
GPEtn(40:7)	19.5	18.3	18.4	18	16.3	16.4
GPEtn(42:10)	2.9	4	1.7	1.4	1.2	1.2
GPEtn(42:5)	1.8	1.9	1.6	1.4	1	1.3
GPGro(38:2)	0.9	0.8	0.7	0.5	0.6	0.5
GPIns(38:5)*	8.7	9.7	8.5	8.2	6.1	7.2
GPSer(34:1)	19.5	21.3	17.5	13.4	14.1	11.1
GPSer(38:1)	3.6	2.9	2.4	2.3	1.9	1.9
GPSer(40:2)	3	2.9	2.3	1.4	0.9	1.2
GPSer(40:3)	3.1	3.2	2.1	2.3	2.1	1.5
GPSer(42:3)	2.2	2.2	1.9	2	1.4	1.4

***LC-MS/MS data correlates with MALDI images**

CHAPTER IV.

DETECTING SPATIAL AND TEMPORAL DISTRIBUTIONS OF PROTEINS DURING EMBRYO IMPLANTATION BY MALDI IMAGING MASS SPECTROMETRY

A. Overview

Imaging mass spectrometry analysis of uterine sections provided molecular composition, relative abundance and spatial distribution of a large number of proteins during the embryo implantation period. This approach has allowed us for the first time to choreograph *in situ* proteome profiles of mouse implantation and interimplantation sites in a region and stage specific manner with the progression of implantation. This application is reliable since patterns of expression of several proteins displayed by imaging mass spectrometry correlate well with *in situ* hybridization and immunohistochemistry results. Interestingly, the use of this approach has provided new insights regarding uterine biology of $cPLA_{2\alpha}$ null females that show implantation defects.

B. Introduction

The heterogeneous cell types of the uterus, each with unique functions, pose a challenge for studying events during early pregnancy. This complexity is increased because their actions change, depending on their proximity to the implanting embryo and with pregnancy progression. Therefore, studying the uterine molecular landscape using conventional approaches presents a laborious task.

Although expression studies by *in situ* hybridization and immunohistochemistry have provided profiles of specific genes and their gene products during implantation and decidualization [1, 2], the *in situ* spatiotemporal distribution of a large number of gene products in uteri during implantation remains poorly understood. Here we used *in situ* imaging mass spectrometry to generate proteomic profiles in the periimplantation mouse uterus. Whereas mass spectrometry is an effective technology for identifying proteins and their post-translational modifications under various physiological conditions [15, 49], imaging mass spectrometry is a powerful tool for *in situ* analysis of proteome profiles on tissue sections [121, 111]. This technology allowed us for the first time to analyze hundreds of proteins involved in proliferation, differentiation and apoptosis during the periimplantation period, providing unique and differential proteomic blueprints of implantation and interimplantation sites. The uterine proteomic profile in mice lacking *Pla2g4a*, the gene encoding for cytosolic phospholipase $A_{2\alpha}$ (cPLA2α), was also compared with wild-type implantation sites, providing new insight regarding uterine biology in these null females that display implantation defects.

C. Results

C.i. Protein signatures differ within specific regions of implantation and interimplantation sites. Implantation in mice occurs at the anti-mesometrial pole of the uterus. On the afternoon of day 5 of pregnancy, the proliferating stromal cells surrounding the implanting embryo begin to differentiate into decidual cells, forming the avascular primary decidual zone (PDZ). By day 6, the PDZ is well differentiated and formed, and a secondary decidual zone (SDZ) forms around the PDZ, coinciding with the cessation of proliferation in the PDZ with continuing proliferation in the SDZ. The SDZ is surrounded by circular and longitudinal muscle layers, collectively referred to as the myometrium. In **Figure 21a,** the anti-mesometrial pole (AM), mesometrial pole (M), PDZ and SDZ are demarcated by faux matrix spots on a representative section from a day 6 implantation site (IS). This figure also depicts an interimplantation site (Inter-IS) which contains all the major cellular regions except the PDZ and SDZ, since they are formed in response to the implanting blastocyst (**Figure 21a**).

To characterize the proteome signatures between specific regions within the implantation and interimplantation sites, frozen sections from these sites on day 6 of pregnancy were thaw-mounted onto glass slides and subjected to profiling mass spectrometry analysis. Briefly, matrix spots (230µm in diameter) were deposited on particular areas of interest (**Figure 21a**). Profiling mass spectrometry generated spectra from those matrix spots, where each mass-to-charge (*m/z*) value corresponds to a unique protein which is subsequently identified. In this analysis, approximately 230 distinct peaks were found within the optimal mass range, which for MALDI-time-of-flight-mass spectrometry (MS) is 2–30 kilodalton (kDa). This is dictated by instrumental parameters. The instrument is operated under delayed extraction conditions; thus, enhanced sensitivity, resolution and mass accuracy are observed for ions less than 50,000 Da. Microchannel plate detection is velocity dependent; thus, higher molecular mass ions (having lower velocities) have lower probabilities of being detected unless they are highly abundant. Clusters of matrix molecules below 2,000 Da complicate the mass spectra and potentially mask expression of low-molecular-mass peptides.

Statistical analyses of spectra from IS and inter-IS revealed 50 peaks as significantly changed due to the presence and proximity of the embryo. The average mass spectra from specific uterine regions for ubiquitin (*m/z* 8565), calgizzarin (*m/z* 10952), calcyclin (*m/z* 9962) and transthyretin (*m/z* 13641) are shown in **Figure 21b**. These four proteins were selected and chosen for further analysis because of their unique expression patterns in the uterus and their reported involvement during pregnancy [122-124]. In addition, these proteins are known to participate in protein degradation, cell differentiation, cell proliferation and retinol binding, respectively. Statistical analysis shows that ubiquitin is up-regulated at IS by 3.4-fold, compared with inter-IS on d 6 of pregnancy. In contrast, calcyclin and calgizzarin are up-regulated by 5.2- and 2-fold, respectively, in the PDZ, compared with the SDZ, whereas transthyretin is up-regulated in the SDZ near the antimesometrial pole (5.1-fold higher in the SDZ, compared with the PDZ, and 2.9-fold higher in antimesometrial pole, compared with the mesometrial pole). Unique spatial locations of these proteins, as determined by imaging mass spectrometry, are described below.

To view these spatiotemporal differences in expression, implantation and interimplantation sites were sectioned on days 5, 6, and 8 of pregnancy and prepared for imaging mass spectrometry. Using this technique, a raster of the entire tissue section produces an ordered array of mass spectra that generates 2D images showing localization of each *m/z* value in the X and Y direction. Our analysis shows that ubiquitin is expressed at higher levels at implantation sites on days 6 and 8 of pregnancy compared with interimplantation sites (**Figure 22a, upper**). Calcyclin is expressed at higher levels immediately adjacent to the implanting embryo with expression concentrated at the antimesometrial pole on day 8 (**Figure 22b, upper**). While the expression of calgizzarin is also primarily localized at the antimesometrial pole on both days 6 and 8 of pregnancy (**Figure 22c, upper**), transthyretin expression is prominent along the outer edge of the stroma underlying the myometrium (**Figure 22d, upper**).

C.ii.a. **Correlating protein images with mRNA localization using *in situ* hybridization.** To determine whether proteins identified by imaging analysis correlates with their mRNA localization, *in situ* hybridization of *ubiquitin, calcyclin, calgizzarin and transthyretin* with ^{35}S-labeled probes was performed on frozen uterine sections from the corresponding days of pregnancy. We found a high correlation between protein and mRNA localizations with the exception of *transthyretin* whose transcripts were detected at low levels in the uterus with an interesting pattern in the day 6 and day 8 embryos (**Figure 22a, b, c, and d, lower**). It can be speculated that imaging did not detect transthyretin in day 6 and 8 embryos because it could be detected at a different mass in these regions due to posttranslational modifications. In addition, imaging mass spectrometry showed distinct expression patterns of a large number of proteins on days 4, 5, 6, and 8 of pregnancy (**Figure 23** and **Table 4**). Differential region-specific distribution of these proteins on day 6 of pregnancy with their potential biological functions is depicted in **Figure 23** and **Table 4**. It is interesting to note that the SDZ shows relative increases in proteins involved in energy production and proliferation, characteristic processes occurring in this zone. Conversely, the PDZ shows increases in proteins influencing hormone signaling.

C.ii.b. **Immunohistochemistry and activity assays confirm protein identification and spatial distribution**. Immunohistochemistry (IHC) was performed in sections of day 6 (D6) implantation sites for Purkinje Cell Protein 4 (PEP-19). Both IHC and IMS showed PEP-19 localization to predominantly be in the muscle layer (myometrium) surrounding the uterus (**Figure 24a**). IHC was also performed in sections of day 8 (D8) implantation sites for calcyclin, calgizzarin and transthyretin to see whether mass spectra correlate with immunolocalization. The results show that localization patterns of these four proteins are in agreement with mass spectra, although immunohistochemistry also detected expression of transthyretin in the embryo (**Figure 24a**). In **Figure 24b**, the enzymatic activity of cytochrome c oxidase (COx), a multi-subunit complex within the mitochondrial respiratory chain, was compared to the IMS results of one of the COx subunits, VIb, on day 5 (D5), D6, and D8. Both experiments showed increased expression in the lumen and embryo on D5, in the uterine stroma around the embryo on D6, and in the uterine stroma in the bottom (AM) pole on D8 (**Figure 24b**).

C.ii.c. **Isotope Coded Affinity Tag based protein profiling confirms profiling and imaging mass spectrometry experimental results.** Isotope Coded Affinity Tag (ICAT) labeling methods and LC-MS/MS analyses were used to quantify and identify proteins in implantation and interimplantation sites on day 6 of pregnancy (**Figure 25**). ICAT results showed a relative expression increase in the implantation sites for thioredoxin 1 and 40S ribosomal protein S28 and S21 by 28%, 35% and 22%, respectively; whereas, macrophage migration inhibitory factor showed a 25% increase in interimplantation sites (**Figure 25, *left***). Consequently, the ICAT data matched the profiling and imaging mass spectrometry data (**Figure 25, *middle and right***). Although, relative protein expression changes were much less in our ICAT study compared to profiling and imaging experiments we were able to conclude even small changes (>10%) were statistically significant (see Materials and Methods for details). One of the limiting factors for the ICAT study was the availability of adequate amounts of tissues, since 100 mg of protein was needed from each sample type. Entire IS and Inter-IS were homogenized, yet most molecules only localize to particular cell types, explaining why ICAT only detected small changes in protein expression.

C.iii. **Exploring protein expression along the Z-axis of a day 6 implantation site.** Imaging mass spectrometry was also used to analyze serial sections of a day 6 implantation site to explore the relative protein expression in the Z direction (**Figure 26a**). As shown in **Figure 26b**, ubiquitin, calcyclin, and calgizzarin all show varying expression patterns in the uterine stroma depending on their proximity to the implanting embryo, whereas expression of purkinje cell protein 4 remains relatively unchanged in the myometrium.

C.iv. **Characterizing differential proteome profiles in the Pla2g4a null mice.** The success of our application of IMS in wild-type periimplantation uteri prompted us to utilize this approach in *Pla2g4a* null females with known defects in implantation. *Pla2g4a* encodes cytosolic phospholipase $A_{2\alpha}$ (cPLA2α) which liberates arachidonic acid from membrane phospholipids for prostaglandin biosynthesis by the cyclooxygenase system [125-127]. Our previous study suggested that compromised pregnancy outcome in *Pla2g4a* null females results from deferral of on-time implantation, leading to subsequent retarded fetoplacental development and reduced litter sizes [95]. This study advanced a new concept that a short delay in the initial attachment reaction propagates detrimental ripple effects later in pregnancy. This is now supported by a more recent study using *Lpa3* null mice [95, 104]. This deferred implantation phenomenon in *Pla2g4a* null females results in both “on-time” and “deferred” implantation sites, morphologically distinguishable by their differing sizes on day 6 of pregnancy (**Figure 27, *left***).

We used profiling and imaging mass spectrometry to address whether proteome signatures on day 6 of pregnancy differ between on-time implantation sites in wild-type and *Pla2g4a* null mice and between on-time and deferred implantation sites in *Pla2g4a* null females. We speculated that while proteome profiles of "on-time" implantation sites in *Pla2g4a* null females would be similar to those of wild-type females, deferred implantation sites in *Pla2g4a* null females would be more similar to day 5 implantation sites in wild-type females. Surprisingly, we found that while expression/localization of some proteins did show remarkable changes, these differences were mostly attributed to the lack of *Pla2g4a* rather than to differences in implantation timing (**Figure 27, *middle* and Figure 28**).

The four proteins that were characterized in wild-type day 6 uteri were selected for further analysis in *Pla2g4a* null uteri. While the expression of ubiquitin did not differ dramatically between WT and *Pla2g4a* null uteri, calgizzarin, calcyclin, and transthyretin showed pronounced differences. Specifically, calgizzarin expression was found to be reduced in *Pla2g4a* null uteri, but more interestingly, its localization shifted to the luminal epithelium in null uteri as opposed to its predominant expression in the antimesometrial decidua of wild-type uteri (**Figure 27, *middle and right***). Calcyclin expression was evident in the PDZ of wild-type uteri, and in the implanting embryo in *Pla2g4a* null females, with lowest expression in deferred implantation sites in *Pla2g4a* null females (**Figure 27, *middle and right***). In contrast, the expression of transthyretin was higher in deferred implantation sites compared with on-time implantation sites in *Pla2g4a* or wild-type females (**Figure 27, *middle and right***).

Previous characterization of *Pla2g4a* null mice inferred that while a short deferral of on-time implantation leads to subsequent developmental defects, those that implanted on-time developed normally during the subsequent course of pregnancy. However, our proteomics results suggest that proteome signatures differ between wild-type and *Pla2g4a* null uteri regardless of the timing of implantation. These are exciting results that will provide deeper understanding of the implantation process.

D. Discussion

In situ localization and identification of a broad proteomic landscape in a given region of tissues remains difficult with current labeling procedures. Therefore, direct analysis of tissue sections by matrix-assisted laser desorption/ionization (MALDI) mass spectrometry holds great potential. Both direct tissue profiling and imaging provide region-specific detailed assessment of the complex protein patterns within a tissue. These techniques also have the advantage of interrogating tissues for protein identification and localization without the limitation of selecting specific proteins for analysis. The present data provide novel proteomic approaches to identify protein signatures within and between implantation sites during the periimplantation period.

In this study, four proteins of interest were selected for more detailed analysis because of their unique uterine expression patterns. Interestingly, these proteins have previously been implicated to play roles during pregnancy. For example, *calcyclin* is known to be expressed at high levels in day 8 and day 9 decidua [124] and it influences placental lactogen secretion in mice [122]. Although our imaging mass spectrometry results show similar expression pattern of calcyclin protein on day 8 of pregnancy, its differential expression pattern in periimplantation uteri suggests that calcyclin is also important for early pregnancy events. In contrast, roles for calgizzarin in early pregnancy remain largely unexplored. However, one study identified this protein as a downstream target of neurokinin B (NKB), which is secreted at high levels from the placenta during preeclampsia, and is known to suppress calgizzarin expression [128]. These results suggest that calgizzarin has beneficial roles in pregnancy maintenance. This contention is supported by our present findings of reduced calgizzarin expression in *Pla2g4a* null females which display implantation, decidualization and placental defects [95].

Transthyretin, a protein involved in transporting both thyroxin and retinol-binding protein, is aberrantly expressed in placental tissues of patients with pregnancy loss, suggesting its important role in placentation [129, 130]. Indeed, *Ttr* mRNA is detected in human placentas with protein expression specifically in the syncytiotrophoblast [123]. While our studies focused on implantation and early pregnancy events, it will be of great interest to use this proteomic approach to determine differential proteome profiles during later events of pregnancy including placentation.

Our success in employing imaging mass spectrometry to study uterine biology in wild-type mice during normal pregnancy provoked us to employ this approach to mice with known defects in implantation. We used *Pla2g4a* null mice to investigate whether the proteomic landscape differed between wild-type and null uteri. *Pla2g4a* null females show deferral of on-time implantation, leading to subsequent adverse ripple effects throughout the course of pregnancy and ultimately reduced litter size [95]. We hypothesized that those embryos that implant beyond the normal window of implantation undergo premature demise and those that implant on-time develop normally. However, our proteomics results suggest that proteome signatures differ between wild-type and *Pla2g4a* null uteri regardless of implantation timing. This finding is interesting and may help distinguish which proteins are critical for on-time implantation. In this respect, the power of IMS in generating proteome signatures within and between implantation sites is remarkable.

Dysregulation of events before, during, or immediately after implantation contributes to poor pregnancy outcome [2]. Therefore, understanding the interplay of numerous proteins during implantation is essential to identify potential targets for treating infertility and developing novel contraceptives approaches. This study examining differential protein signatures between and within implantation sites and interimplantation sites on different days of pregnancy has opened up a new avenue of exploring protein profiles and their interactions during normal and defective implantation.

E. Materials and Methods

Mice. Adult CD-1 mice were purchased from Charles River Laboratory (Raleigh, NC). Females were mated with fertile males of the same strain to induce pregnancy. Mice were sacrificed between 0900 and 1000 h on the specified day of pregnancy (day 1 = vaginal plug). The disruption of the *Pla2g4a* gene was originally achieved in J1 ES cells by homologous recombination as described [125]. Genotyping was by PCR analysis of genomic DNA. Implantation sites on days 5 and 6 of pregnancy were visualized by an intravenous injection of Chicago Blue dye solution, as previously described by us [87]. All mice in the present investigation were housed and used in accordance with the National Institutes of Health and institutional guidelines on the care and use of laboratory animals.

Protein profiling and imaging experiments. Implantation sites (IS) and interimplantation sites (Inter-IS) were dissected from the uterus, snap-frozen, sectioned (11 μm) in a cryostat, thaw-mounted onto matrix-assisted laser desorption/ionization (MALDI) mass spectrometry compatible glass slides and rinsed in a series of reagent grade ethanol/water washes (70% for 30 seconds (s), 70% for 30 s, and 100% for 15 s). A thin layer of fine sinapinic acid (SA) crystals was applied to vacuum dried tissue sections (seeding). Mechanical grinding with a mortar and pestle results in 1-40 μm sized crystals. An Acoustic Reagent Multispotter (Labcyte Inc, Sunnyvale, CA) was used to deposit SA matrix spots (25 mg/ml in 50% Acetonitrile (AcN), 0.1% Trifluoroacetic acid (TFA)) over distinct regions of IS and Inter-IS [131]. Different matrix deposition techniques were used for the profiling experiment (13 drops [stop/start mode] 3 passes) and the imaging experiment (1 drop [start/stop mode] 5 passes). All experiments were performed in the linear mode geometry on an Autoflex MALDI-TOF-MS (Bruker Daltonics, Billerica, MA) equipped with a solid-state Smartbeam laser operating at 100 Hz. The experimental design is illustrated in **Figure 29**.

In the profiling study, matrix spots (230µm in diameter) were deposited over unique cell types within the IS and Inter-IS. In the imaging study, uterine sections were uniformly spotted with SA matrix solution (120µm in diameter, 150µm center to center spacing defining the resolution). A partial 3D study explored the influence of the embryo along the Z axis on day 6 of pregnancy. A section of mouse uterus containing an IS flanked on one side by Inter-IS was analyzed. Every fifth section (55µm apart) was collected until the embryo was reached and then every section was collected. After analysis, the distance of each uterine section from the center of the IS (location of embryo) was calculated. All images directly compared were run on the same day and on the same MALDI glass plate.

Spectra preprocessing. For all studies, Pro TS-Data (Biodesix Inc. Steamboat Springs, CO) was used for spectra processing. Spectra from profiling and imaging experiments were baseline subtracted and normalized to the total ion current (sum of all intensities in the entire spectrum [TIC]) [35]. To ensure this spectral processing does not alter the spatial localization of protein images we compared the normalized and un-normalized images for each protein of interest

(**Figure 30**). Normalization adjusts for pixel to pixel variations but the overall spatial localization is not altered in **Figure 30**. Normalizing the data makes it possible to compare data acquired on different days as demonstrated by **Figure 31**. The study in **Figure 31** analyzed a mouse implantation site from day 6 of pregnancy. Sections were collected through the center of the implantation site, washed and matrix was applied using a robotic spotter as described above. Mass spectra acquisition was carried out on one section at a time every third day for 2 weeks. MS preprocessing consisted of noise removal, baseline subtraction and TIC normalization. Three proteins were visualized on each section; PEP-19 (green), 40S ribosomal protein S28 (red), and homeodomain-only protein (blue). Each of these proteins localized to a different tissue type: PEP-19 to the muscle surrounding the uterus, 40S ribosomal protein S28 to the uterine stroma, and homeodomain-only protein to the embryo. Most importantly, both spatial localization and peak intensity information were retained throughout the two week period of MS acquisition. The results reflect the general stability of spotted tissue sections over time, stored in a vacuum dessicator; thereby, supporting previously published results [132].

Statistical Analysis. In profiling studies of different cell types in wild-type mice, three sections were taken from each mouse (n=5) at either the implantation site or interimplantation site. For each section, 1 to 3 spectra were acquired within each different cellular region. In the profiling study of *Pla2g4a* null mice, 7 to 10 sections were taken from each *Pla2g4a* null mouse with either on-time implantation or deferred implantation, and from each wild-type mouse with on-time implantation. About 7 spectra were acquired for each section. Following processing, multiple spectra from each individual animal were averaged over each cellular region of implantation and interimplantation sites. Features were extracted from the average spectrum. For imaging, Biomap (Novartis, Basel, Switzerland) was used for plotting 2D ion density maps (x and y dimension) of selected mass-to-charge (*m/z)* values (wild-type [n ≥ 3 for each day of pregnancy analyzed] and *Pla2g4a* [n ≥ 3 for differed and on-time ISs and Inter-ISs]).

Statistical analysis of wild-type [n=30] and *Pla2g4a* null [n=30] profiles revealed peaks of significance. Significance Analysis of Microarrays (SAM) for paired data was used to identify significant features between different cell types [133]. SAM computes a statistic for each feature which is a measurement of difference in group means standardized by pooled within-group standard deviation. SAM then uses a permutation method to evaluate the significance of the statistics of each feature. False discovery rate (FDR) was used to control for the multiple testing. An FDR less than 0.0001 was used as the cutoff for concluding a set of features significant.

Protein identification experiments. Excised day 6 and day 8 ISs were homogenized in Tissue Protein Extraction Reagent (TPER; Pierce, Rockford, IL) supplemented with protease inhibitors. For each extract, a Vydac C8 polymeric reversed-phase column (3.2 x 150mm) fractionated 300 µg of protein solution (96 min linear gradient from 2-90% Acetonitrile in 0.1% TFA) into a 96-well PCR plate. During separation, a liquid handling robot moves the transfer capillary sequentially into each of the 96 wells at 1 min intervals. To identify wells containing proteins of interest in an automated process, 0.2 μL was removed from each well, mixed with SA matrix, and analyzed by MALDI-MS (Bruker Autoflex). Fractions containing *m/z* values of interest were run on a gel (10-20% tricine) and bands of interest were excised and digested with trypsin gold (Promega; Madison, WI). In solution trypsin digest was also performed on fractions which contained *m/z* values of interest. Either an LTQ or LCQ (Thermo Scientific; Waltham, MA) was used to analyze digested proteins. The peptides were separated on a packed capillary column, 75 μm x 10.5 cm, with C18 resin (Monitor C18, 5 μm; Column Engineering, Ontario, CA), using a linear gradient (5% to 95% Acetonitrile in 0.1% formic acid in water) delivered at 250 nL/min. MS/MS spectra were initially analyzed by searching the mouse International Protein Index database using Sequest software [134]. ProteinProphet software was then used to determine the probability that a protein had been correctly identified, based on the available peptide sequence evidence (**Figure 32**) [135, 136].

***In situ* hybridization.** The cDNA clones for *Calgizzarin*, *Calcyclin*, *Transthyretin*, and *Ubiquitin* were generated by RT-PCR using the following specific primers: *Calgizzarin (*191 bp), 5'-GCA TTG AGT CCC TGA TTG CT-3' and 5'-ATC TAG CTG CCC GTC ACA GT-3'; *Calcyclin (*165 bp), 5'-CAA GGA AGG TGA CAA GCA CA-3' and 5'-AAG GCG ACA TAC TCC TGG AA-3'; *Transthyretin (*358 bp), 5'-GCT TCC CTT CGA CTC TTC CT-3' and 5'-CAG AGT CGT TGG CTG TCA

AA-3'; *Ubiquitin (*235 bp), 5'-GGT AAG ACC ATC ACC CTG GA-3' and 5'-TCT TGC CTG TCA GGG TCT TC-3'. For *in situ* hybridization, sense or antisense ^{35}S-labeled probes were generated by using appropriate polymerases from cDNAs as previously described by the Dey lab [88]. Sections hybridized with sense probes showed no signal and served as negative controls. Probes had specific activities of approximately 2 x 10^9 dpm/µg.

Immunohistochemistry. Antibodies used included PEP-19 (provided by Dr. Malin Andersson, Stockholm, Sweden), Ubiquitin (Calbiochem, San Diego, CA), Calgizzarin (Proteintech Group, Chicago, IL), Calcyclin (Santa Cruz Biotechnology, Santa Cruz, CA) and Transthyretin (Santa Cruz Biotechnology). Localization of protein in formalin-fixed paraffin-embedded uterine sections (5 µm) was achieved as previously described [120]. In brief, after deparaffinization and hydration, sections were subjected to antigen retrieval using a pressure cooker in 10 mmol/L sodium citrate solution (pH 6.0) for 20 minutes. A Histostain-Plus kit (Zymed, San Francisco, CA) was used to visualize the antigen; brown deposits indicate sites of positive immunostaining.

***In Situ* Cytochrome c oxidase activity staining in implantation sites.** COx activity tissue staining was performed according to previously published protocols [137]. In brief, cytochrome c oxidase (COx) enzyme complex activity was visualized by immersing tissue sections in COx activity buffer (PBS [pH 7.4] containing 0.05% Di-amino benzidinetetrachloride [DAB], 0.02% reduced cytochrome *c*, and 4% sucrose). COx oxidizes cytochrome *c*, which then oxidizes DAB to form a red-colored precipitate. After incubation, sections were washed with water, dehydrated with increasing concentrations of ethanol (50%, 70%, 95%, 100%, and 100%) and xylene.

Isotope Coded Affinity Tag (ICAT) based protein profiling. The ICAT analysis of Implantation sites (IS) and control interimplantation sites (Inter-IS) from day 6 of pregnancy was carried out using the commercially available cleavable ICAT Reagent Kit (Applied Biosystems, San Francisco, CA, USA) according to the instructions provided by manufacturer. Briefly, excised day 6 IS and Inter-IS were homogenized in Tissue Protein Extraction Reagent (TPER; Pierce, Rockford, IL) supplemented with protease inhibitors. Equal protein concentrations (100 µg) were used for the ICAT analysis. After reduction and denaturation, the IS and Inter-IS samples were labeled with biotin-conjugated ^{12}C (light) and ^{13}C (heavy) reagents at 37°C for 2 hr, respectively. The two ICAT-labeled samples were combined and digested with trypsin at a ratio of 1:10 with respect to the sample protein concentration at 37°C for 12 to 16 hr. The digest was acidified and loaded into a cation exchange column equilibrated with 10 mM KH_2PO_4/25% acetonitrile, pH 2.5-3.3. After neutralization, the biotinylated-ICAT-labeled peptides were purified by avidin affinity cartridge prepared as per the manufacturer's instructions. ICAT-labeled peptides were eluted with 30% acetonitrile, 0.4% trifluoroacetic acid in water. The eluted peptides were evaporated to dryness and reconstituted in 100 µl of cleavage reagent for 2h at

37ºC to cleave the biotin portion of the tag from the labeled peptides. The cleaved peptides were evaporated to dryness and re-suspended in aqueous solvent (100 µl H_2O/0.1% formic acid). Separations were carried out on an on-line capillary LC system in reverse phase mode prior to MS/MS analysis using a LTQ (Thermo Scientific; Waltham, MA). Gas-phase fractionation methods were used to increase proteome coverage; therefore, the mixture was analyzed six separate times, with the mass spectrometer selecting ions for fragmentation from a subset of the entire mass range for each run (*m/z* ranges: 400-500, 500-600, 600-700, 700-800, 800-1000, 1000-2000) [138]. Protein ID's were carried out using SEQUEST/ProteinProphet, and quantified in XPRESS.

ICAT analysis of IS and Inter-IS identified over 200 proteins (criteria > 1 peptide/ protein; Trans-Proteomic Pipeline score of 1.0). β-actin and β-tubulin are known to be equally abundant in IS and Inter-IS (relative ratios should be equal to one). This data was useful in determining an approximate acceptable cutoff for fold changes in abundances for proteins of interest. The three β-actin peptides analyzed had an average error of 7% from 1 (see table below). The four β-tubulin peptides had an average error of 7.5% from 1. Due to the small standard deviation even small changes in protein abundance between implantation sites and interimplantation sites are probably significant.

Actin Peptides Quantified with ICAT Labels	**IS : Inter-IS**	**Average Error from 1:1**
L**C**YVALDFEQEMATAASSSSLEK	0.94 : 1	**0.07 = 7%**
CPEALFQPSFLGMES**C**GIHETTFNSIMK	0.90 : 1	
CDVDIR	1 : 0.95	

ICAT measured expression levels of some proteins with important roles in implantation are listed below (**% higher in IS**). *Also observed to increase in the profiling/ imaging studies, ^Proteins known to be increased in IS

Alpha-2-macroglobulin / pregnancy zone protein (**80%**)^, Protein Disulfide Isomerase A3 (**66%**), Transferrin (**57%**), 40S ribosomal protein S28 and S21 (**35% and 22%**)*, Alpha-2-HS-glycoprotein (**33%**)^, Stress induced phosphoprotein (**30%**), Hemopexin (**30%**), Implantation serine proteinase (**28%**)^, Thioredoxin 1 (**28%**)*, Esterase (**26%**), Calreticulin (**24%**), Complement C3 (23%), Antithrombin (**20%**), Macrophage Migration Inhibitory Factor (**Decreased 25% in IS**)*

F. Acknowledgments

Mice were supplied by Sudhansu K. Dey's Lab. Sections were provided by Takiko Daikoku and Susanne Tranguch (Sudhansu K. Dey's Lab). Statistical analysis was done in collaboration with Deming Mi. *In situ* hybridization experiments were done in collaboration with Susanne Tranguch (Sudhansu K. Dey's Lab).

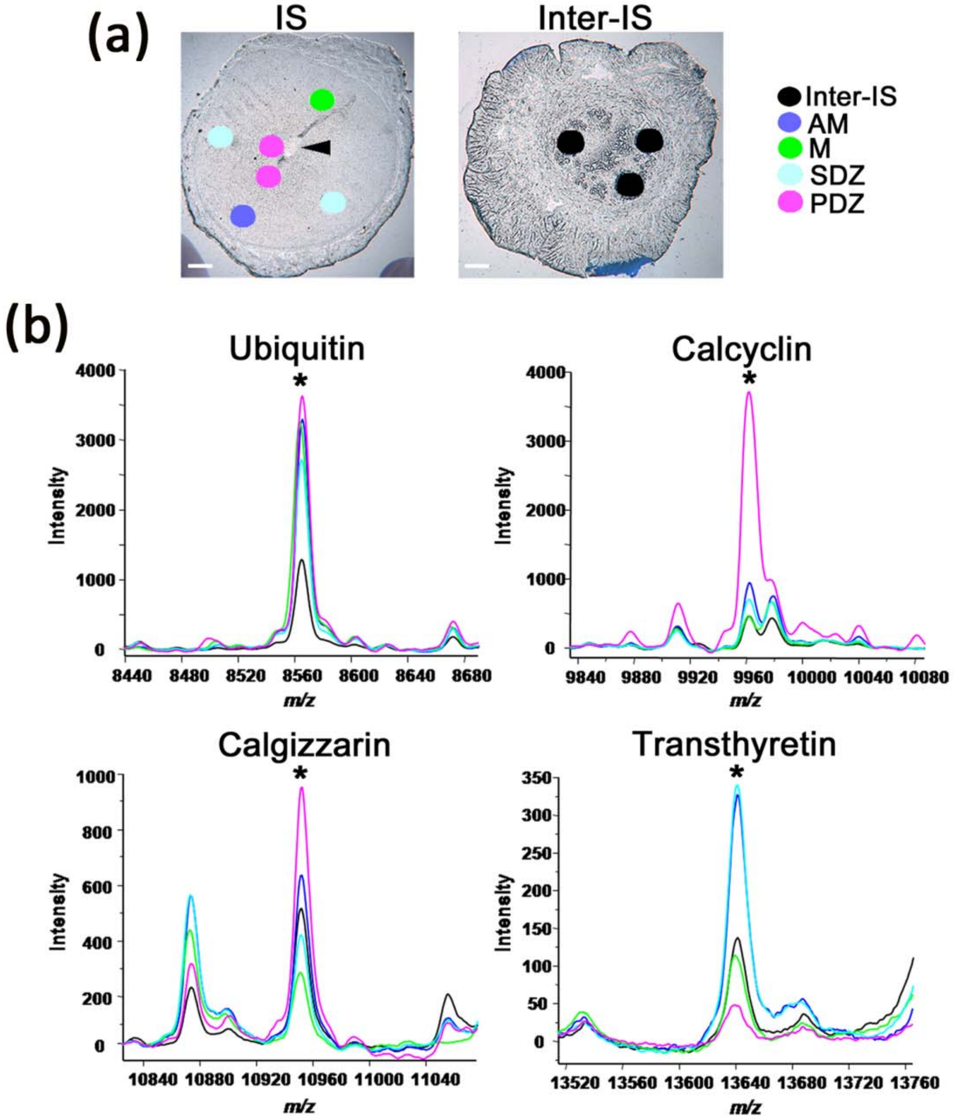

Figure 21. Profiling mass spectrometry reveals differential proteome profiles between and within implantation sites (IS) and interimplantation sites (Inter-IS). (a) A representative photomicrograph of a uterine section of an IS and Inter-IS on day 6 of pregnancy. Arrowhead denotes the location of implanting blastocysts. **(b)** Average mass spectra for Ubiquitin, Calcyclin, Calgizzarin and Transthyretin obtained from highlighted spots of IS and Inter-IS. Abbreviation: M, mesometrial pole; AM, antimesometrial pole; PDZ, primary decidual zone. SDZ, secondary decidual zone; *, peak, m/z protein of interest. Bar, 230 µm.

Image adapted from: Burnum, K.E. et al. Journal of Endocrinology 149, 3274-3278 (2008)

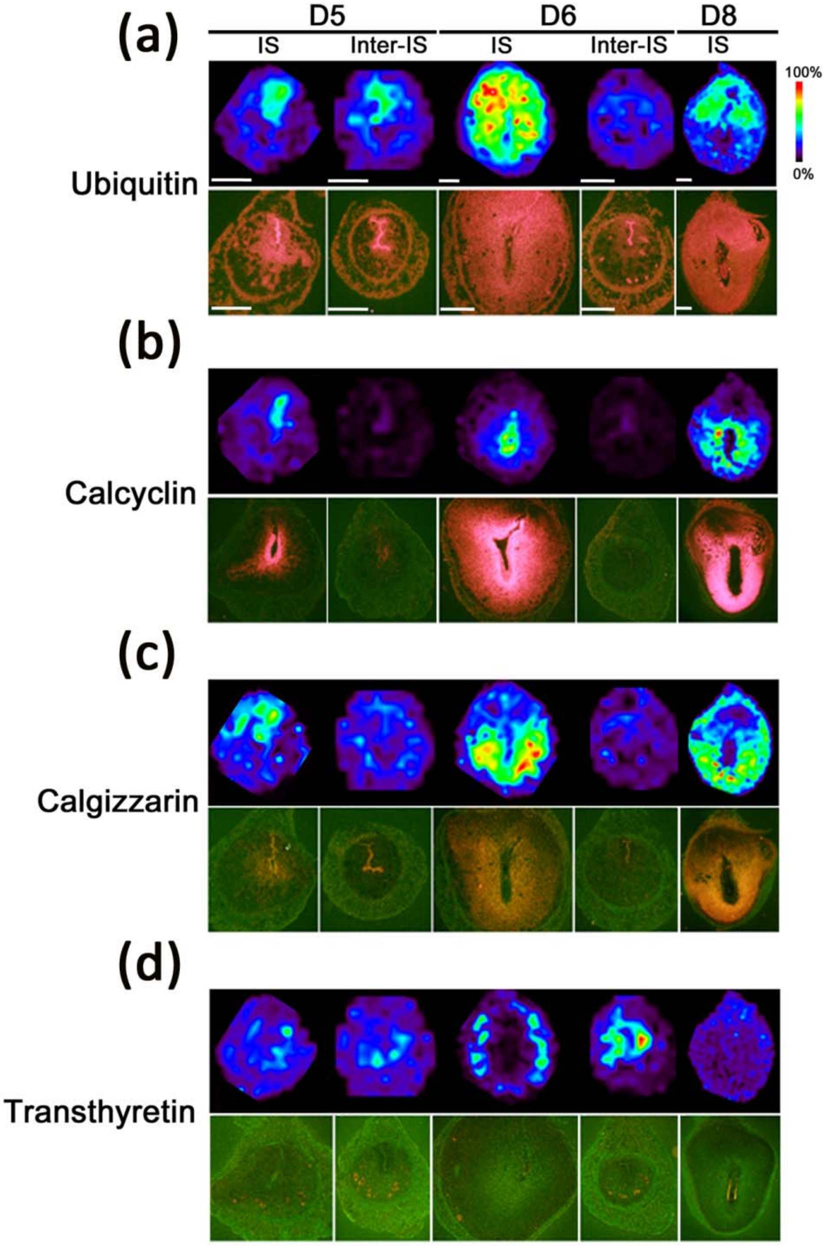

Figure 22. Comparing MS images with *in situ* hybridization for selected proteins / transcripts of interest on days 5, 6, and 8 of pregnancy (D5, D6 & D8). Spatial localization of **(a)** Ubiquitin, **(b)** Calcyclin, **(c)** Calgizzarin, and **(d)** Transthyretin by Imaging MS (upper) and respective mRNAs by in situ hybridization (lower). Abbreviation: Implantation site (IS) and interimplantation site (Inter-IS) labels. Bar, 700 µm.

Image adapted from: Burnum, K.E. et al. Journal of Endocrinology 149, 3274-3278 (2008)

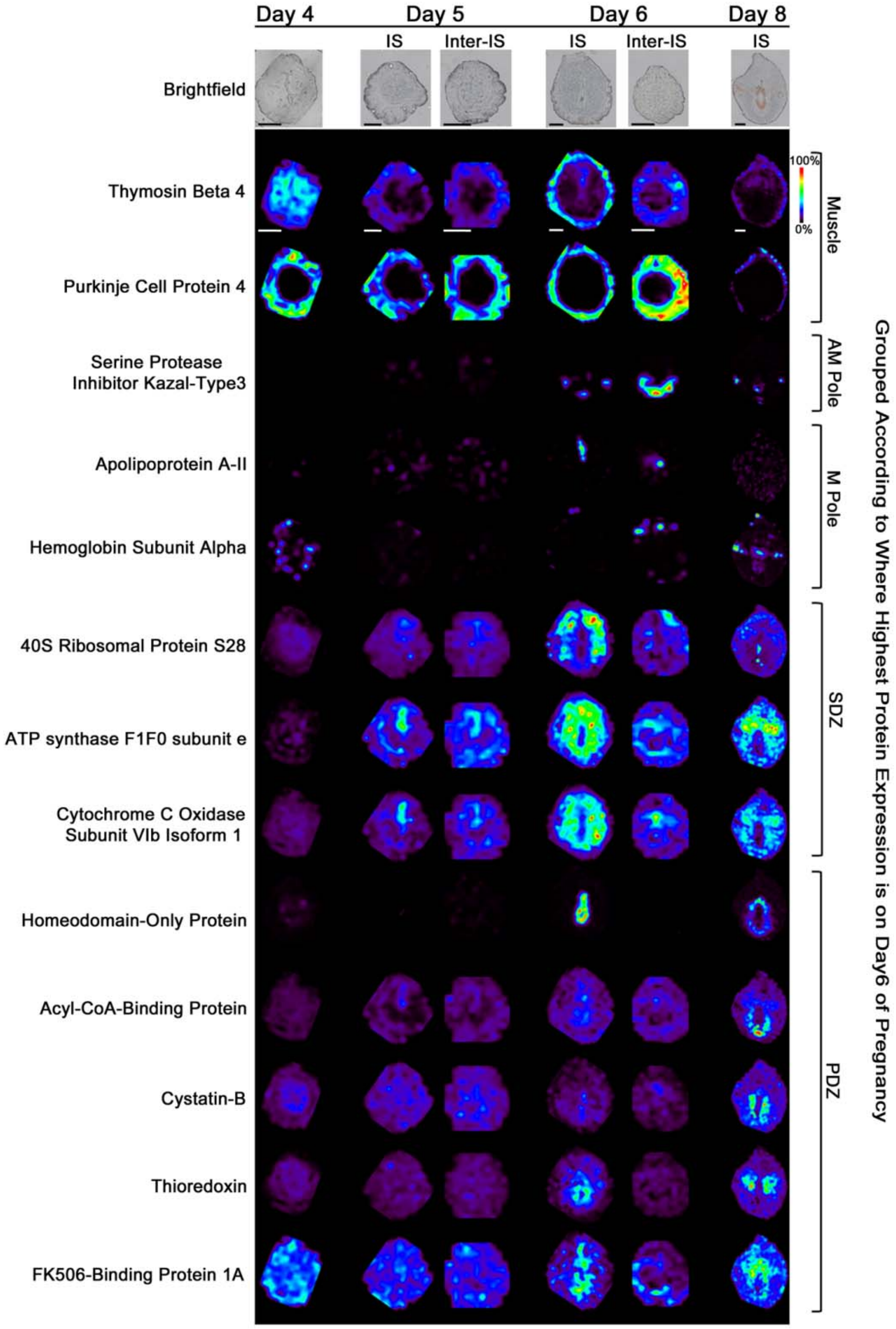

Figure 23. MALDI images of implantation sites (IS) and interimplantation sites (Inter-IS) on days 4, 5, 6 and 8 of pregnancy. MALDI images of selected proteins show differential proteome expression patterns between varying days of early pregnancy and between IS and Inter-IS. Bar, 700 μm.

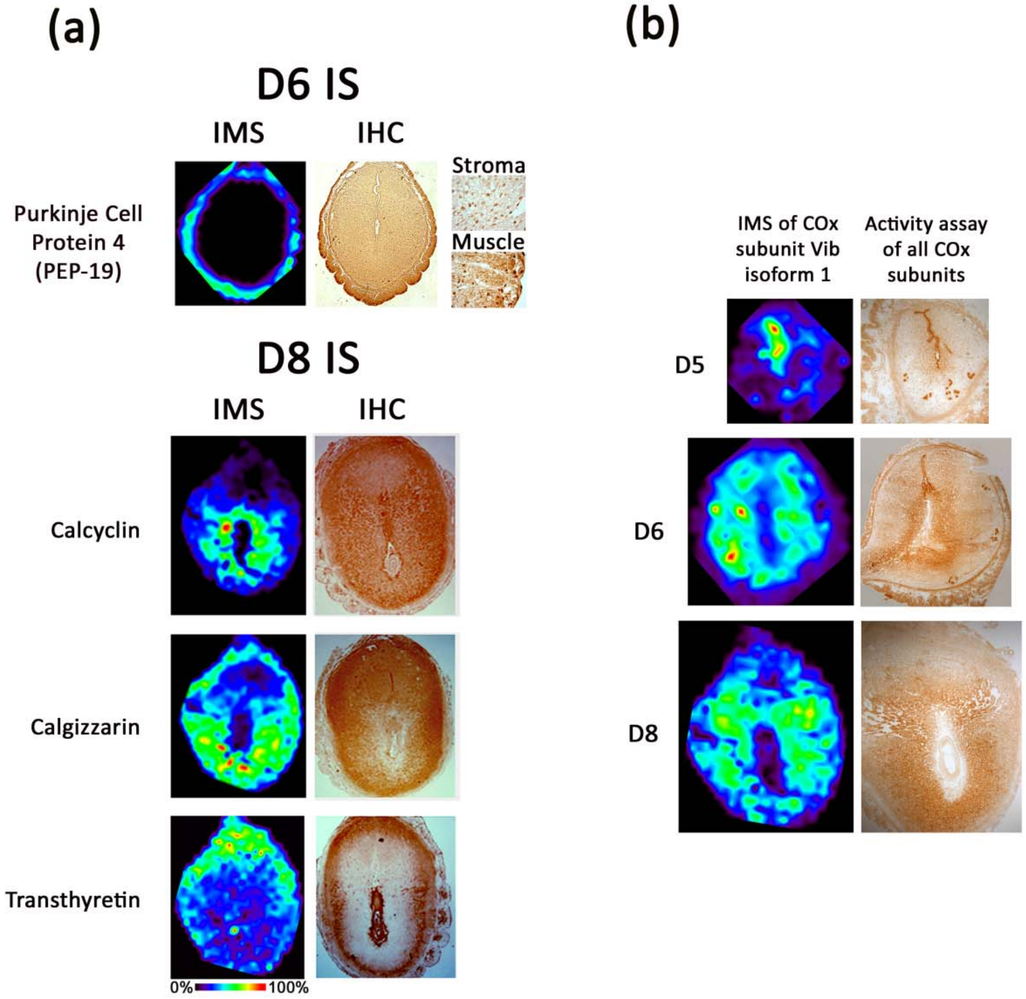

Figure 24. Verification of MALDI images (IMS) by Immunohistochemistry (IHC) (panel a) and Cytochrome C Oxidase (COx) Activity Assays (panel b) on day 5 (D5), day 6 (D6) and day 8 (D8) of pregnancy.

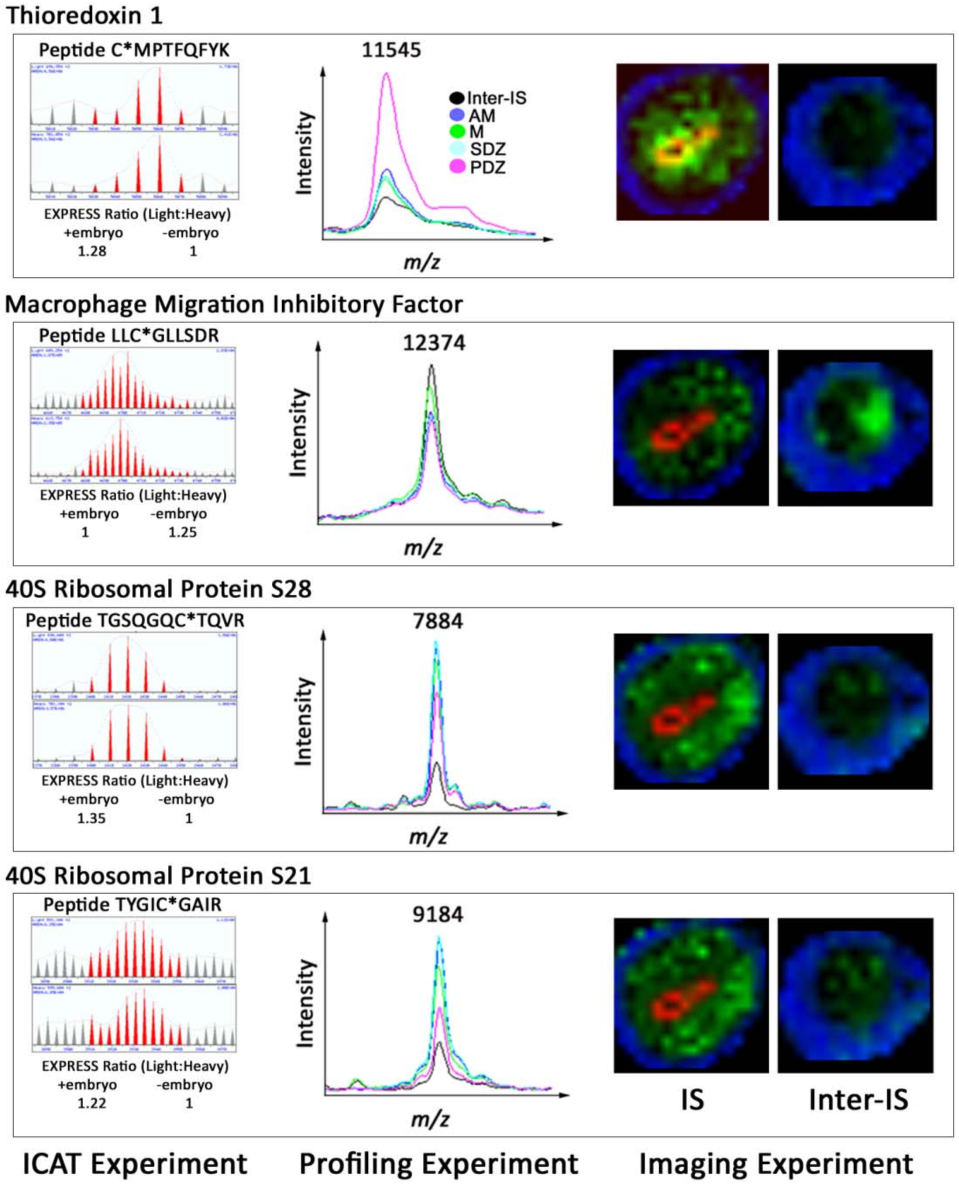

Figure 25. Verifying Imaging and Profiling MS experiments with ICAT. (Left) ICAT study, **(Middle)** profiling study, and **(Right)** IMS study. In the imaging experiment the red ion (*m/z* 8194) represents the embryo, the blue ion (*m/z* 6718) represents the muscle surrounding the uterus, and the green ion represents the ion of interest either thioredoxin 1 (*m/z* 11545), macrophage migration Inhibitory factor (*m/z* 12374), 40S ribosomal protein S28 (*m/z* 7884), or 40S ribosomal protein S21 (*m/z* 9184).

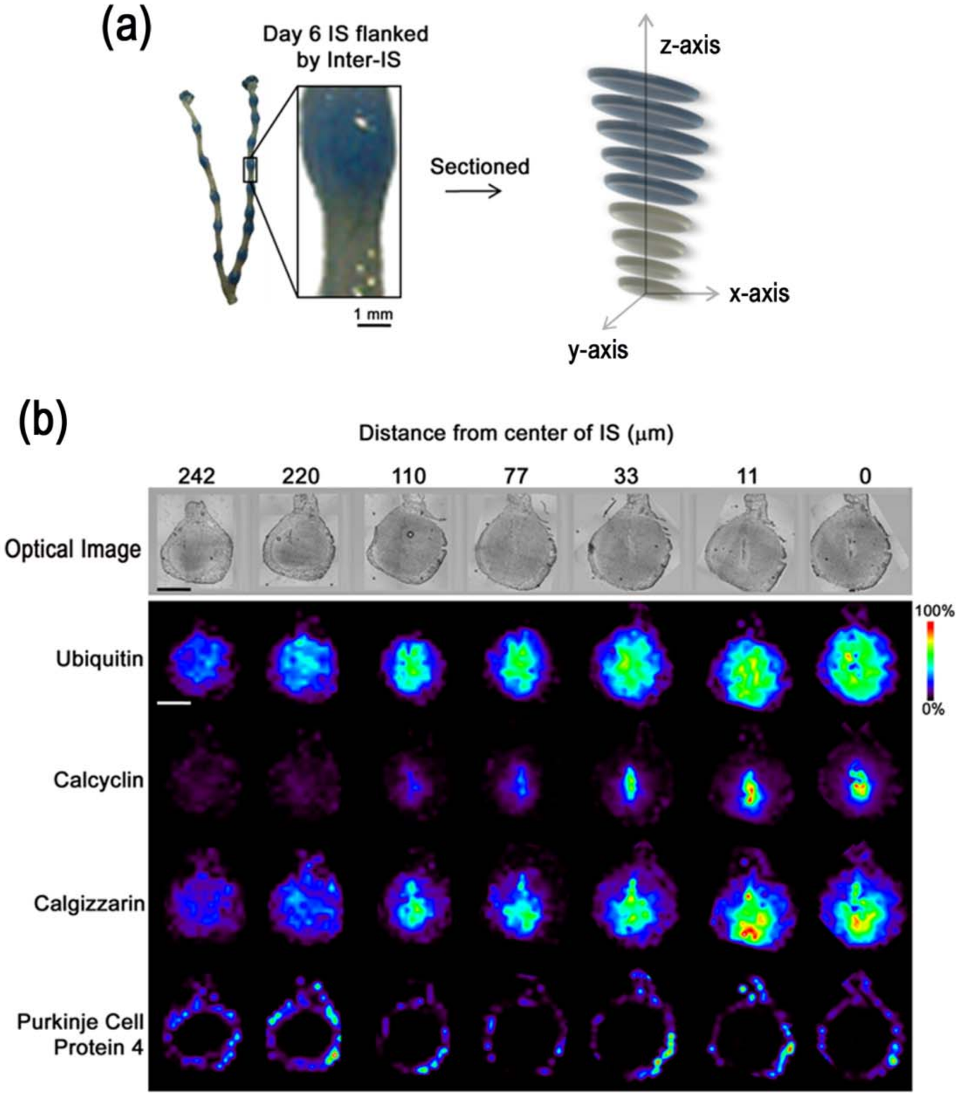

Figure 26. Relative protein expression changes along the Z-axis of a day 6 implantation site (IS). (a) Experimental Design: enlargement of a d6 IS flanked by interimplantation (Inter-IS) on bottom (left) and the resulting sections (right); Bar, 1 mm. **(b)** Imaging mass spectrometry shows differential protein localization depending on proximity to implanted embryo. Brightfield images of serial sections of an implantation site collected on day 6 of pregnancy (upper). Ion intensity maps of Ubiquitin, Calcyclin, Calgizzarin, and Purkinje cell protein 4 are shown underneath respective brightfield images.

Image adapted from: Burnum, K.E. et al. Journal of Endocrinology 149, 3274-3278 (2008)

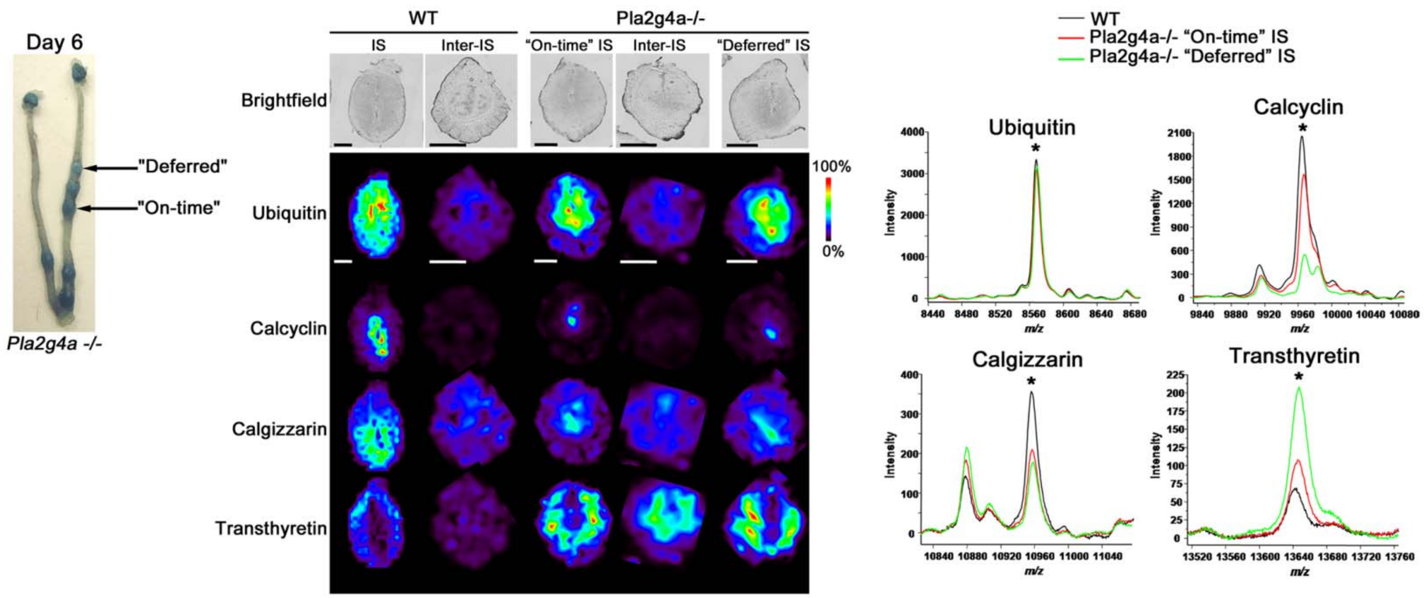

Figure 27. Proteome profiles defer between wild-type and Pla2g4a null uteri on day 6 of pregnancy regardless of implantation timing. (Left) Representative photograph of Pla2g4a null uterus collected on day 6 of pregnancy. Notice smaller 'deferred' IS and larger 'on-time' IS. **(Middle)** Optical images of a wild-type (WT) IS and Inter-IS and Pla2g4a null (-/-) "deferred" IS and "on-time" IS (upper); Bar, 670 µm. Corresponding ion intensity maps for Ubiquitin, Calcyclin, Calgizzarin and Transthyretin are shown below respective brightfield images. **(Right)** Average mass spectra obtained from day 6 uterine sections. *, peak, m/z protein of interest.

Image adapted from: Burnum, K.E. et al. Journal of Endocrinology 149, 3274-3278 (2008)

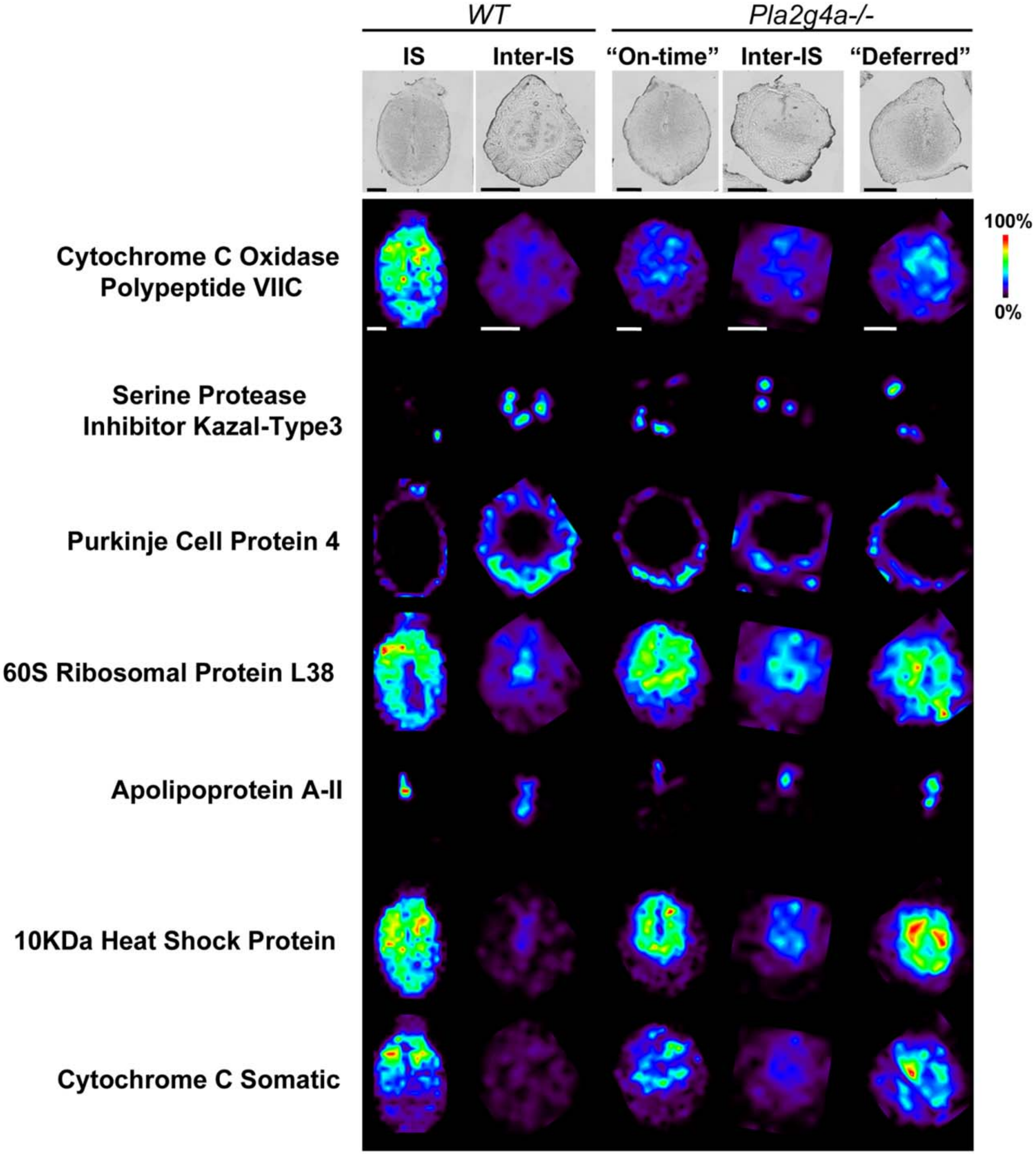

Figure 28. MALDI images of a wild-type (WT) IS and Inter-IS and Pla2g4a null (-/-) "deferred" IS, "on-time" IS and Inter-IS. (Top) Optical images, (bottom) corresponding ion intensity maps for selected proteins which show differential proteome expression patterns between WT and Pla2g4a null (-/-) IS. Bar, 670 μm.

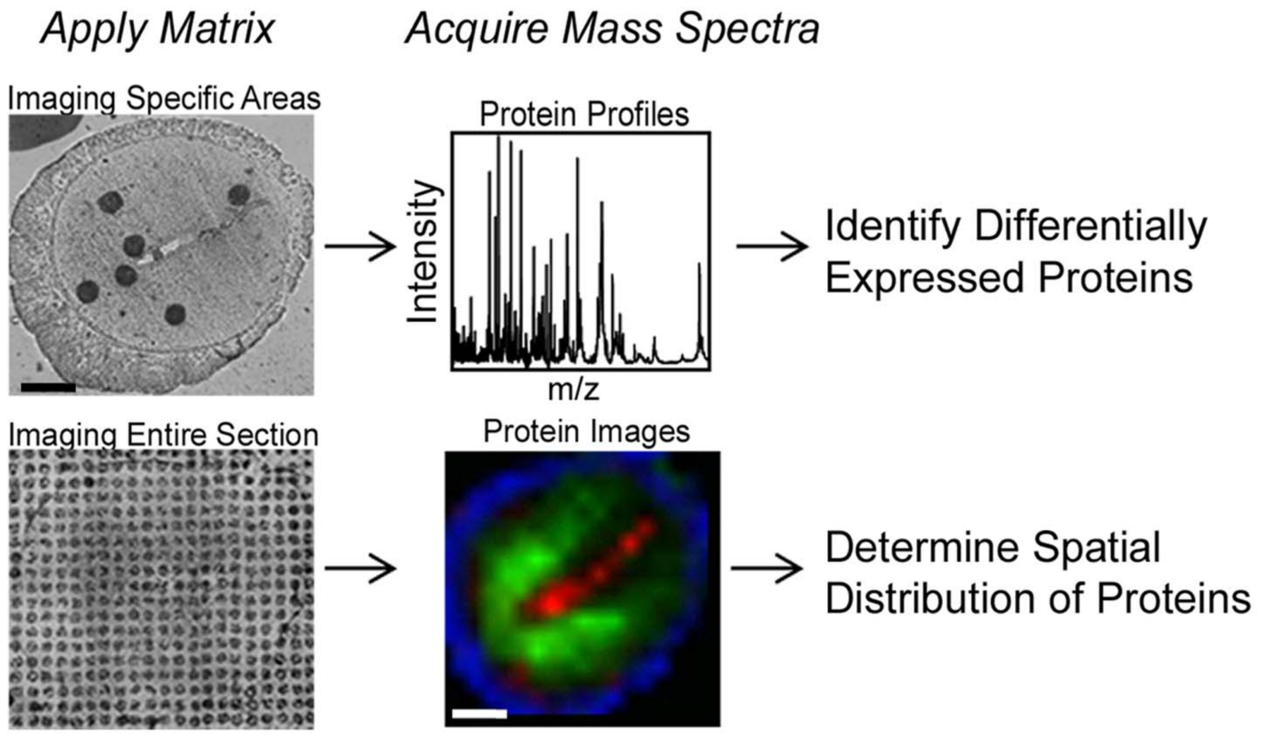

Figure 29. Experimental Design: Frozen uterine sections (11 μm) were thaw mounted on a MALDI glass plate and subjected to profiling or imaging analysis as shown. Resulting mass spectra from profiling (upper) were baseline corrected, normalized, and realigned. Statistical analysis highlights m/z values showing differential expression, and corresponding proteins were identified. Imaging (lower) creates a two-dimensionalintensity map for the m/z values of interest. Bar, 700 μm.

Image adapted from: Burnum, K.E. et al. Journal of Endocrinology 149, 3274-3278 (2008)

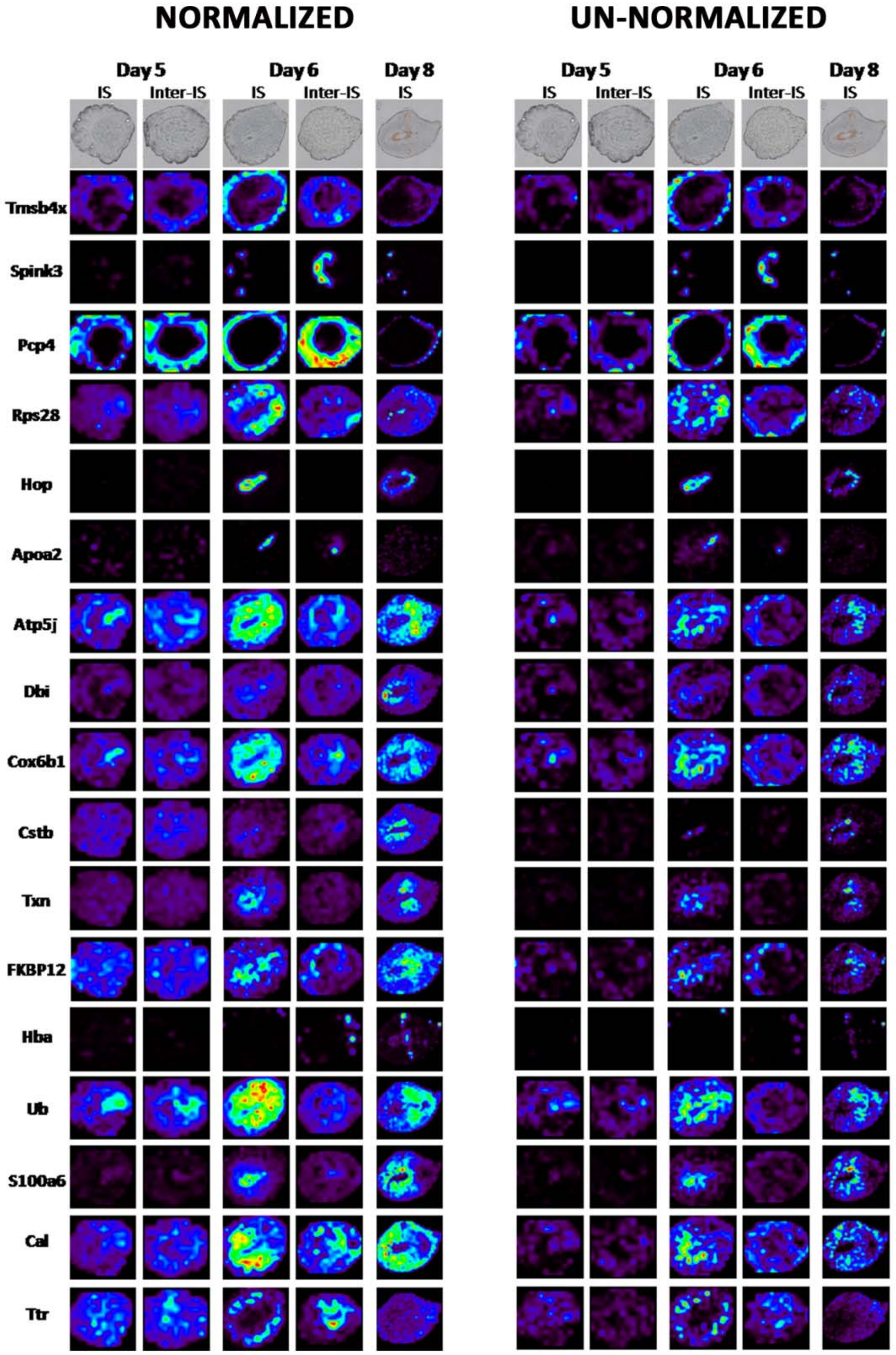

Figure 30. Comparing normalized images to un-normalized images.

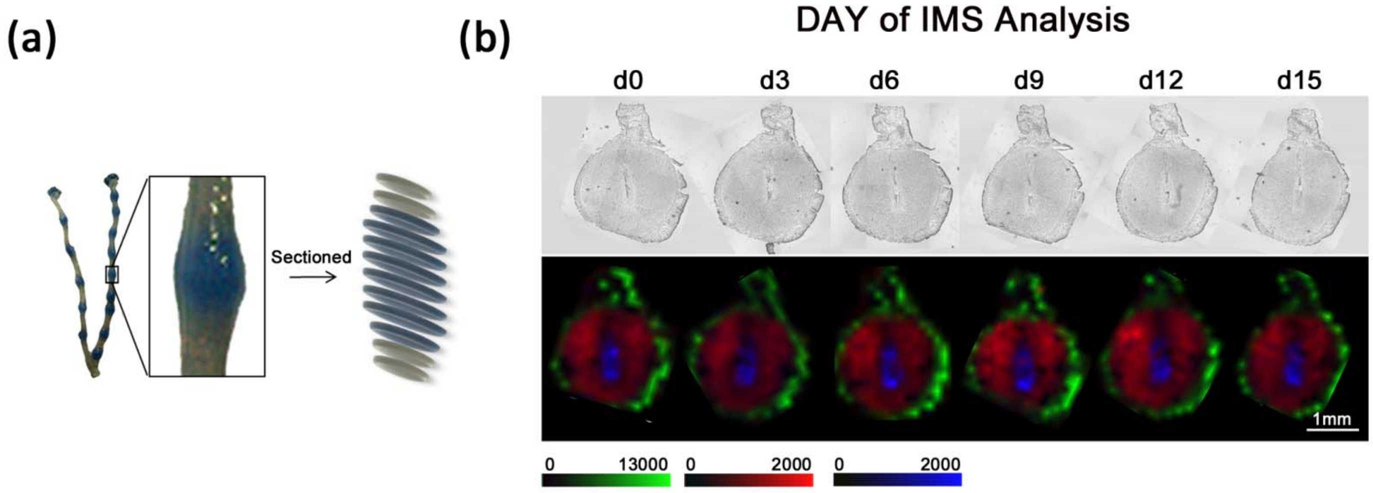

Figure 31. Reproducibility of MALDI IMS analysis of embryo implantation in the mouse uterus on day 6 of pregnancy after total ion current normalization. (a) This picture shows a mouse uterus on day 6 of pregnancy and an enlargement of the implantation site which was sectioned. **(b)** The optical images of the 6 serial center sections (top) with corresponding MALDI images (bottom) are shown. The day of analysis is listed above the optical images. Each of these sections contains part of the embryo. The impressive aspect of this picture is we can see the symmetry of the embryo (represented by homeodomain-only protein in blue) in these images. (green = 6718 [pep19], red = 7884 [40S ribosomal protein S28], blue = 8194 [homeodomain-only protein]).

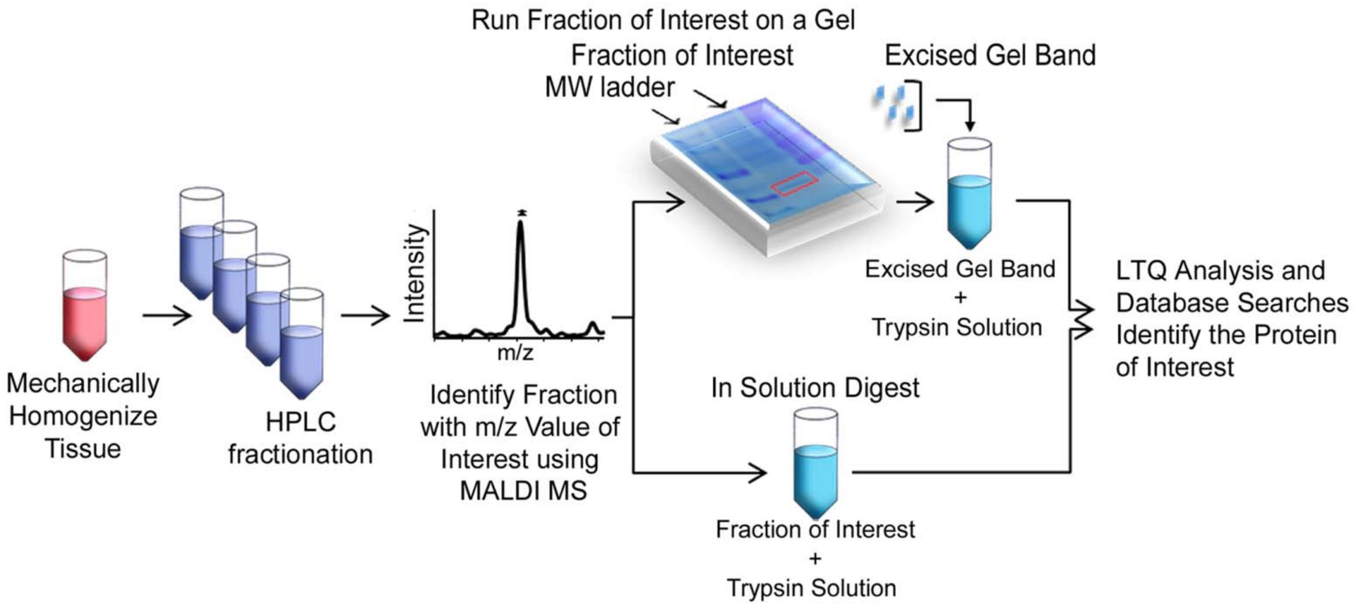

Figure 32. Protein Identification. Proteins corresponding to m/z values of interest were identified from tissue extracts and fractionated with a reversed-phase column. Fractions containing m/z values of differentially expressed proteins were either digested with trypsin or run on a 1D gel, and bands of interest were digested. Proteins were then identified using a linear ion trap (LTQ) and database searches.

Image adapted from: Burnum, K.E. et al. Journal of Endocrinology 149, 3274-3278 (2008)

Table 4. Proteins which also show differential expression patterns between the various cell types on day 6 of pregnancy are listed.

MW (Da)	Protein Name	% coverage of unprocessed precursor	Modifications (amino acid chain)	Swissprot Primary Accession Number	TPP	Cellular Region with High Expression	Primary Functions and Processes of the Protein
Proteins Expressed in the Muscle							
4964	Thymosin Beta 4	38	* (8 - 50)	P20065	0.88	**Muscle and M pole '**	Cytoskeleton organization, Regulation of cell migration
6718	Purkinje cell protein 4	44.3	* (2 - 62)	P63054	1	**Muscle '**	Calcium ion binding
7413	Purkinje cell like protein 4 - like 1	60.3	* (2 - 68)	Q6W8Q3	1	**Muscle '**	
Proteins Expressed in the Anti-Mesometrial Pole							
6120	Serine Protease inhibitor Kazal-type 3	56.2	(3 disulfide) (24 - 80)	P09036	1	**AM**	Serine-type endopeptidase inhibitor activity, Endopeptidase inhibitor activity
10951	Calgizzarin	37.8	(2 - 98)	P50543	1	**AM and PDZ**	Cytokine activity, Calcium ion binding
Proteins Expressed in the Mesometrial Pole							
8906	Apolipoprotein AII	51	* (24 - 102)	P09813	1	**M**	Lipid binding and transport
12131	Cytochrome C somatic	41.9	*, # (2 - 105)	P62897	1	**M**	Positive regulation of apoptosis
12373	Macrophage migration inhibitory factor	36	(2 - 115)	P34884	1	**M**	Inflammatory response
14954	Hemoglobin alpha chain	62.7	(2 - 142)	P01942	1	**M '**	Oxygen transport
15709	hemoglobin beta chain 1	97.3	(2 - 147)	P02088	1	**M'**	Oxygen transport
15747	hemoglobin beta chain 2	96.6	(2 - 147)	P02089	1	**M'**	Oxygen transport
Proteins Expressed in the Secondary Decidual Zone							
6546	40S ribosomal protein S29	18.8	(2-56)	P62274	1	**SDZ**	Translation
7883	40S ribosomal protein S28	13	* (1 - 69)	P62858	1	**SDZ**	Translation
8073	60S ribosomal protein L38	50	(2 - 70)	Q9JJI8	1	**SDZ**	Translation
8105	ATP synthase F1F0 subunit e	61.4	(2-71)	Q5EBI8	1	**SDZ**	ATP synthesis coupled proton transport
8945	ATP synthase Coupling Factor 6	40.7	(33 - 108)	P97450	1	**SDZ**	ATP synthesis coupled proton transport
9183	40S Ribosomal Protein S21	39.8	* (1 - 83)	Q9CQR2	1	**SDZ**	Translation
9982	Cytochrome c oxidase subunit Vib isoform 1	41.2	* (2 - 86)	P56391	1	**SDZ**	Electron transport
10873	10KDa heat shock protein	67.6	* (2 - 102)	Q64433	1	**SDZ**	Protein folding
11811	60S acidic ribosomal protein P2	84.3	$S^{17\wedge}$,$S^{102\wedge}$ (1-115)	P99027	1	**SDZ**	Translation
13640	Transthyretin	61.9	(21 - 147)	P07309	1	**SDZ and AM**	Thyroid hormone generation, Transport

***acetylated N-terminus (+42 Da), ^Phosphorylation (+80 Da), # heme group (+615 Da),**

‘muscle localization was determined by IMS not statistical analysis

TTP: Trans-Proteomic Pipeline probability score

Table 4 (Continued). Proteins which also show differential expression patterns between the various cell types on day 6 of pregnancy are listed.

MW (Da)	Protein Name	% coverage of unprocessed precursor	Modifications (amino acid chain)	Swissprot Primary Accession Number	TPP	Cellular Region with High Expression	Primary Functions and Processes of the Protein

Proteins Expressed in the Primary Decidual Zone

6157	Metallothionein-2	13.1	* (1-61)	P02798	1	**PDZ**	Cellular zinc ion homeostasis, Detoxification of copper ion, Nitric oxide mediated signal transduction
8193	Homeodomain only protein	31.9	* (2-73)	Q8R1H0	1	**PDZ**	Regulation of transcription
9911	Acyl CoA binding protein	46	* (2 - 87)	P31786	1	**PDZ**	Transport
9961	Calcyclin	67.4	* (2 - 89)	P14069	1	**PDZ**	Cell cycle, Cell proliferation, Regulation of progression through cell cycle
11088	Cystatin B	56.1	* (1 - 98)	Q62426	1	**PDZ**	Cysteine protease inhibitor activity, Endopeptidase inhibitor activity, Protease binding
11544	Thioredoxin 1	56.2	(2 - 105)	P10639	1	**PDZ**	Cell redox homeostasis
11791	FK 506-binding protein 1A	29.6	(2 - 108)	P26883	1	**PDZ**	Isomerase activity, Protein folding, Transport

Proteins Expressed throughout the Implantation Site

6653	Cytochrome C oxidase copper chaperone	25.8	(2 - 63)	P56394	0.99	**IS**	Copper chaperone activity
8565	Ubiquitin	91.8	(24 - 102)	P62991	1	**IS**	Protein degeradation

Proteins Expressed throughout the Interimplantation Site

11347	Histone H4	57.7		P62806	1	**Inter-IS**	Nucleosome assembly
13804	Histone H2B	24.6		Q9FFC0	1	**Inter-IS and SDZ**	Nucleosome assembly
14006 14047	Histone H2A2	27.1		Q6GSS7	1	**Inter-IS and SDZ**	Nucleosome assembly

Proteins not Expressed in specific regions

6088	Probable Mitochondrial Import Receptor Subunit TOM7 Homolog	30.9	* (2 - 55)	Q9D173	1		Transport
6573	Cytochrome C oxidase polypeptide VIIA	12	(24-83)	P48771	0.97		Electron transport
7207	Copper Transport Protein ATOX1	58.8	(2 - 68)	O08997	1		Copper transport
10901	Dynein Cytoplasmic light chain 2a	73.7	* (2 - 96)	P62627	1		Microtubule-based movement, Small GTPase mediated signal transduction
11055	Calpactin 1 light chain	27.8	(2 - 97)	P08207	1		Regulation of cell differentiation, Regulation of cell growth
11687	Beta-2 microglobulin	35	(21 - 119)	P01887	1		Immune response, Antigen processing and presentation of peptide antigen via MHC class I
12165	Prothymosin alpha	22.7	(2 - 111)	P26350	1		Immune response
12772	Myotrophin	25.6	* (2 - 118)	P62774	1		Protein binding
14777	Lectin galactose binding soluble 1	61.5	* (2 - 135)	P16045	1		Cell adhesion

***acetylated N-terminus (+42 Da)**

TTP: Trans-Proteomic Pipeline probability score

CHAPTER V

CONCLUSIONS AND PERSPECTIVES

A. Discussion of protein and phospholipid localization patterns during early pregnancy

This study found that small structural changes in phospholipids have a huge impact on their spatial distribution across implantation sites and, as a result, their biological activity. In addition, proteins important to biological processes of embryo implantation are highly regionalized and take place in very discrete time domains. In **Figures 33 – 41** protein and phospholipid images are categorized according to their expression patterns on different days of embryo implantation. Proteins with increased expression levels on day 4 of pregnancy include actin sequestering proteins, thymosin β4 and β10, which plays roles in regulation of actin polymerization (**Figure 33**). These proteins are known to be involved in cell proliferation, migration, and differentiation, all cellular processes which play important roles in priming the receptive uterus. In day 4 implantation sites most phospholipids show an intensity increase in the lumen (**Figure 34**). An exception is PC 32:0 which localizes to the uterine stroma; this phospholipid shows an inverse localization pattern in comparison to the other phospholipids throughout embryo implantation. Proteins with increased expression in the luminal epithelial cells on day 5 of pregnancy; such as, ATP synthase F1F0 subunit e, and cytochrome c oxidase subunit VIb isoform 1 play a role in energy production

(**Figure 35**). In day 5 implantation sites most phospholipids show an intensity increase in the uterine stroma immediately surrounding the implanting embryo (**Figure 36**). Proteins implicated in hormone signaling and proliferating localize to the PDZ and SDZ of day 6 implantation sites, respectively (**Figure 37**). On day 6 of implantation most of the phospholipids showed an intensity increase in the PDZ (**Figure 38**). Some of these phospholipids are starting to localize to the M pole (PC 34:1 [16:0/18:1] and PI 38:5 [18:1/20:4]), whereas others are localizing to the AM pole (PC 36:2 [18:0/18:2] and PC 36:4 [16:0/20:4]). Proteins that show the highest intensity on day 8 of pregnancy, such as, cystatin B and acyl CoA binding protein localize to embryo and are implicated in embryo survival (**Figure 39**). On day 8 of pregnancy, phospholipids localized to either the M pole or AM pole of the implantation sites (**Figure 40**). Oleate (18:1) containing phospholipids and arachidonate (20:4) containing PEs and PIs localize to the M pole. Linoleate (18:2) and docosahexaenoate (22:6) containing phospholipids and arachidonate (20:4) containing PCs localize to the AM pole. Strikingly, MALDI images of 18:1 (PC 34:1, PC 36:1 and PS 36:1) and 18:2 (PC 34:2, PC 36:2 and PS 36:2) containing phospholipids show that they localize to completely different hemispheres of the day 8 implantation sites, yet the only structural change between these phospholipids is one double bond in the sn2 fatty acid chain. Potential angiogenic and apoptotic roles for phospholipids in the M and AM poles of day 8 implantation sites are discussed in the following section. Purkinje cell protein 4 (PEP-19) and purkinje cell protein 4 like 1 proteins show constant expression during the implantation process because they localize the muscle layer encircling the uterine stroma, which is unaffected by the decidualization process resulting from the presence of the embryo (**Figure 41**).

Figures 33 – 41 also show the unparalleled ability of MALDI IMS to spatially resolve posttranslational modified proteins form their intact forms. Figure 35 depicts a truncated form of ubiquitin which is missing two c-terminal glycines (G) (**Figure 35**). This modified ubiquitin has been characterized in many different pathological and physiological biological processes [139]. Posttranslational modified forms of apolipoprotein A-II, missing its c-terminal lysine (K), and serine protease inhibitor kazal-type3, missing its n-terminal alanine (A) and K were also detected by imaging MS (**Figure 37**).

Based on our studies discussed in chapter IV, it was known that proteins can also show expression/distribution patterns in the M and AM poles on day 8 of pregnancy, similar to that seen in the lipid images in this study [113]. To explore this further, protein images of a day 8 implantation site were generated that showed high expression levels in either the M or AM pole (**Figure 42**). In **Figure 39**, ATP synthase coupling factor 6, thymosin β4, FK506-binding protein 1A, and macrophage migration inhibitory factor localized to the M pole. These proteins have been shown to play important roles in angiogenesis [140-144]. Calgizzarin and calcyclin localized to the uterine cells in the AM pole, whereas, homeodomain only protein, and cystatin B localize to the embryo in the AM pole. The edge of the embryo is depicted by homeodomain-only protein that is expressed in embryonic trophoblast cells[145]. This is consistent with other data that show calgizzarin and calcyclin to be important in cell apoptosis, while cystatin B prevents apoptosis [146, 147]. In summary, with respect to proteins, images on day 8 of pregnancy revealed an increased level of proteins involved in angiogenesis at the uterine stroma at the M pole and those involved in apoptosis to the uterine stroma in the AM pole. This is consistent with known biology, on day 8 of pregnancy where cells at the M pole are preparing for rapid development of the placenta by initiating angiogenesis; cells at the AM pole are preparing for embryo growth by undergoing apoptosis.

In summary, this work focuses on technology that provides both spatial and temporal molecular analyses in the elucidation of critical events in the reproductive process. Here for the first time, we use Imaging Mass Spectrometry to elucidate the spatial patterning of lipids and proteins during embryo implantation and demonstrate its value in helping to understand fertility and the reproductive process. For example, our analysis clearly shows previously unknown molecular distributions of lipids over time in this system. Beyond this example, we think that the approach and the concepts illustrated in this work will be of enormous value in various areas of biology and will be critical for understanding many biological processes.

Implantation is an incredibly important biological process, a better understanding of which will advance our knowledge in several basic physiological processes. For example, several reports have noted an interesting parallel between implantation and cancer in that many cellular processes such as tissue invasion, replicative potential, and angiogenesis, which are required during implantation, are also important during tumorigenesis [1, 48, 148]. During embryo implantation the tissue microenvironment has the ability to tightly regulate these events, while dysregulation of these events may lead to cancer. Some of the phospholipids analyzed in this study are known to play important roles in cancer proliferation, survival and migration. It has previously been reported that in cancer linoleate can promote cancer cell growth [149], whereas, docosahexaenoate has been shown to inhibit cancer cell growth by preventing neovascularization [146, 150]. Understanding the molecular events driving cellular transformations during embryo implantation may shed light on similar processes occurring in other biological processes involving cell proliferation.

B. Future Outlook: Advancements in IMS

IMS continues to advance at an accelerating rate moving toward higher spatial resolution and wider applicability. The size of the focused MALDI laser beam, matrix spots in an array, and matrix crystal size in a sprayed or spotted matrix coating, all determine the lateral image resolution (surface area mapped by a single pixel) in an IMS experiment. Therefore, IMS analysis of individual cells is at present a laborious endeavor. As the technology advances, submicron dimension of both the laser and matrix crystals will enable IMS experiments to explore subcellular molecular compositions.

The molecular complexity of biological systems obviates the need for molecularly specific tools to elucidate proteomic events in both spatial and temporal distributions. Parallel analysis of hundreds of molecular species by IMS without the need for target-specific reagents such as florescence tags or antibodies provides investigators with a unique tool for studying pathological and physiological biological processes. Moreover, this technology appeals to the human intellect and to our ability to understand complexity in a visual format. With continued developments in the field, IMS can become even more comprehensive and powerful with the potential to become an important and routine analysis for clinical, pharmaceutical and laboratory practice.

Furthermore, the massive amount of information produced by new technologies, such as, MALDI IMS, has ushered in a new era where instead of identifying individual biomolecules and studying their specific function, researchers hope to understand how these biomolecules function in context of the integrated system. Organisms are not static systems; they are integrated and interacting networks of genes, gene transcripts, proteins, lipids and biochemical reactions. IMS is a powerful tool for systems biology applications since it has the ability to analyze each of these networks; thereby, providing insight into highly structured but incredibly complex ways these molecules interact.

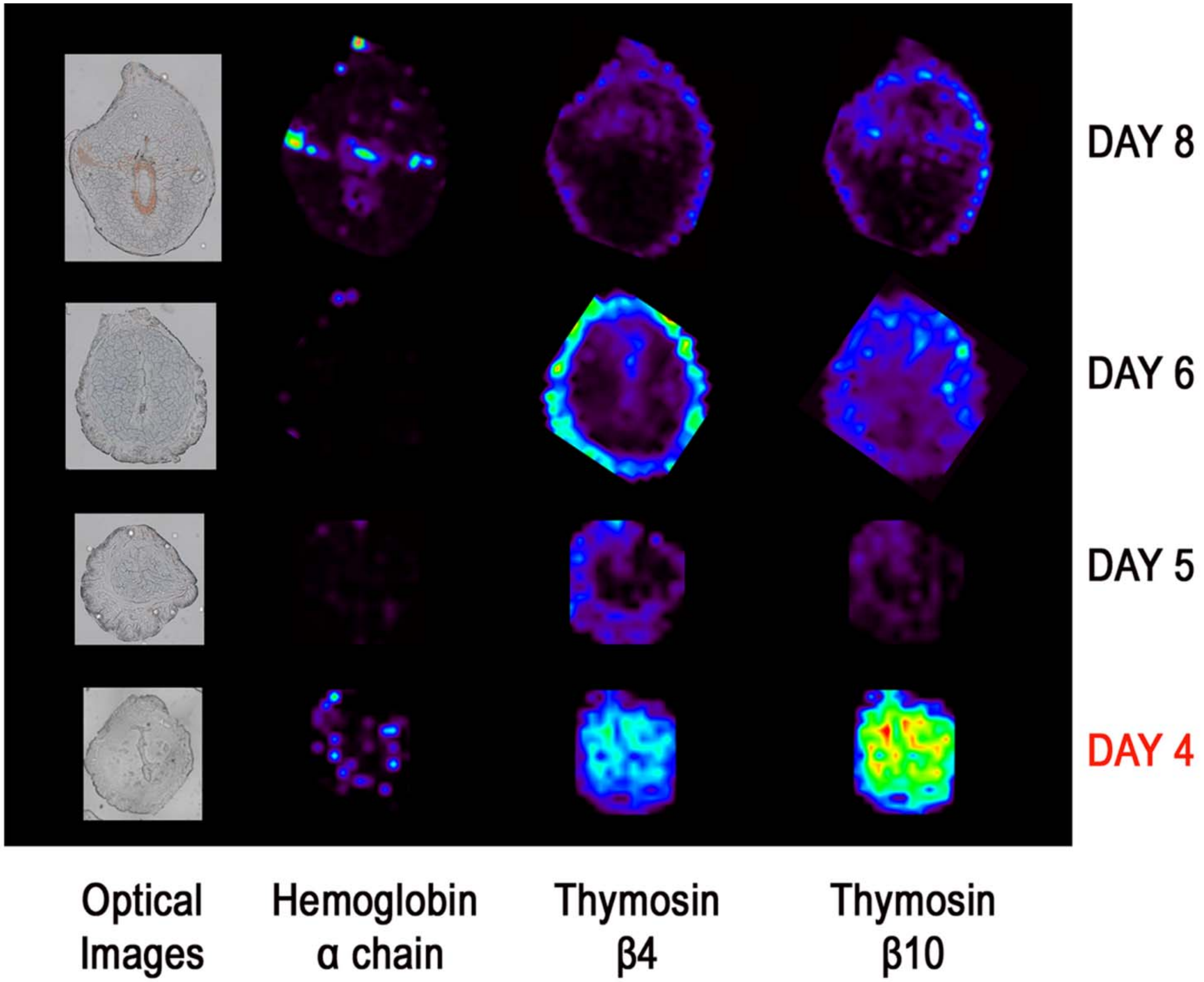

Figure 33. Proteins that show highest expression levels on Day 4 of Pregnancy

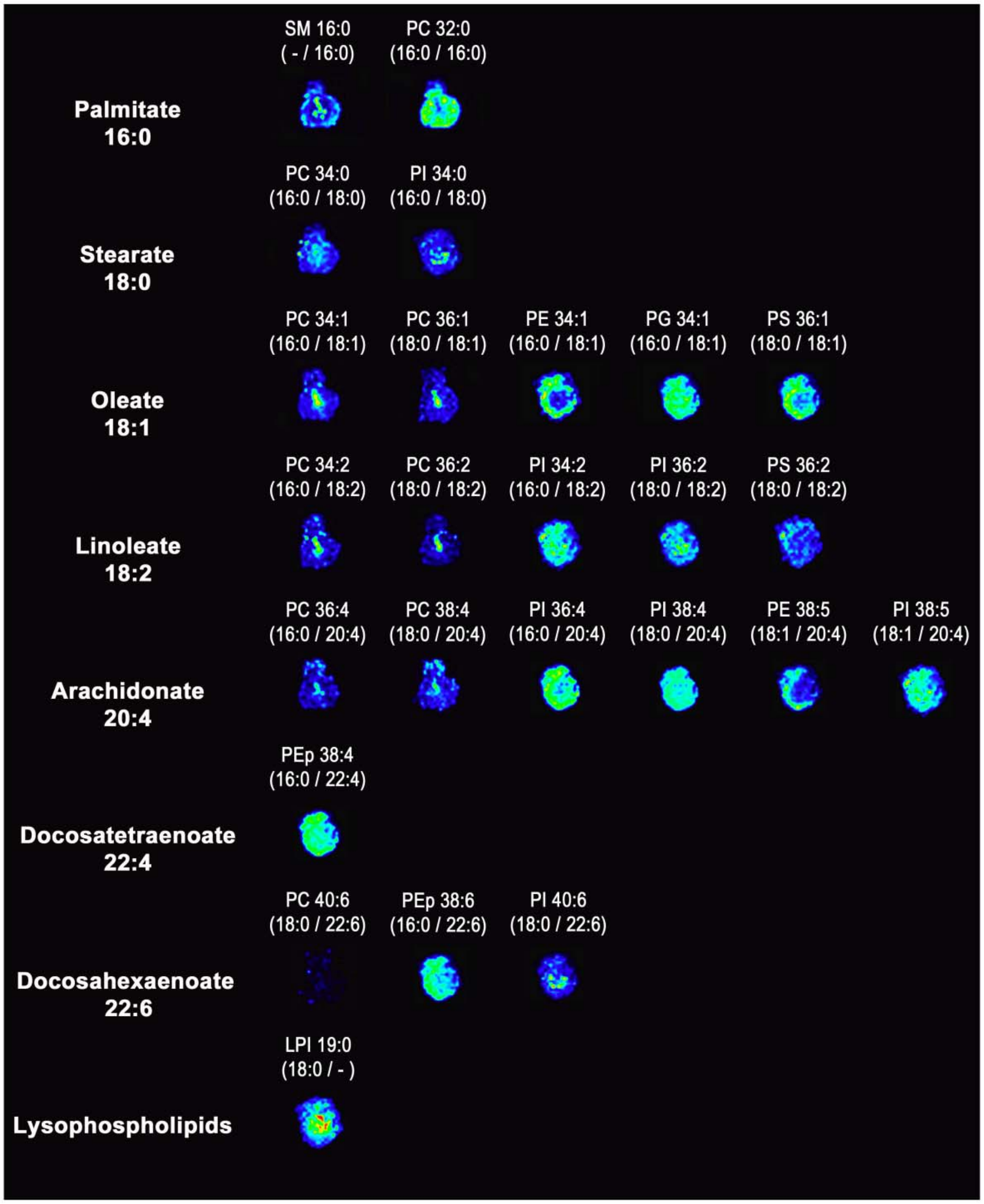

Figure 34. Phospholipid Expression on Day 4 of Pregnancy

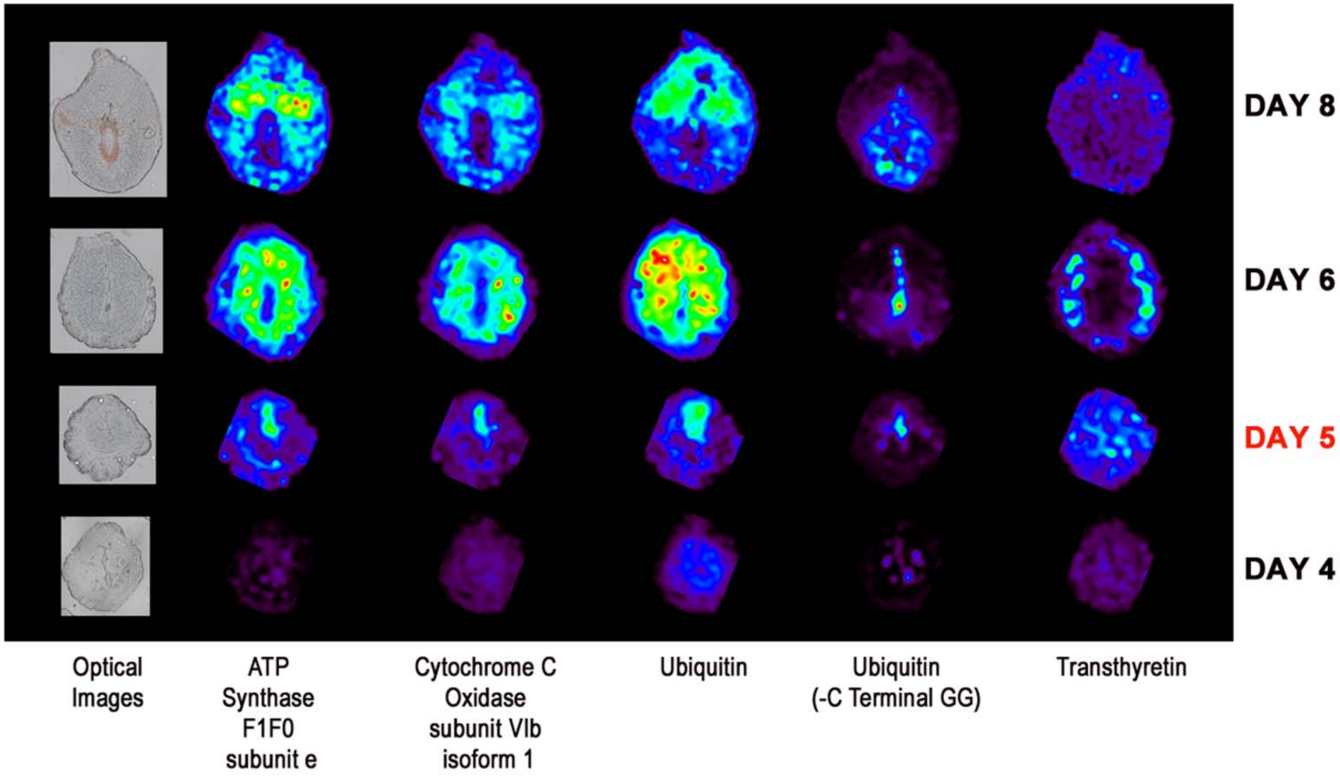

Figure 35. Proteins that show highest expression levels on Day 5 of Pregnancy

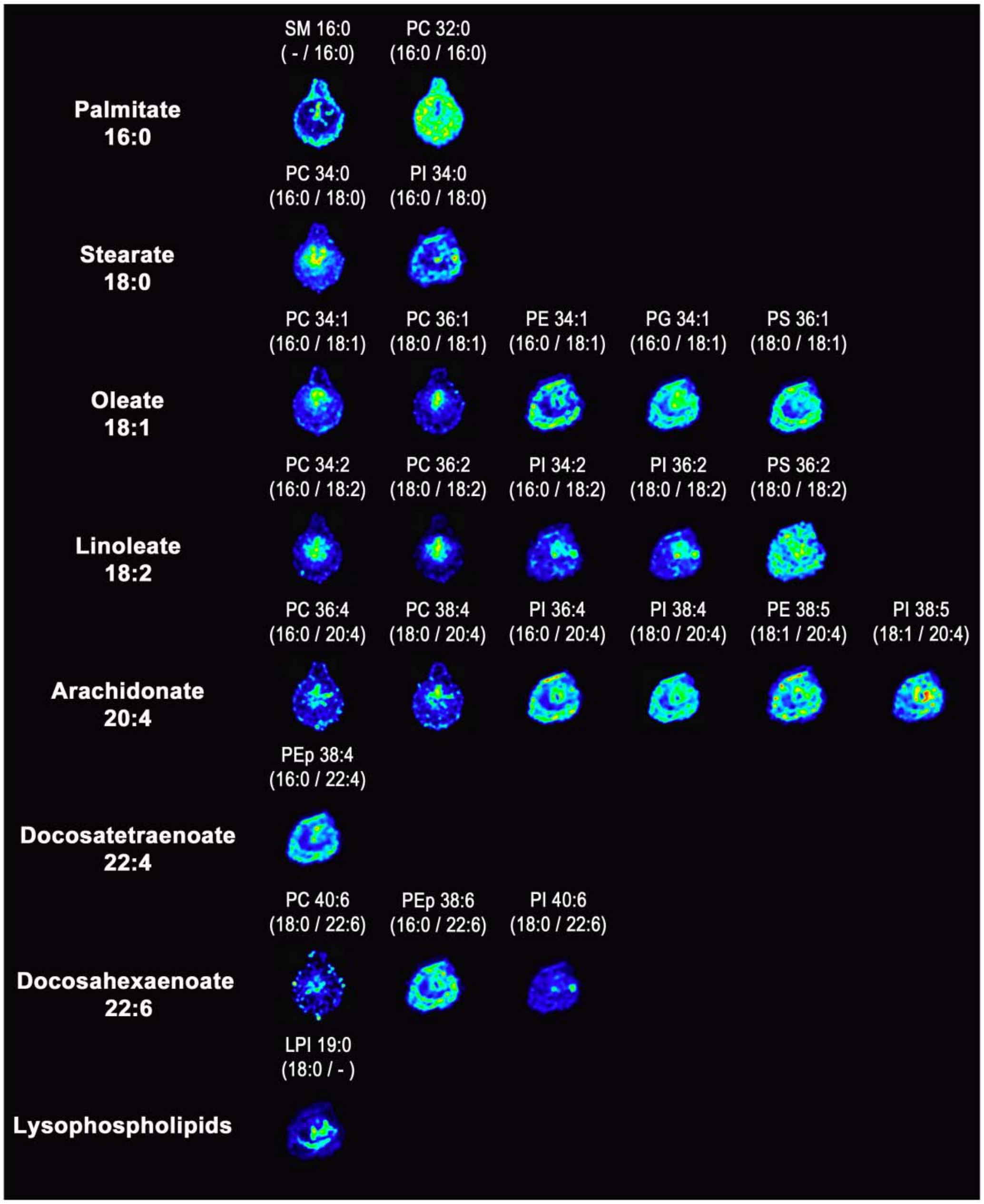

Figure 36. Phospholipid Expression on Day 5 of Pregnancy

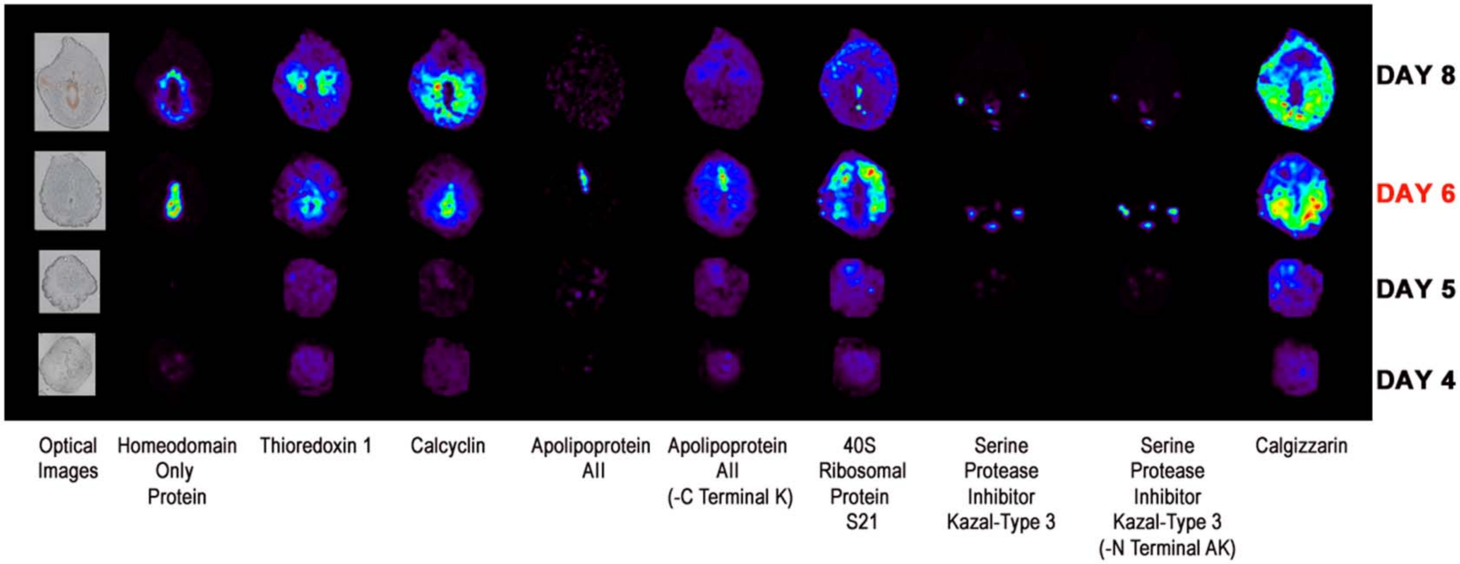

Figure 37. Proteins that show highest expression levels on Day 6 of Pregnancy

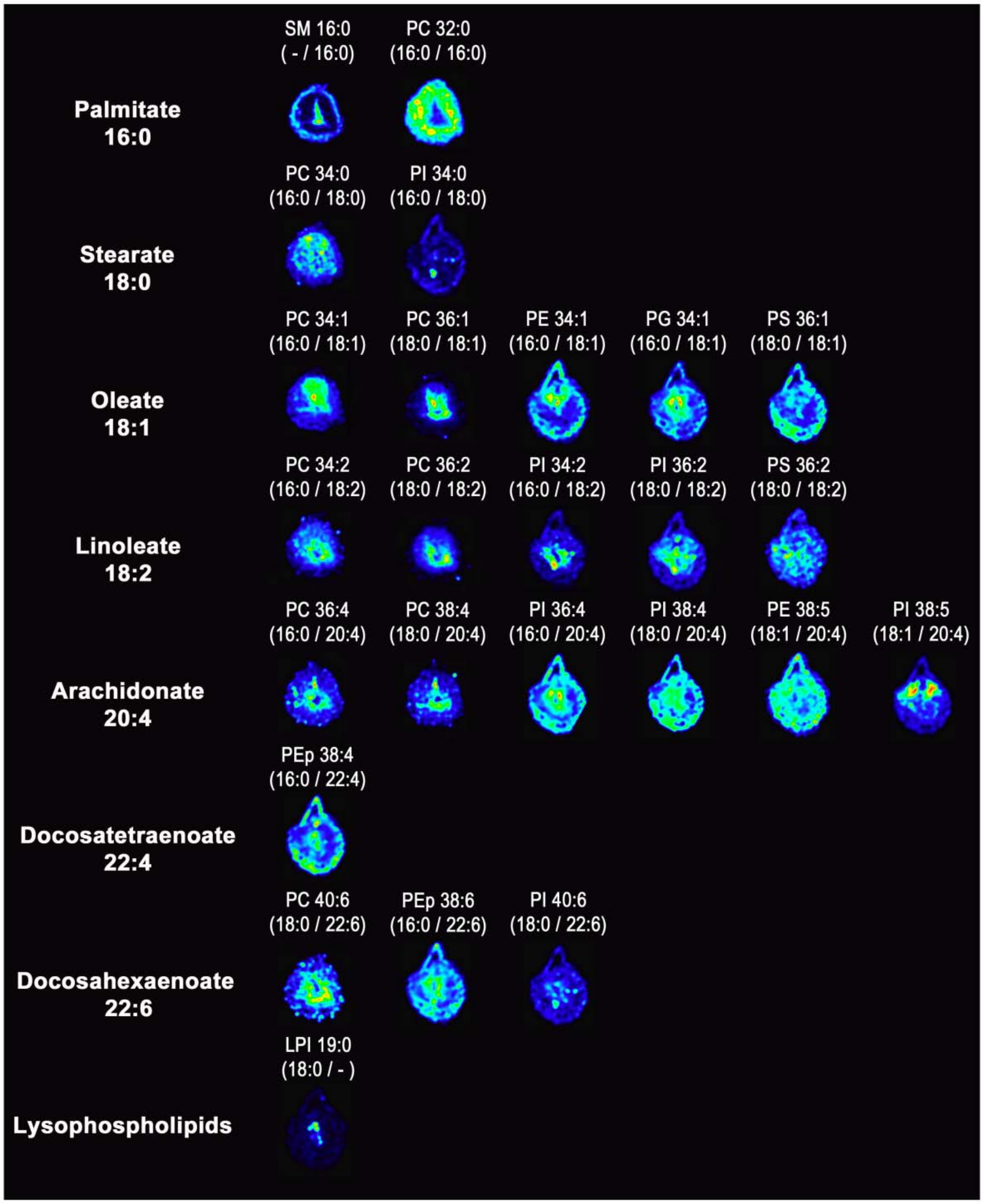

Figure 38. Phospholipid Expression on Day 6 of Pregnancy

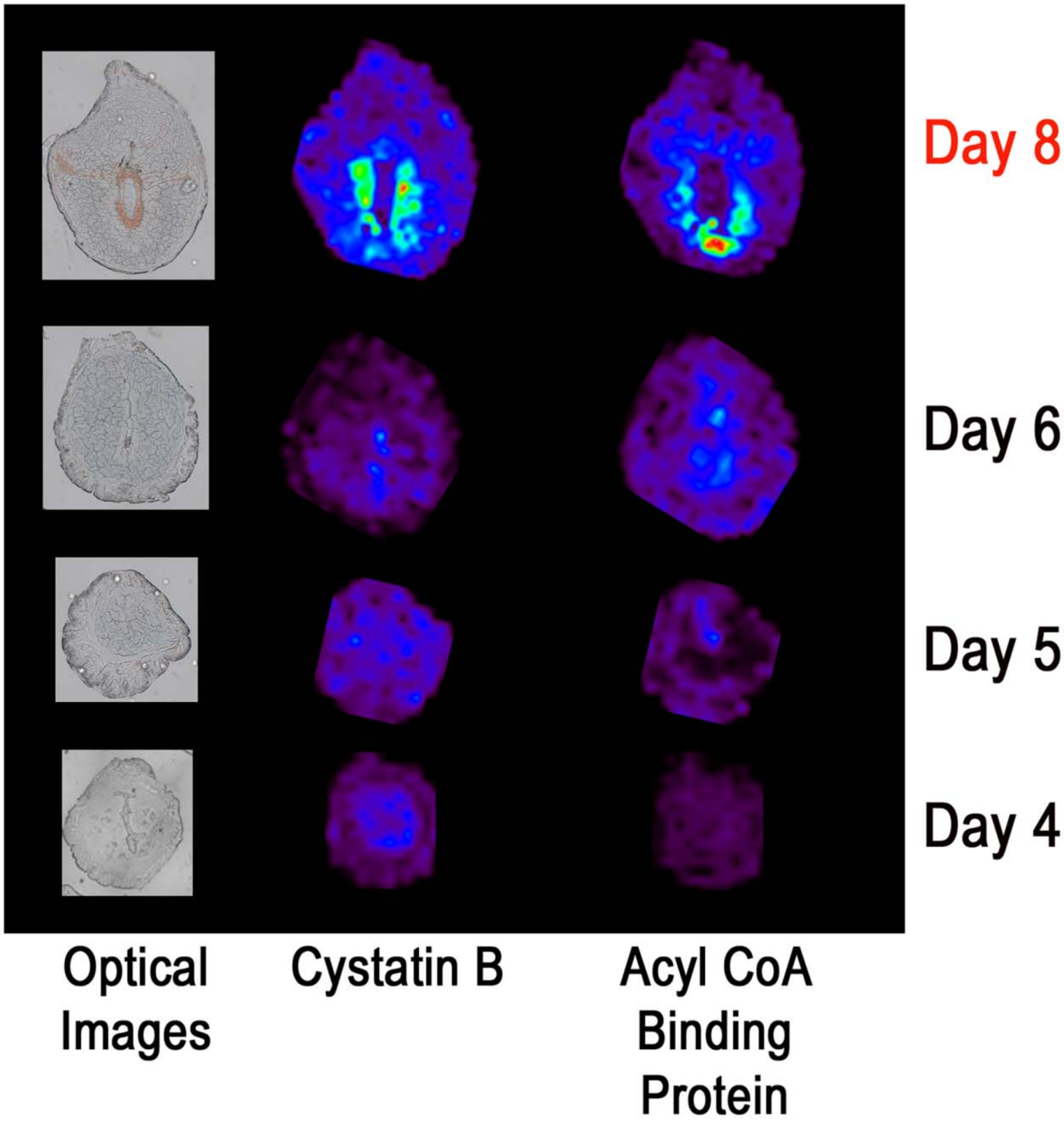

Figure 39. Proteins that show highest expression levels on Day 8 of Pregnancy

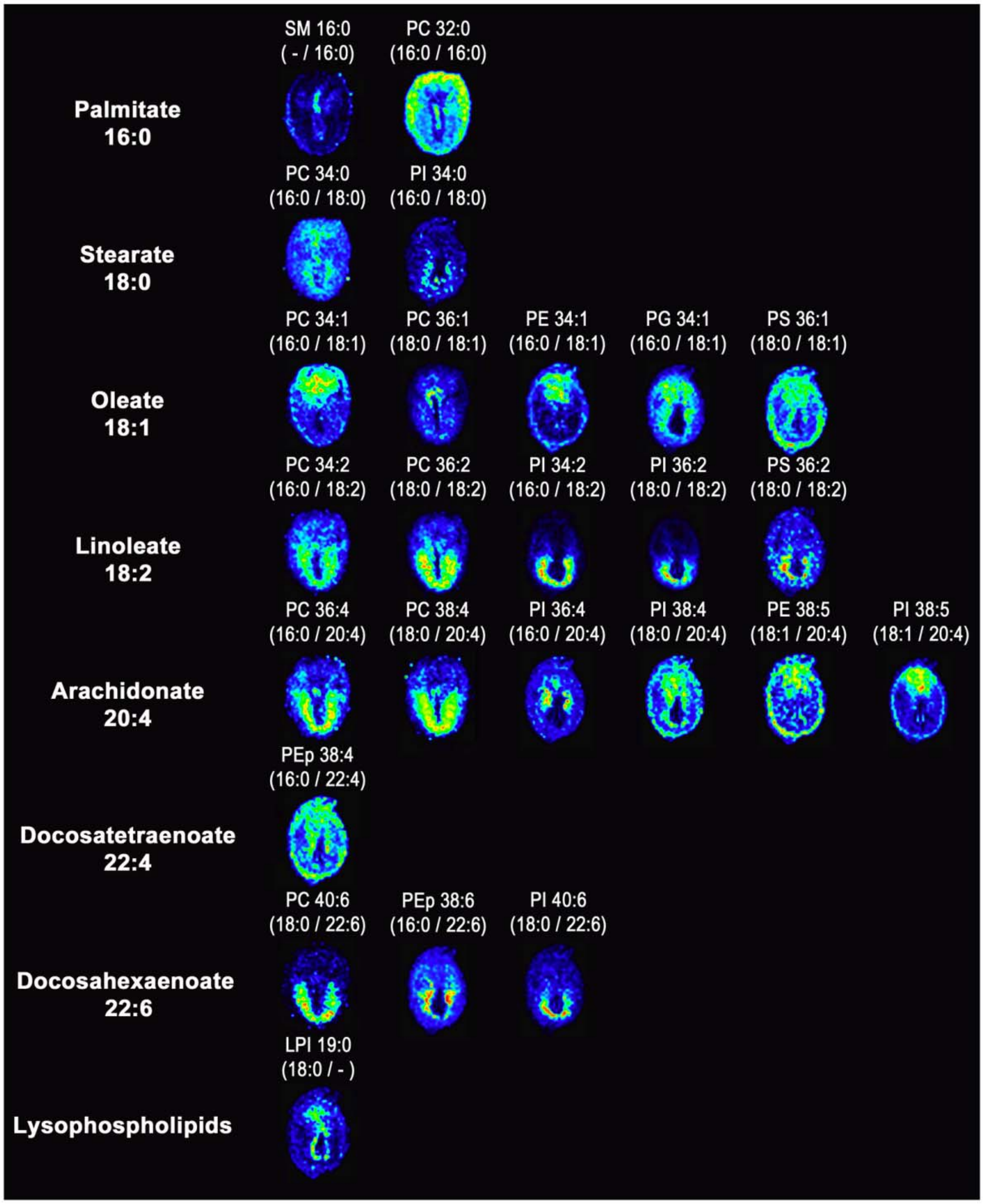

Figure 40. Phospholipid Expression on Day 8 of Pregnancy

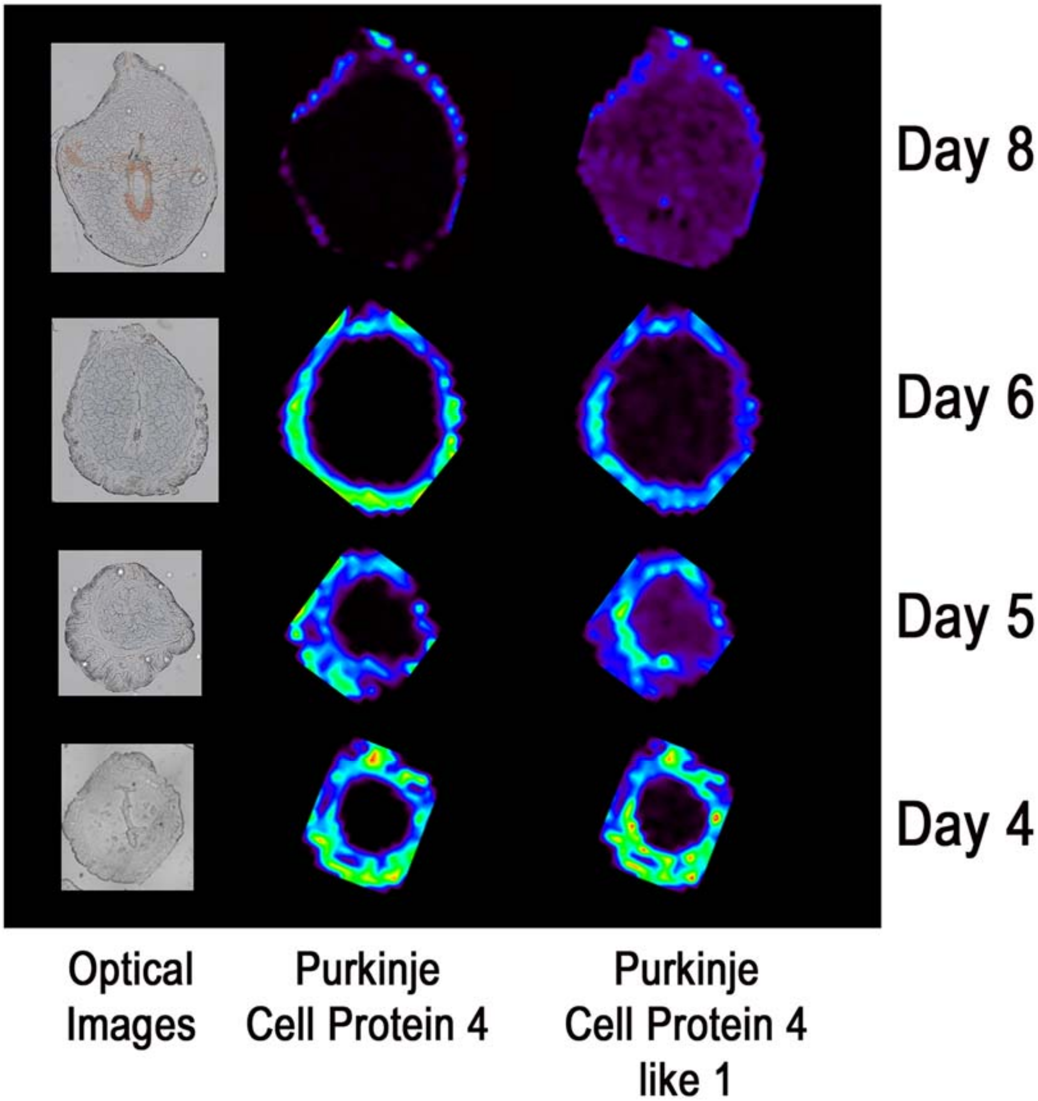

Figure 41. Proteins that show constant expression levels on Days 4-8 of Pregnancy

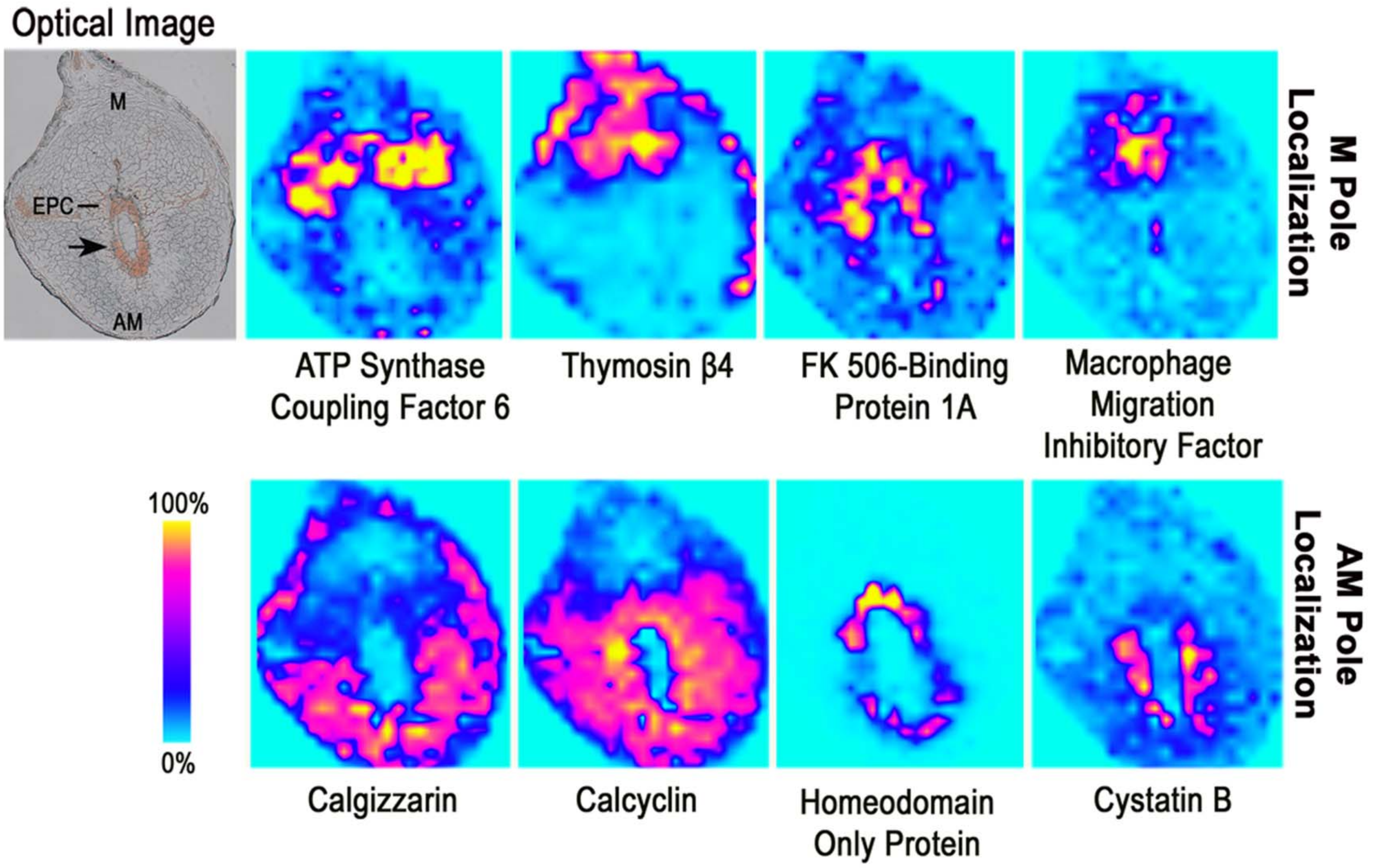

Figure 42. Protein images which show M Pole or AM Pole Expression on Day 8 of Pregnancy.

REFERENCES

1. Wang, H. & Dey, S.K. Roadmap to embryo implantation: clues from mouse models. *Nature Reviews Genetics* 7, 185-199 (2006).

2. Dey, S.K. et al. Molecular cues to implantation. *Endocrine reviews* 25, 341-373 (2004).

3. Wang, H. & Dey, S.K. Roadmap to embryo implantation: clues from mouse models. *Nat Rev Genet* 7, 185-199 (2006).

4. Anin, S., Vince, G. & Quenby, S. Trophoblast invasion. *Human Fertility* 7, 169 - 174 (2004).

5. Mincheva-Nilsson, L., Hammarstrom, S. & Hammarstrom, M.L. Human decidual leukocytes from early pregnancy contain high numbers of gamma delta+ cells and show selective down-regulation of alloreactivity. *Journal of Immunology* 149, 2203-2211 (1992).

6. Cornett, D.S., Reyzer, M.L., Chaurand, P. & Caprioli, R.M. MALDI imaging mass spectrometry: molecular snapshots of biochemical systems. *Nature Methods* 4, 828-833 (2007).

7. Puolitaival, S.M., Burnum, K.E., Cornett, D.S. & Caprioli, R.M. Solvent-Free Matrix Dry-Coating for MALDI Imaging of Phospholipids. *Journal of American Society for Mass Spectrometry* 19, 882-886 (2008).

8. Björn, J. ToF-SIMS imaging of lipids in cell membranes. *Surface and Interface Analysis* 38, 1401-1412 (2006).

9. Sinha, T.K. et al. Integrating spatially resolved three-dimensional MALDI IMS with in vivo magnetic resonance imaging. *Nature Method* 5, 57-59 (2008).

10. Khatib-Shahidi, S., Andersson, M., Herman, J.L., Gillespie, T.A. & Caprioli, R.M. Direct molecular analysis of whole-body animal tissue sections by imaging MALDI mass spectrometry. *Analytical Chemistry* 78, 6448-6456 (2006).

11. Meistermann, H. et al. Biomarker discovery by imaging mass spectrometry: Transthyretin is a biomarker for gentamicin-induced nephrotoxicity in rat. *Molecular and Cellular Proteomics* 5, 1876–1886 (2006).

12. Dass, C. Principles and Practice of Biological Mass Spectrometry. (John Wiley & Sons, New York; 2001).

13. Schwartz, S.A., Reyzer, M.L. & Caprioli, R.M. Direct tissue analysis using matrix-assisted laser desorption/ionization mass spectrometry: practical aspects of sample preparation. *Journal of Mass Spectrometry* 38, 699-708 (2003).

14. Chaurand, P., Schwartz, S.A. & Caprioli, R.M. Profiling and imaging proteins in tissue sections by MS. *Analytical Chemistry* 76, 86A-93A (2004).

15. Chaurand, P. et al. Integrating Histology and Imaging Mass Spectrometry. *Analytical Chemistry* 76, 1145-1155 (2004).

16. Chaurand, P., Sanders, M.E., Jensen, R.A. & Caprioli, R.M. Proteomics in diagnostic pathology - Profiling and imaging proteins directly in tissue sections. *American Journal of Pathology* 165, 1057-1068 (2004).

17. Woods, A.S. & Jackson, S.N. Brain tissue lipidomics: Direct probing using matrix-assisted laser desorption/ionization mass spectrometry. *The AAPS Journal* 8, E391-E395 (2006).

18. Aerni, H.R., Cornett, D.S. & Caprioli, R.M. Automated acoustic matrix deposition for MALDI sample preparation. *Analytical Chemistry* 78, 827-834 (2006).

19. Groseclose, M.R., Andersson, M., Hardesty, W.M. & Caprioli, R.M. Identification of proteins directly from tissue: in situ tryptic digestions coupled with imaging mass spectrometry. *Journal of Mass Spectrometry* 42, 254-262 (2007).

20. Baluya, D.L., Garrett, T.J. & Yost, R.A. Automated MALDI matrix deposition method with inkjet printing for imaging mass spectrometry. *Analytical Chemistry* 79, 6862-6867 (2007).

21. Guo, J. in American Society for Mass Spectrometry Conference San Antonio, TX; 2005).

22. Schuerenberg, M., Luebbert, C., Deininger, S.O., Ketterlinus, R. & Suckau, D. MALDI tissue imaging: mass spectrometric localization of biomarkers in tissue slices. *Nature Methods* 4, iii-iv (2007).

23. Nye, G.J., Norris, J.L. & Nickerson, S. in American Society for Mass Spectrometry Seattle, WA; 2006).

24. Hankina, J.A., Barkleya, R.M. & Murphy, R.C. Sublimation as a Method of Matrix Application for Mass Spectrometric Imaging. *Journal of the American Society for Mass Spectrometry* 18, 1646-1652 (2007).

25. Jurchen, J.C., Rubakhin, S.S. & Sweedler, J.V. MALDI-MS Imaging of Features Smaller than the Size of the Laser Beam. *Journal of American Society for Mass Spectrometry* 16, 1654-1659 (2005).

26. Mamyrin, B.A. Laser assisted reflectron time-of-flight mass spectrometry. *International Journal of Mass Spectrometry and Ion Processes* 131, 1-19 (1994).

27. Taban, I.M. et al. Imaging of peptides in the rat brain using MALDI-FTICR mass spectrometry. *Journal of the American Society for Mass Spectrometry* 18, 145-151 (2007).

28. Altelaar, A.F.M. et al. High-resolution MALDI imaging mass spectrometry allows localization of peptide distributions at cellular length scales in pituitary tissue sections. *International Journal of Mass Spectrometry* 260, 203-211 (2007).

29. Verhaert, P.D., Conaway, M.C.P., Pekar, T.M. & Miller, K. Neuropeptide imaging on an LTQ with vMALDI source: The complete 'all-in-one' peptidome analysis. *International Journal of Mass Spectrometry* 260, 177-184 (2007).

30. DeKeyser, S.S., Kutz-Naber, K.K., Schmidt, J.J., Barrett-Wilt, G.A. & Li, L.J. Imaging mass spectrometry of neuropeptides in decapod crustacean neuronal tissues. *Journal of Proteome Research* 6, 1782-1791 (2007).

31. Marshall, A.G. Milestones in fourier transform ion cyclotron resonance mass spectrometry technique development. *International Journal of Mass Spectrometry* 200, 331-356 (2000).

32. Khatib-Shahidi, S., Andersson, M., Herman, J.L., Gillespie, T.A. & Caprioli, R.M. Direct molecular analysis of whole-body animal tissue sections by imaging MALDI mass spectrometry. *Analytical Chemistry* 78, 6448-6456 (2006).

33. Li, Y., Shrestha, B. & Vertes, A. Atmospheric Pressure Molecular Imaging by Infrared MALDI Mass Spectrometry. *Analytical Chemistry* 79, 523-532 (2007).

34. McLean, J.A., Ridenour, W.B. & Caprioli, R.M. Profiling and imaging of tissues by imaging ion mobility-mass spectrometry. *Journal of Mass Spectrometry* 42, 1099-1105 (2007).

35. Norris, J.L. et al. Processing MALDI Mass Spectra to Improve Mass Spectral Direct Tissue Analysis. *International Journal of Mass Spectrometry* 260, 212-221 (2007).

36. Jolliffe, I.T. Principle Component Analysis, Edn. 2nd. (Springer-Verlag, New York; 2002).

37. Tusher, V.G., Tibshirani, R. & Chu, G. Significance analysis of microarrays applied to the ionizing radiation response. *Proceedings of the National Academy of Sciences* 98, 5116-5121 (2001).

38. Meunier, B. et al. Assessment of Hierarchical Clustering Methodologies for Proteomic Data Mining. *Journal of Proteome Research* 6, 358-366 (2006).

39. Marko-Varga, G. & Fehniger, T.E. Proteomics and disease - The challenges for technology and discovery. *Journal of Proteome Research* 3, 167-178 (2004).

40. Oehr, P. 'Omics'-based imaging in cancer detection and therapy. *Personalized Medicine* 3, 19-32 (2006).

41. Lescuyer, P., Hochstrasser, D. & Rabilloud, T. How Shall We Use the Proteomics Toolbox for Biomarker Discovery? *Journal of Proteome Research* 6, 3371-3376 (2007).

42. Lewin, D.A. & Weiner, M.P. Molecular biomarkers in drug development. *Drug Discovery Today* 9, 976-983 (2004).

43. Bieck, P.R. & Potter, W.Z. Biomarkers in psychotropic drug development: Integration of data across multiple domains. *Annual Review of Pharmacology and Toxicology* 45, 227-246 (2005).

44. Strand, K.J., Khalak, H., Strovel, J.W., Ebner, R. & Augustus, M. Expression biomarkers for clinical efficacy and outcome prediction in cancer. *Pharmacogenomics* 7, 105-115 (2006).

45. Pusch, W., Flocco, M.T., Leung, S.M., Thiele, H. & Kostrzewa, M. Mass spectrometry-based clinical proteomics. *Pharmacogenomics* 4, 463-476 (2003).

46. Scaros, O. & Fisler, R. Biomarker technology roundup: from discovery to clinical applications, a broad set of tools is required to translate from the lab to the clinic. *Biotechniques* 38, S30-S-32 (2005).

47. Kamb, A., Wee, S. & Lengauer, C. Opinion - Why is cancer drug discovery so difficult? *Nature Reviews Drug Discovery* 6, 115-120 (2007).

48. Hanahan, D. & Weinberg, R.A. The hallmarks of cancer. *Cell* 100, 57-70 (2000).

49. Stoeckli, M., Chaurand, P., Hallahan, D.E. & Caprioli, R.M. Imaging mass spectrometry: a new technology for the analysis of protein expression in mammalian tissues. *Nature medicine* 7, 493-496 (2001).

50. Reyzer, M.L. et al. Early changes in protein expression detected by mass spectrometry predict tumor response to molecular therapeutics. *Cancer Research* 64, 9093-9100 (2004).

51. Johnson, M.D., Floyd, J.L. & Caprioli, R.M. Proteomics in Diagnostic Neuropathology. *Journal of Neuropathology and Experimental Neurology* 65, 837-845 (2006).

52. Schwamborn, K. et al. Identifying prostate carcinoma by MALDI-Imaging. *International Journal of Molecular Medicine* 20, 155-159 (2007).

53. Chaurand, P. et al. Monitoring Mouse Prostate Development by Profiling and Imaging Mass Spectrometry. *Molecular & Cellular Proteomics* 7, 411-423 (2008).

54. Crecelius, A.C. et al. Three-dimensional visualization of protein expression in mouse brain structures using imaging mass spectrometry. *Journal of the American Society for Mass Spectrometry* 16, 1093-1099 (2005).

55. Andersson, M., Groseclose, M.R., Deutch, A.Y. & Caprioli, R.M. Imaging mass spectrometry of proteins and peptides: 3D volume reconstruction. *Nature Method* 5, 101-108 (2008).

56. Haacke, E.M., Brown, R.W., Thompson, M.L. & Venkatesan, R. Magnetic Resonance Imaging: Physical Principles and Sequence Design. (John Wiley, 1999).

57. Ingelsson, M. et al. Early A beta accumulation and progressive synaptic loss, gliosis, and tangle formation in AD brain. *Neurology* 62, 925-931 (2004).

58. Schonheit, B., Zarski, R. & Ohm, T.G. Spatial and temporal relationships between plaques and tangles in Alzheimer-pathology. *Neurobiology of Aging* 25, 697-711 (2004).

59. Rohner, T.C., Staab, D. & Stoeckli, M. MALDI mass spectrometric imaging of biological tissue sections. *Mechanisms of Ageing and Development* 126, 177-185 (2005).

60. Skold, K. et al. Decreased striatal levels of PEP-19 following MPTP lesion in the mouse. *Journal of Proteome Research* 5, 262-269 (2006).

61. Walgren, J.L. & Thompson, D.C. Application of proteomic technologies in the drug development process. *Toxicology Letters* 149, 377-385 (2004).

62. Rudin, M., Rausch, M. & Stoeckli, M. Molecular imaging in drug discovery and development: Potential and limitations of nonnuclear methods. *Molecular Imaging and Biology* 7, 5-13 (2005).

63. Hsieh, Y., Chen, J. & Korfmacher, W.A. Mapping pharmaceuticals in tissues using MALDI imaging mass spectrometry. *Journal of Pharmacological and Toxicological Methods* 55, 193-200 (2007).

64. Lemaire, R. et al. Direct analysis and MALDI imaging of formalin-fixed, paraffin-embedded tissue sections. *Journal of Proteome Research* 6, 1295-1305 (2007).

65. Groseclose, M.R., Massion, P.P., Chaurand, P. & Caprioli, R.M. High-throughput proteomic analysis of formalin-fixed paraffin-embedded tissue microarrays using MALDI imaging mass spectrometry. *Proteomics* 8, 3715-3724 (2008).

66. Garrett, T.J. et al. Imaging of small molecules in tissue sections with a new intermediate-pressure MALDI linear ion trap mass spectrometer. *International Journal of Mass Spectrometry* 260, 166-176 (2007).

67. Jackson, S.N., Wang, H.-Y.J. & Woods, A.S. In Situ Structural Characterization of Phosphatidylcholines in Brain Tissue Using MALDI-MS/MS. *Journal of the American Society for Mass Spectrometry* 16, 2052-2056 (2005).

68. Jackson, S.N., Wang, H.-Y.J. & Woods, A.S. Direct tissue analysis of phospholipids in rat brain using MALDI-TOFMS and MALDI-ion mobility-TOFMS *Journal of the American Society for Mass Spectrometry* 16, 133-138 (2005).

69. Jackson, S.N., Wang, H.Y.J. & Woods, A.S. Direct Profiling of Lipid Distribution in Brain Tissue Using MALDI-TOFMS. *Analytical Chemistry* 77, 4523-4527 (2005).

70. Fujiwaki, T., Yamaguchi, S., Sukegawa, K. & Taketomi, T. Application of delayed extraction matrix-assisted laser desorption ionization time-of-flight mass spectrometry for analysis of sphingolipids in cultured skin fibroblasts from sphingolipidosis patients. *Brain & development* 24, 170-173 (2002).

71. He, X., Chen, F., Dagan, A., Gatt, S. & Schuchman, E.H. A fluorescence-based, high-performance liquid chromatographic assay to determine acid sphingomyelinase activity and diagnose types A and B Niemann–Pick disease. *Analytical Biochemistry* 314, 116-120 (2003).

72. Han, X., Holtzman, D.M., McKeel, D.W., Kelley, J. & Morris, J.C. Substantial sulfatide deficiency and ceramide elevation in very early Alzheimer's disease: potential role in disease pathogenesis. *Journal of Neurochemistry* 82, 809-818 (2002).

73. Murphy, E.J., Schapiro, M.B., Rapoport, S.I. & Shetty, H.U. Phospholipid composition and levels are altered in down syndrome brain. *Brain Research* 867 9-18 (2000).

74. Wang, H.-Y.J., Jackson, J.N., Post, J. & Woods, A.S. A minimalist approach to MALDI imaging of glycerophospholipids and sphingolipids in rat brain sections. *International Journal of Mass Spectrometry* doi:10.1016/j.ijms.2008.04.005 (2008).

75. Svennerholm, L. Distribution and fatty acid composition of phosphoglycerides in normal human brain. *Journal of Lipid Research* 9, 570-579 (1968).

76. Ivanova, P.T. et al. Glycerophospholipid Identification and Quantitation by Electrospray Ionization Mass Spectrometry. *Methods in Enzymology* 432, 21-57 (2007).

77. Touchstone, J.C. Thin-layer chromatographic procedures for lipid separation. *Journal of Chromatography. B, Biomedical applications* 671, 169-195 (1995).

78. Harris, E., Gharavi, A. & Hughes, G. Anti-phospholipid antibodies. *Clinics in Rheumatic Diseases* 11, 591-609 (1985).

79. Wiseman, J.M., Ifa, R.D., Song, Q. & Cooks, R.G. Tissue Imaging at Atmospheric Pressure Using Desorption Electrospray Ionization (DESI) Mass Spectrometry. *Angewandte Chemie (International ed. in English)* 45, 7188-7192 (2006).

80. Sjövall, P., Johansson, B. & Lausmaa, J. Localization of lipids in freeze-dried mouse brain sections by imaging TOF-SIMS *Applied Surface Science* 252, 6966-6974 (2006).

81. Börner, K., Malmberg, P., Månsson, J.-E. & Nygren, H. Molecular imaging of lipids in cells and tissues. *International Journal of Mass Spectrometry* 260, 128-136 (2007).

82. Jackson, S.N. et al. MALDI-ion mobility-TOFMS imaging of lipids in rat brain tissue. *Journal of Mass Spectrometry* 42, 1093-1098 (2007).

83. Hanahan, D.J. A Guide to Phospholipid Chemistry. (Oxford University Press, New York; 1997; pp 65-74).

84. Wright, M.M., Howe, A.G. & Zaremberg, V. Cell membranes and apoptosis: role of cardiolipin, phosphatidylcholine, and anticancer lipid analogues. *Biochemistry and Cell Biology* 82, 18-26 (2004).

85. Wenk, M.R. Lipidomics in drug and biomarker development. *Expert Opinion on Drug Discovery* 1, 723-736 (2006).

86. Chaurand, P. et al. Profiling and imaging proteins in the mouse epididymis by imaging mass spectrometry. *Proteomics* 3, 2221-2239 (2003).

87. Paria, B.C., Huet-Hudson, Y.M. & Dey, S.K. Blastocyst's state of activity determines the "window" of implantation in the receptive mouse uterus. *Proceedings of the National Academy of Sciences of the United States of America* 90, 10159-10162 (1993).

88. Das, S.K. et al. Heparin-binding EGF-like growth factor gene is induced in the mouse uterus temporally by the blastocyst solely at the site of its apposition: a possible ligand for interaction with blastocyst EGF-receptor in implantation. *Development (Cambridge, England)* 120, 1071-1083 (1994).

89. Enders, A.C. Anatomical aspects of implantation. *Journal of reproduction and fertility* 25, 1-15 (1976).

90. Schlafke, S. & Enders, A.C. Cellular basis of interaction between trophoblast and uterus at implantation. *Biology of reproduction* 12, 41-65 (1975).

91. Shah, B.H. & Catt, K.J. Roles of LPA3 and COX-2 in implantation. *Trends in Endocrinology and Metabolism* 16, 397-399 (2005).

92. Mills, G.B. & Moolenaar, W.H. The emerging role of lysophosphatidic acid in cancer. *Nat Rev Cancer* 3, 582-591 (2003).

93. Khan, W.A., Blobe, G.C. & Hannun, Y.A. Arachidonic acid and free fatty acids as second messengers and the role of protein kinase C. *Cellular Signalling* 7, 171-184 (1995).

94. Smith, W.L., DeWitt, D.L. & Garavito, R.M. Cyclooxygenases: structural, cellular, and molecular biology. *Annu Rev Biochem* 69, 145-182 (2000).

95. Song, H. et al. Cytosolic phospholipase A2alpha is crucial [correction of A2alpha deficiency is crucial] for 'on-time' embryo implantation that directs subsequent development. *Development* 129, 2879-2889 (2002).

96. Lim, H. et al. Multiple female reproductive failures in cyclooxygenase 2-deficient mice. *Cell* 91, 197-208 (1997).

97. Wang, H. et al. Rescue of Female Infertility from the Loss of Cyclooxygenase-2 by Compensatory Up-regulation of Cyclooxygenase-1 Is a Function of Genetic Makeup. *The Journal of Biological Chemistry* 279, 10649-10658 (2004).

98. Chakraborty, I., Das, S.K., Wang, J. & Dey, S.K. Developmental expression of the cyclo-oxygenase-1 and cyclo-oxygenase-2 genes in the peri-implantation mouse uterus and their differential regulation by the blastocyst and ovarian steroids. *Journal of Molecular Endocrinology* 16, 107-122 (1996).

99. Matsumoto, H. et al. Diversification of cyclooxygenase-2-derived prostaglandins in ovulation and implantation. *Biol Reprod* 64, 1557-1565 (2001).

100. Lim, H. et al. Cyclo-oxygenase-2-derived prostacyclin mediates embryo implantation in the mouse via PPARdelta. *Genes Dev* 13, 1561-1574 (1999).

101. Davis, B.J. et al. Anovulation in cyclooxygenase-2-deficient mice is restored by prostaglandin E2 and interleukin-1beta. *Endocrinology* 140, 2685-2695 (1999).

102. Segi, E. et al. Expression of messenger RNA for prostaglandin E receptor subtypes EP4/EP2 and cyclooxygenase isozymes in mouse periovulatory follicles and oviducts during superovulation. *Biol Reprod* 68, 804-811 (2003).

103. Ishii, I., Fukushima, N., Ye, X. & Chun, J. Lysophospholipid receptors: signaling and biology. *Annu Rev Biochem* 73, 321-354 (2004).

104. Ye, X. et al. LPA3-mediated lysophosphatidic acid signalling in embryo implantation and spacing. *Nature* 435, 104-108 (2005).

105. Dey, S.K. Reproductive biology: fatty link to fertility. *Nature* 435, 34-35 (2005).

106. Wilcox, A.J., Baird, D.D. & Weinberg, C.R. Time of implantation of the conceptus and loss of pregnancy. *N Engl J Med* 340, 1796-1799 (1999).

107. Mizugishi, K. et al. Maternal disturbance in activated sphingolipid metabolism causes pregnancy loss in mice. *J Clin Invest* 117, 2993-3006 (2007).

108. Sjovall, P., Lausmaa, J. & Johansson, B. Mass Spectrometric Imaging of Lipids in Brain Tissue. *Analytical Chemistry* 76, 4271-4278 (2004).

109. Touboul, D. et al. MALDI-TOF and cluster-TOF-SIMS imaging of Fabry disease biomarkers. *International Journal of Mass Spectrometry* 260, 158-165 (2007).

110. Rujoi, M., Estrada, R. & Yappert, M.C. In Situ MALDI-TOF MS Regional Analysis of Neutral Phospholipids in Lens Tissue. *Analytical Chemistry* 76, 1657-1663 (2004).

111. Caprioli, R.M., Farmer, T.B. & Gile, J. Molecular imaging of biological samples: localization of peptides and proteins using MALDI-TOF MS. *Analytical Chemistry* 69, 4751-4760 (1997).

112. Cornett, D.S., Reyzer, M.L., Chaurand, P. & Caprioli, R.M. MALDI imaging mass spectrometry: molecular snapshots of biochemical systems. *Nat Meth* 4, 828-833 (2007).

113. Burnum, K.E. et al. Imaging Mass Spectrometry Reveals Unique Protein Profiles during Embryo Implantation. *Endocrinology* 149, 3274-3278 (2008).

114. Voet, D. & Voet, J.G. Biochemistry, Edn. 3. (John Wiley & Sons, Inc, New Jersey; 2004).

115. Murphy, R.C. & Harrison, K.A. Fast atom bombardment mass spectrometry of phospholipids. *Mass Spectrometry Reviews* 13, 57-75 (1994).

116. Akcali, K.C., Khan, S.A. & Moulton, B.C. Effect of decidualization on the expression of bax and bcl-2 in the rat uterine endometrium. **137**, 3123-3131 (1996).

117. Rouzer, C.A. et al. Lipid Profiling Reveals Arachidonate Deficiency in RAW264.7 Cells: Structural and Functional Implications. *Biochemistry* **45**, 14795-14808 (2006).

118. Rouzer, C.A., Ivanova, P.T., Byrne, M.O., Brown, H.A. & Marnett, L.J. Lipid Profiling Reveals Glycerophospholipid Remodeling in Zymosan-Stimulated Macrophages. *Biochemistry* **46**, 6026-6042 (2007).

119. Hsu, F.F., Bohrer, A. & Turk, J. Formation of Lithiated Adducts of Glycerophosphocholine Lipids Facilitates their Identification by Electrospray Ionization Tandem Mass Spectrometry. *Journal of the American Society for Mass Spectrometry* **9**, 516-526 (1998).

120. Tan, J., Paria, B.C., Dey, S.K. & Das, S.K. Differential uterine expression of estrogen and progesterone receptors correlates with uterine preparation for implantation and decidualization in the mouse. *Endocrinology* **140**, 5310-5321 (1999).

121. Karas, M., Bachmann, D., Bahr, U. & Hillenkamp, F. Matrix-Assisted Ultraviolet Laser Desorption of Non-Volatile Compounds. *International Journal of Mass Spectrometry and Ion Processes* **78**, 53-68 (1987).

122. Farnsworth, R.L. & Talamantes, F. Calcyclin in the mouse decidua: expression and effects on placental lactogen secretion. *Biology of reproduction* **59**, 546-552 (1998).

123. McKinnon, B., Li, H., Richard, K. & Mortimer, R. Synthesis of thyroid hormone binding proteins transthyretin and albumin by human trophoblast. *The Journal of clinical endocrinology and metabolism* **90**, 6714-6720 (2005).

124. Waterhouse, P., Parhar, R.S., Guo, X., Lala, P.K. & Denhardt, D.T. Regulated temporal and spatial expression of the calcium-binding proteins calcyclin and OPN (osteopontin) in mouse tissues during pregnancy. *Molecular reproduction and development* **32**, 315-323 (1992).

125. Bonventre, J.V. et al. Reduced fertility and postischaemic brain injury in mice deficient in cytosolic phospholipase A2. *Nature* **390**, 622-625 (1997).

126. Clark, K.L. & Pierre, L. Characterization of endothelin receptors in rat renal artery in vitro. *British journal of pharmacology* **114**, 785-790 (1995).

127. Uozumi, N. et al. Role of cytosolic phospholipase A2 in allergic response and parturition. *Nature* 390, 618-622 (1997).

128. Sawicki, G., Dakour, J. & Morrish, D.W. Functional proteomics of neurokinin B in the placenta indicates a novel role in regulating cytotrophoblast antioxidant defences. *Proteomics* 3, 2044-2051 (2003).

129. Liu, A.X. et al. Proteomic analysis on the alteration of protein expression in the placental villous tissue of early pregnancy loss. *Biology of reproduction* 75, 414-420 (2006).

130. Vascotto, C. et al. Oxidized transthyretin in amniotic fluid as an early marker of preeclampsia. *Journal of Proteome Research* 6, 160-170 (2007).

131. Aerni, H.R., Cornett, D.S. & Caprioli, R.M. Automated acoustic matrix deposition for MALDI sample preparation. *Analytical Chemistry* 78, 827-834 (2006).

132. Seeley, E.H., Oppenheimer, S.R., Mi, D., Chaurand, P. & Caprioli, R.M. Enhancement of Protein Sensitivity for MALDI Imaging Mass Spectrometry After Chemical Treatment of Tissue Sections. *Journal of the American Society for Mass Spectrometry* 19, 1069-1077 (2008).

133. Tusher, V.G., Tibshirani, R. & Chu, G. Significance analysis of microarrays applied to the ionizing radiation response. *Proceedings of the National Academy of Sciences of the United States of America* 98, 5116-5121 (2001).

134. Eng, J.K., McCormack, A.L. & Yates, J.R. An approach to correlate tandem mass spectral data of peptides with amino acid sequences in a protein database. *Journal of American Society for Mass Spectrometry* 5, 976-989 (1994).

135. Keller, A. et al. Experimental protein mixture for validating tandem mass spectral analysis. *Omics* 6, 207-212 (2002).

136. Nesvizhskii, A.I., Keller, A., Kolker, E. & Aebersold, R. A statistical model for identifying proteins by tandem mass spectrometry. *Analytical Chemistry* 75, 4646-4658 (2003).

137. Wong-Riley, M. Changes in the visual system of monocularly sutured or enucleated cats demonstrable with cytochrome oxidase histochemistry. *Brain Research* 171, 11-28 (1979).

138. Spahr, C.S. et al. Towards defining the urinary proteome using liquid chromatography-tandem mass spectrometry I.Profiling an unfractionated tryptic digest. *Proteomics* 1, 93-107 (2001).

139. Herring, K.D. C-Terminal Cleavage of Ubiquitin: From Experimental Artifact to Biological Relevance. *Vanderbilt University Biochemistry Thesis* (December 2008).

140. Le Page, C. et al. Gene expression profiling of primary cultures of ovarian epithelial cells identifies novel molecular classifiers of ovarian cancer. *British Journal of Cancer* 94, 436-445 (2006).

141. Campostrini, N. et al. Proteomic analysis of anti-angiogenic effects by a combined treatment with vinblastine and rapamycin in an endothelial cell line. *Proteomics* 6, 4420-4431 (2006).

142. Philp, D., Huff, T., Gho, Y.S., Hannappel, E. & Kleinman, H.K. The actin binding site on thymosin {beta}4 promotes angiogenesis. *FASEB Journal* 17, 2103-2105 (2003).

143. van Beijnum, J.R. et al. Gene expression of tumor angiogenesis dissected: specific targeting of colon cancer angiogenic vasculature. *Blood* 108, 2339-2348 (2006).

144. Xu, X.D. et al. Overexpression of macrophage migration inhibitory factor induces angiogenesis in human breast cancer. *Cancer Letters* 261, 147-157 (2008).

145. Asanoma, K. et al. HOP/NECC1, A Novel Regulator of Mouse Trophoblast Differentiation. *Journal of Biological Chemistry* 282, 24065-24074 (2007).

146. Joo, J.H. et al. S100A6 (Calcyclin) enhances the sensitivity to apoptosis via the upregulation of caspase-3 activity in Hep3B cells. *Journal of Cellular Biochemistry* 103, 1183-1197 (2008).

147. Na, L. et al. A proteomic investigation into a human gastric cancer cell line BGC823 treated with diallyl trisulfide. *Carcinogenesis* 27, 1222-1231 (2006).

148. Soundararajan, R. & Rao, A.J. Trophoblast 'pseudeo-tumorigenesis': Significance and contributory factors. *Reproductive Biology and Endocrinology* 2, 15 (2004).

149. Reyes, N., Reyes, I., Tiwari, R. & Geliebter, J. Effect of linoleic acid on proliferation and gene expression in the breast cancer cell line T47D. *Cancer Letters* 209, 25-35 (2004).

150. Abeywardena, M.Y. & Head, R.J. Longchain n-3 polyunsaturated fatty acids and blood vessel function. *Cardiovascular Research* 52, 361-371 (2001).